

PHASE STABILITY IN TI/BCC MULTILAYERED THIN FILMS

by

LI WAN

GREGORY B. THOMPSON, COMMITTEE CHAIR
ROBIN D. FOLEY
SUSHMA KOTRU
LIN LI
GARY J. MANKEY

A DISSERTATION

Submitted in partial fulfillment of the requirements
for the degree of Doctor of Philosophy in the
Department of Metallurgical and Materials Engineering
in the Graduate School of
The University of Alabama

TUSCALOOSA, ALABAMA

2016

ABSTRACT

Materials structures with large surface area-to-volume ratios can exhibit size dependent physical and chemical properties that are different than their bulk form. These changes are often related to the material adopting a different crystallographic phase. Often these phase transformations are serendipitously observed with the criteria for their stability difficult to ascertain. This work elucidates the underpinnings of phase stability behavior in the nanoscale regime by providing a systematic study using Ti/bcc multilayered thin film architectures. The influences of lattice misfit, layer thickness, composition and chemical intermixing on the phase stability are determined. *In situ* thin film growth stresses of these materials are measured and correlated to the interfacial stress evolution to help rationalize the stability behavior. X-ray and electron diffraction have been employed to determine the phase with atom probe tomography used to characterize the chemical compositions within the materials and across the interfaces. This work will delineate how intrinsic film stress drives compositional intermixing across such interfaces which can thermodynamically promote phase transformations.

DEDICATION

Dedicated to my parents, the reason of what I become today.

LIST OF ABBREVIATIONS AND SYMBOLS

$1/R$	Curvature of the film during/after deposition
$1/R0$	Curvature of the film before deposition
a_{bcc}	Lattice constant of the bcc metals
APT	Atom probe tomography
Ar	Argon
a_{Ti}	Lattice constant of bcc Ti
bcc	Body centered cubic
BF	Bright field
CNA	Common neighbor analysis
ε	Strain
EAM	Embedded atom model
E_k	Kinetic energy of the atom
E_s	Young's modulus of the substrate
fcc	Face centered cubic
Fe	Iron
f_i	Volume fraction

<i>FIB</i>	Focused ion beam
<i>Ga</i>	Gallium
<i>HAADF</i>	High angle annular dark field
<i>hcp</i>	Hexagonal closed packed
<i>HRTEM</i>	High resolution transmission electron microscope
<i>m₀</i>	Lattice misfit
<i>MD</i>	Molecular dynamic
<i>MOS</i>	Multi-beam Optic Sensor
<i>Nb</i>	Niobium
<i>NVE</i>	Number, volume, energy
<i>NVT</i>	Number, volume, temperature
<i>PIPS</i>	Precision ion polishing system
<i>ROI</i>	Region of interest
<i>SAD</i>	Selected area diffraction
<i>STEM</i>	Scanning transmission electron microscope
<i>TEM</i>	Transmission electron microscope
<i>t_f</i>	Thickness of the film
<i>Ti</i>	Titanium
<i>t_s</i>	Thickness of the substrate
<i>V</i>	Vanadium

W	Tungsten
XRD	X-ray diffraction
XRR	X-ray reflectivity
Z	Atomic number
γ	Surface energy
ΔG_v	Volumetric energy change
$\Delta\gamma$	Interfacial energy change
ν_s	Poisson ratio of substrate
σ_f	Film stress
λ	Bilayer thickness

ACKNOWLEDGEMENTS

I would like to give my sincerest thanks to my family, friends, and colleagues for their support in this research project. A special mention must go to my research advisor, Dr. Georgy Thompson, for his technical guidance, support, sharing his research expertise and wisdom in conducting this research. His mentorship has allowed me to accomplish many professional and personal goals in my graduate school career for which I am truly grateful. I would also like to thank all my committee members, Drs. Robin Foley, Sushma Kotru, Lin Li, and Gary Mankey for their invaluable input, inspiring questions, and support to the research.

I would like to recognize the National Science Foundation for their financial support for this research through grant DMR 1207220. I also appreciate the use of facilities in the Central Analytical Facility (CAF).

I would also like to acknowledge my fellow colleagues: Dr. Justin Brons, Dr. Chad Hornbuckle, Dr. Xiao-xiang Yu, Dr. Monica Kapoor, Dr. Anne Copper, Dr. Florian Vogel, Nicholas De Leon, Thomas Burton, Suzanne Kornegay, Jelani Hardwick, Katherine Vinson, Tyler Kaub, Chase Smith, Xuyang Zhou, Qianying Guo, Miki Ngai, Dallin Barton, for their support, help, and most importantly friendship during the progress of this research. My thanks also go to Mr. Rich Martens, Johnny Goodwin, and Rob Holler in Central Analytical Facility for their assistance in materials characterization.

Finally, thanks to my fiancée Jingfu Liu, for his unconditional love and support as I worked through the graduate school.

CONTENTS

ABSTRACT	ii
DEDICATION	iii
LIST OF ABBREVIATIONS AND SYMBOLS.....	iv
ACKNOWLEDGEMENTS	vii
LIST OF TABLES	xiii
LIST OF FIGURES.....	xiv
1. INTRODUCTION.....	1
1.1 Motivation	1
1.2 Prediction of Phase Stability in Multilayered Thin Films	6
1.3 Stress Evolution in Multilayered Thin Films	9
1.4 Materials Selection for BCC Template	12
1.5 Thin Film Deposition and Structural Characterization	14
1.6 Dissertation Layout	16
1.7 References	19
2. PHASE STABILITY AND IN SITU GROWTH STRESSES IN TI/NB THIN FILMS.....	22

2.1 Abstract.....	22
2.2 Introduction.....	23
2.3 Experimental and Computational Details	25
2.4 Experimental Results	27
2.5 Discussions	36
2.6 Summary	42
2.7 Acknowledgements.....	43
2.8 References	43
3. ELUCIDATING TI'S SUB-GROWTH SURFACE PHASE TRANSFORMATION IN NB/TI/NB NANOLAMINATES	47
3.1 Abstract.....	47
3.2 Introduction	48
3.3 MD Simulations of 2 nm Ti/2 nm Nb Multilayer.....	50
3.4 MD Simulation of 3 nm Ti/3 nm Nb Multilayer	53
3.5 Experimental Confirmation of BCC Ti	56
3.6 Summary.....	58
3.7 Acknowledgements	59
3.8 References	60
4. INTERRELATIONSHIP OF IN SITU GROWTH STRESS EVOLUTION AND PHASE TRANSFORMATIONS IN TI/W MULTILAYERED THIN FILMS	62

4.1 Abstract.....	62
4.2 Introduction	63
4.3 Experimental and Computational Details	66
4.4 Results and Discussions	68
4.5 Conclusions	82
4.6 Acknowledgements	83
4.7 References	83
5. BCC STABILIZATION AND GROWTH STRESSES BEHAVIOR IN TI/V MULTILAYERS	87
5.1 Abstract.....	87
5.2 Introduction	88
5.3 Experimental Details	91
5.4 Experimental Results	93
5.5 Discussions	105
5.6 Conclusions	110
5.7 Acknowledgements	111
5.8 References	111
6. INFLUENCE OF FE UNDERLAYERS ON STRESS EVOLUTION OF TI IN TI/FE MULTILAYERS	114
6.1 Abstract.....	114

6.2 Introduction	115
6.3 Experimental Details	118
6.4 Results and Discussions	120
6.5 Summary.....	134
6.6 Acknowledgements	134
6.7 References	134
7. CONCLUSIONS AND FUTURE WORK.....	138
APPENDICES	144

LIST OF TABLES

1.1 Lattice Misfit and Surface Energies of Ti and BCC Metals.....	13
2.1 Interfacial Stress for Ti/Nb Multilayers	33
4.1 Interfacial Stress for Ti/W Multilayers	75
5.1 Intermixing Width in Ti/V Multilayers	103
5.2 Lattice Strain Calculated from XRD for Ti/V Multilayers	107
6.1 Lattice Strain Calculated from XRD for Ti/Fe Multilayers	123

LIST OF FIGURES

1.1 Strain Contribution to the Phase Stability	3
1.2 Schematic of Bain Strain in fcc Cu	4
1.3 A/B Multilayered Thin Film Stack	7
1.4 Zr/Nb Multilayers Biphase Diagram	8
1.5 Schematic Cartoon of Generic Stress Evolution	10
1.6 Growth Stresses in Ag/Cu Multilayers	11
2.1 TEM BF Images and Diffraction Patterns of Ti/Nb Multilayers	29
2.2 Stress Evolution in Ti/Nb Multilayers	31
2.3 Atom Probe Compositional Profile of Ti/Nb Multilayers	35
2.4 MD Simulations for Ti/Nb Multilayers	37
3.1 MD Simulations of 2 nmTi/2 nm Nb on Nb Substrate	52
3.2 MD Simulations of 3 nmTi/3 nm Nb Multilayers	54
3.3 HCP and BCC Coordination in Ti and Nb Cap layers	55
3.4 TEM Images of 3 nm/3 nm and 2 nm/2 nm Ti/Nb Multilayers	57
4.1 XRD Scans of Ti/W Multilayers	70
4.2 TEM Images and Diffraction Patterns of Ti/W Multilayers	71

4.3 Stress Evolution in Ti/W Multilayers	74
4.4 MD Simulations of Phase Stability in Ti/W Multilayers	80
5.1 XRD Scans of Ti/W Multilayers	94
5.2 TEM Images and Diffraction Patterns of Ti/V Multilayers	96
5.3 TEM Images and Orientation Relationship in Ti/V	98
5.4 Stress Evolution in Ti/V Multilayers.....	100
5.5 Atom Probe Compositional Profile of Ti/V Multilayers.....	104
6.1 XRD Scans of Ti/Fe Multilayers	121
6.2 Diffraction Patterns of Ti/Fe Multilayers	125
6.3 TEM Images and Atom Probe 1D Profiles of Ti/Fe Multilayers	127
6.4 Stress Evolution in Ti/Fe Multilayers.....	130
6.5 Stress Evolution in 30 nm/10 nm and 10 nm/30 nm Ti/Fe	133

CHAPTER 1

INTRODUCTION

1.1 Motivation

1.1.1 Phase transformations in multilayered thin films

Material structures with large surface area-to-volume ratios can exhibit size dependent physical and chemical properties that are different than their bulk form [1,2]. These properties are enabling new devices with exceptional functionality to be developed including magnetic sensors [3], semiconductors [4], high density storage capacities [5] and energy storage devices [6]. Some of these changes are related to the material adopting a different crystallographic phase from the bulk and whose phase stability is size dependent. To fully exploit nanomaterials, the dimensional stability of such phases must be determined.

Multilayers are an ideal architecture to study phase stability of materials because thin films exhibit large interfacial-to-volume ratios that can be readily controlled through layer thickness. The structural and chemical nature of the interfaces can easily be modified through the sequence of deposition of different contact compositions, growth temperatures, and deposition energies [7]. During deposition, these thin films experience significant stress states [7,8,9] that exceed elasticity limits for their bulk counterparts. Such stress conditions likely control and/or influence the stability of the phases formed within these films. The interconnection of phase equilibrium and intrinsic growth stresses remains a fertile area of research.

Often phase transformations in the nanometer regime are serendipitously discovered with the stability criteria difficult to ascertain. For example, in Co/Cr multilayers, Boher *et al.* [10] reported that Co changes its phase from hcp to bcc while Vavra *et al.* [11] reported a change of Cr from bcc to hcp [11]. This leads to a confusion that which layer undergoes a phase transformation. In the Co/Cr multilayer, the phase was linked to the magnetic performance for giant magneto-resistance recording device. Since structure controls properties, the ability to understanding the contributing factors of phase stability are essential.

1.1.2 Approaches to understand phase stability in multilayers

In general, the prediction of phase stability has been explained using both strain induced transformation concepts [12,13] and classical thermodynamics [14,15,16,17]. In the former model, the film transforming layer achieves a metastable condition as the lattice parameter undergoes strain, as shown in **Fig. 1.1(a)**. This metastable phase is a different phase than that of the bulk and is at a local energy minimum whose energy is higher than the bulk phase. For example, the face centered cubic (fcc) to body centered cubic (bcc) transformation in Cu [18,19] has been explained through a Bain-based strain mechanism. As shown in **Fig. 1.2**, with a compression on [001] direction, the fcc Cu undergoes a martensitic transformation to form bcc. As the volume of the film is reduced, via a thinner layer thicknesses, the material becomes more susceptible to compliance induced strains that can drive a phase transformation.

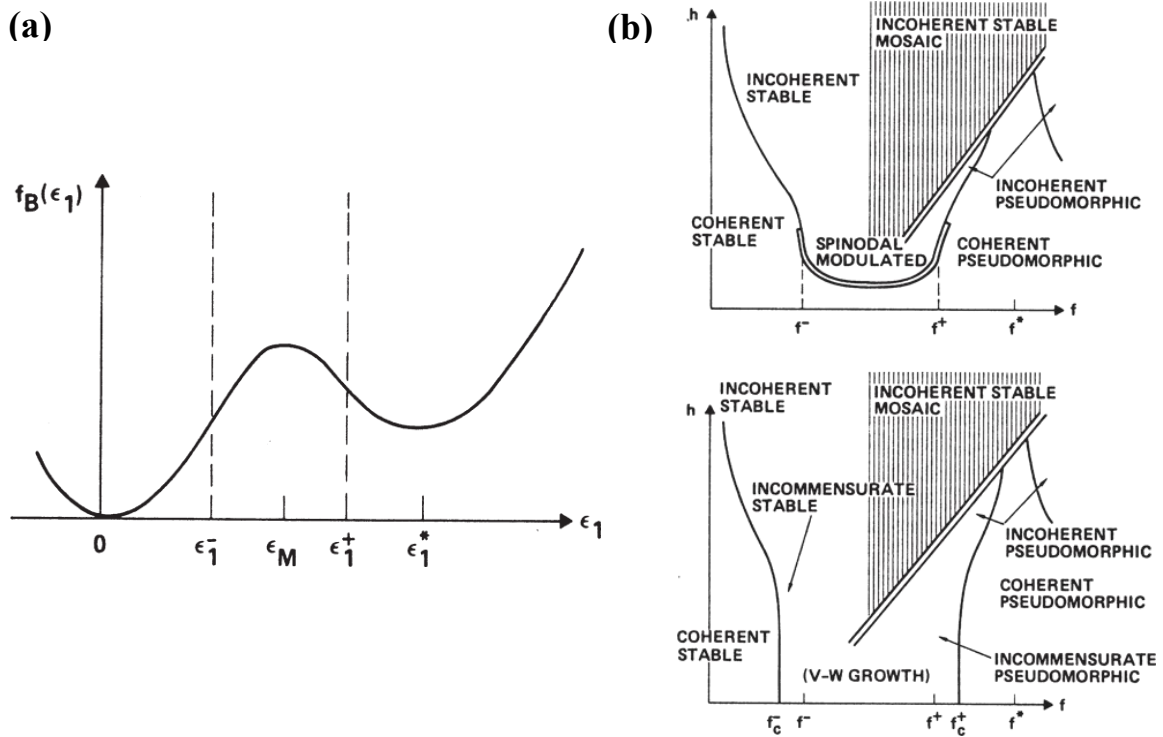


Fig. 1.1 (a) The changes in the free energy function, f_B , for a materials with strain, ϵ . Local minimums may exist along the free energy curve for specific curve for specific values of strain, ϵ^* . These minimums in free energy correspond to metastable phase structures [12]. (b) Structural phase diagram as a function of film height, h , and misfit, f . The upper figure is for strong film-substrate adhesion while the bottom figure is for weak substrate substrate-film adhesion [12].

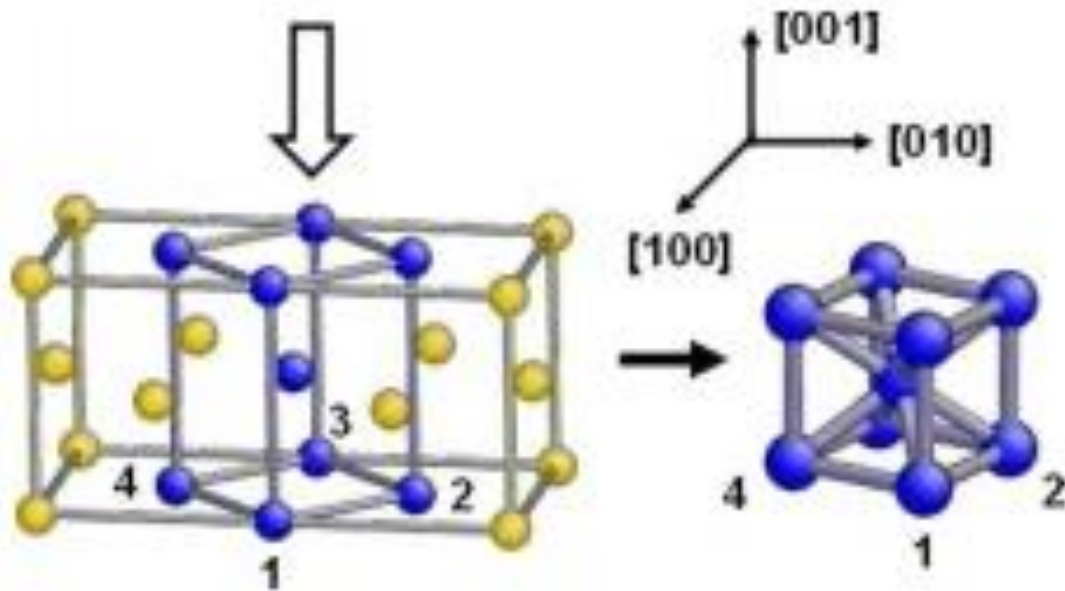


Fig. 1.2 Schematic of Bain strain induced martensitic transformation in fcc Cu [18]. As a compressive force is applied along the $[001]$ direction, the atoms (highlighted in blue) shown in the fcc Cu will eventually form a bcc structure.

In the thermodynamic approach for phase stability [14,15,16,17], the reduced layer thickness results in the interfacial energy contribution dominating the volumetric energy penalty for the phase transformation. Hence, from a thermodynamic prospective, the change in phase is placing the system at its equilibrium condition considering the balance of the interfacial and volumetric energies. This new phase is then referred to as a pseudomorph as it's not explicitly at a higher (but local minimum) energy state, which is the definition of metastability. Though this is a minor definition distinction between pseudomorphic and metastability, it is significant in how one considers and approaches the underlying mechanisms that contribute to phase stability.

In either case, the thin film stress is critical and would have a significant impact in the phase transformation process. The stress results in a strain (the prior model) which would change the energies due to the bond displacement in either the volumetric or interfacial terms (latter model). Thompson *et al.* reported a transitional behavior in the hcp to bcc transformation for Zr in Zr/Nb [15] which was related to coherency strains in the thermodynamic model. In the hcp to bcc Ti transformation in Ti/Nb, significant Nb was noted to interdiffuse into the Ti which could also be related to possible stress assisted diffusion [16]. The role of stress and its interrelationship to the thermodynamics of phase stability requires a much more detailed experimental investigation.

The present research will elucidate the underpinnings of phase stability by using a series of nanoscale thin film multilayers as its case study architecture. Model metallic Ti/bcc multilayers whose length scales and compositions are controlled with near atomic processing precision employed. By selecting different bcc layers, the influence of lattice misfit, layer thickness, surface energy, and the hcp to bcc stability can to be determined in relationship to these former strain and thermodynamic based models. Real-time, *in situ* growth stresses are measured and correlated to the interfacial stress evolution and intermixing across the layers. This work aims to delineate how

intrinsic film stress drives compositional intermixing across interfaces which can thermodynamically promote phase transformations.

1.2 Prediction of Phase Stability in Multilayered Thin Films

As noted above, different models have been proposed to explain phase stabilities in multilayers. Redfield *et al.* [20] developed a model based on interface-induced modifications to bulk stacking fault energies [20] in Ti/Al multilayers, but this model only considered phase stability consisting of close-packed lattice structures (i.e. fcc and hcp) with similar lattice parameters. It is relatively easy for either fcc and hcp to transform to the other phase by introducing stacking faults. Besides its limited use to certain crystal symmetries, the model was not conducive for the development of simple phase diagrams that one can use to readily identify when phase transformations occur. Bruinsma and Zangwill [12] proposed a series of phase diagrams, **Fig. 1.1 (b)**, based on the idea lattice strains driving films to metastable conditions and spinodal decompositions. Though more useful than the Zangwill approach, these diagrams have not been readily used in subsequent work to explain or even predict phase transitions.

Arguably, Dregia *et al.* [14] use of a thermodynamic phase diagram has had more success in its application to explaining and predicting phase changes in thin films [14]. The model is based on a multilayered structure of A/B layers, shown in **Fig. 1.3**. The phase stability is determined by a competition between the volumetric energy increases, ΔG_v , from the bulk stable to pseudomorphic phase versus the interfacial energy reduction, $\Delta\gamma$, for this transformation. The thickness for each individual layer is h_A and h_B , shown in **Fig. 1.3** with the bilayer thickness, λ , given by

$$\lambda = h_A + h_B \quad (1)$$

The volume fraction, f_i , multiplied to λ yields the thickness of that particular layer. The Gibbs free energy change for a phase transformation, normalized by the constant surface of the film, Δg , would be

$$\Delta g = 2\Delta\gamma + (\Delta G_A h_A + \Delta G_B h_B) \quad (2)$$

This equation describes the balance between the competing energy terms.

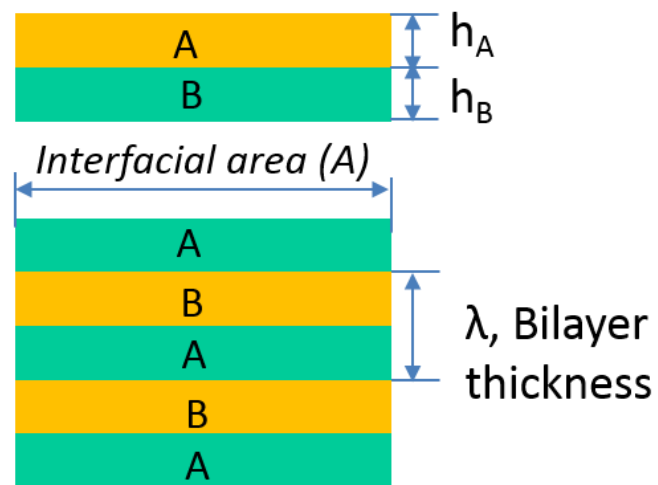


Fig. 1.3 A/B multilayered thin film stack, h_A and h_B is the thickness for each individual layer.

When a layer thickness becomes sufficiently thin, alternatively the volume reduced, the $\Delta\gamma$ value dominates ΔG_v and the new phase is stabilized. By plotting the volume fraction, f_i , versus the inverse bilayer spacing, λ^{-1} , a phase diagram is constructed on where transitions occur in either layer, as shown in the example Zr/Nb system of **Fig. 1.4**. This phase diagram has been successfully applied to a number of multilayers including, Zr/Nb [15], Ti/Nb [16], Ti/Al [21], Co/Cr [22] and Mg/Nb [17].

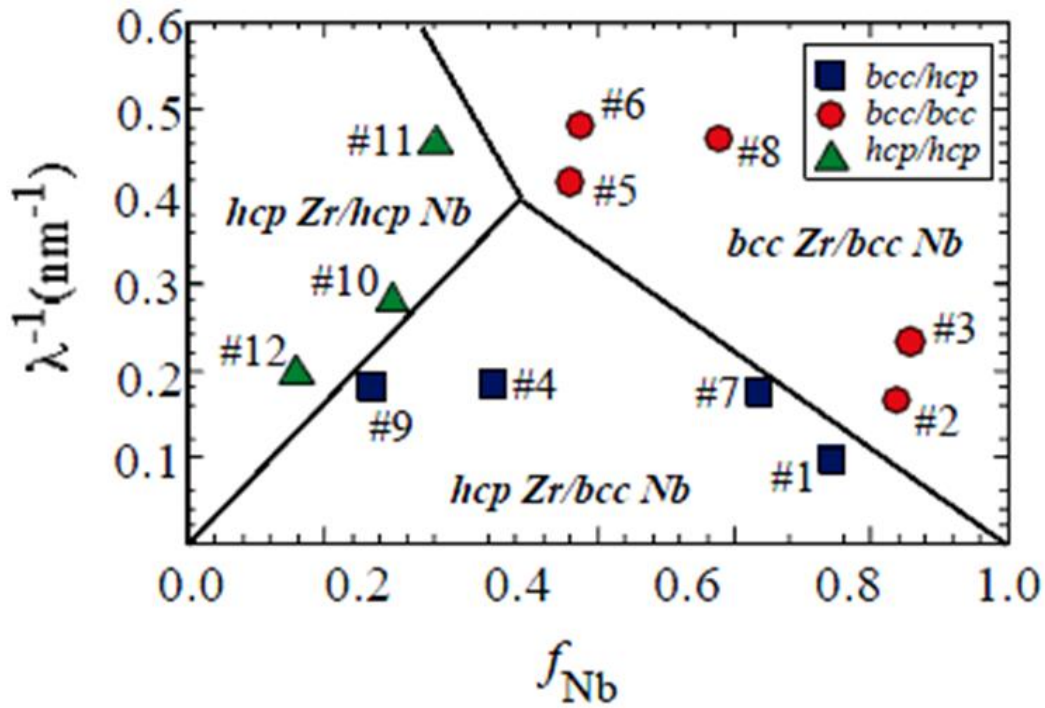


Fig. 1.4 Zr/Nb multilayer phase diagram. “G.B. Thompson. *Appl.Phys.L.* 84 (7)1083 (2004)” [15]

1.3 Stress Evolution in Multilayered Thin Films

1.3.1 Origins of stress in thin films

When a thin film grows on a substrate or underlayer film, intrinsic stresses are generated. These stress will alter the thermodynamic energies of the system and provides the connection between the strain induced and thermodynamic based approaches described above. To understand the stress formation within a growing film, consider the stress generation of a single layer. A generic cartoon of this thin film's stress evolution is plotted in **Fig. 1.5**. It is generally accepted that the initial compressive stress at the first stage of growth is a result of the atomic-scale migration of adatoms into embryonic islands [23,24] that form to minimize surface area to volumetric energies as the atoms nucleate. The subsequent tensile stress originates from the elastic strain associated with the coalescence of these islands to minimize the grain boundary energy. Elemental films with low atomic mobility, such as Fe, Cr, and Al, tend to retain the tensile condition with continued growth unless acted upon by external stimuli, such as thermal energy. For films with atoms of higher intrinsic mobility, such as Cu, Nb and Ti, they exhibit a return to compressive stress in the post coalescence condition. The mechanism of post-coalescence compressive stress is still under discussion [25,26,27,28] with Chason *et al.* [29,30] proposing that extra atoms, driven by differences in surface and grain boundary chemical potentials during deposition, cause the atoms to move into and out of grain boundaries creating the compressive stress. All of these stresses can be captured by measuring the substrate bending moments creating by the growing film using a laser reflection technique. [31]

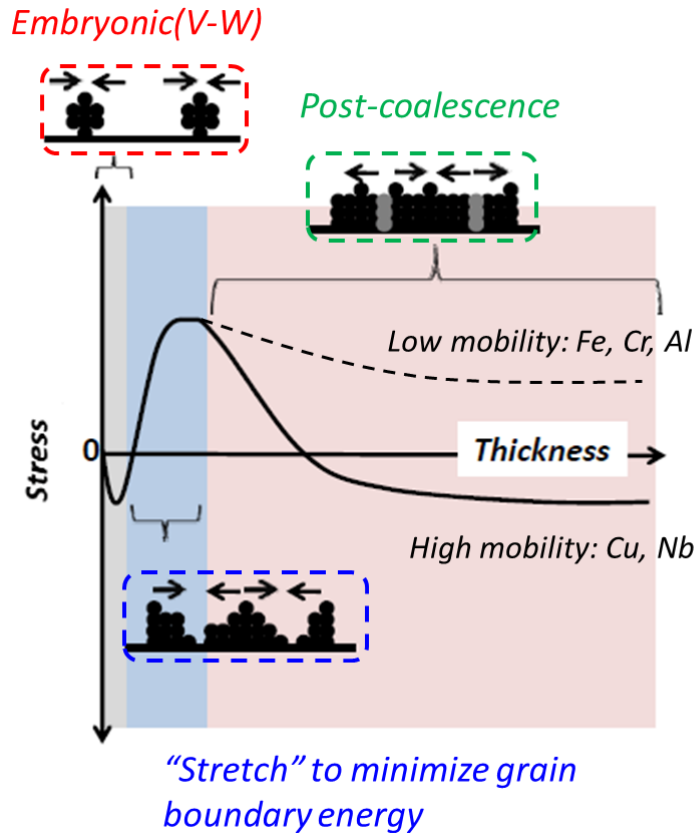


Fig. 1.5 A schematic cartoon of the generic stress evolution during thin film growth.

1.3.2 Interfacial stresses in multilayered thin films

Shull and Spaepen have applied the measurements of single film stress growth to that of multilayered films. In their pioneering work using Ag/Cu multilayers, they were able to deduce how the overall stress of a film changed with layering and how the stress between the layers changed during growth, **Fig. 1.6**. [32]. These stress states were used to deduce atomic mobility [24] of each film on the other, where a tensile state is related to low adatom mobility and compressive state to higher adatom mobility. The interfacial stress of each layer was determined by comparing how the stress changed when on layer grew on the other. This measurement was achieved by extrapolating the slope of the stress-thickness product data to zero thickness of the

new layer and determining the difference between the absolute stress-thickness product value at the end of the initial layer and that of the new layer [32].

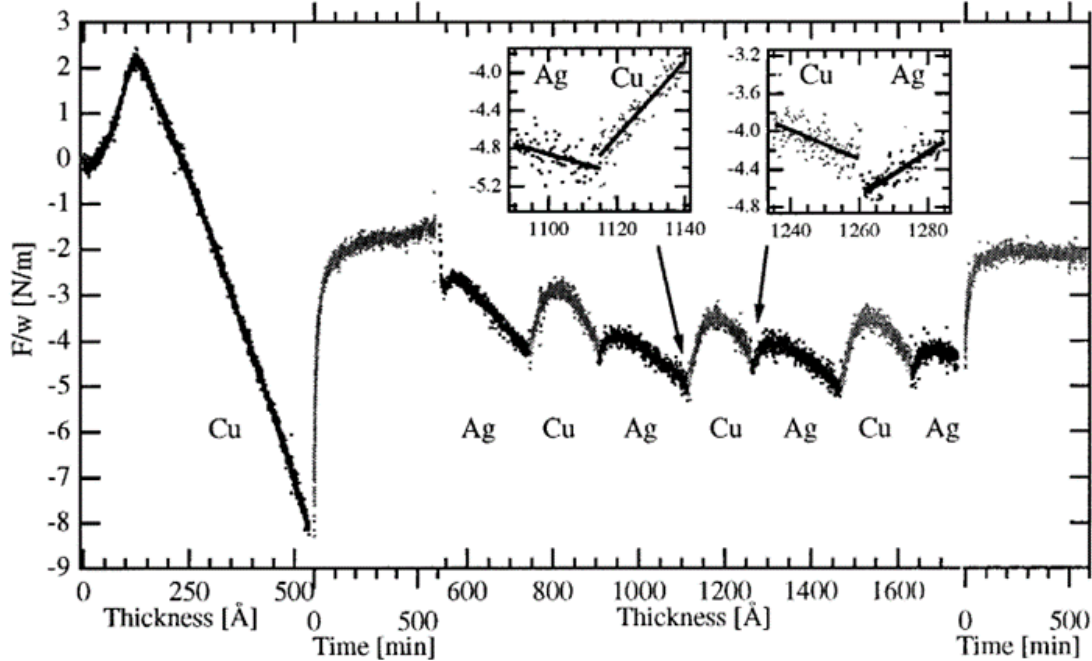


Fig. 1.6 Growth stresses in Ag/Cu multilayer [32]

The interfacial stress measurements, in Ag/Cu system, revealed that the tensile stress of the new layer growing on the previously deposited layer was dependent on the immediate contact surface and not the collective stress state of the film. This implied that the growth surface for the new deposits is critical in regulating the growth stresses for the new depositing layer. Since Ag and Cu are both fcc phases, no phase transformation to another crystal structure would be expected.

Unlike Ag/Cu, the proposed Ti/bcc system is expected to undergo an α -Ti (hcp) to β -Ti (bcc) transformation [16]. To date, it is not known how such a change in phase may influence the growth stress (adatom mobility). Moreover, prior reports have shown that significant Nb interdiffuses into the Ti layer which could also alter the adatom mobility [16]. Through the use of

in situ stress measurements, the influence of the phase growth surface as well as the interfacial compositional stability (intermixing) via stress changes will be explored. The results of which will help to explain how film growth is altered by interfacial energy reduction and strain. This will bridge our knowledge gaps between strain induced and thermodynamic driven phase transformations.

1.4 Materials Selection for BCC Template

The Ti/bcc multilayer systems to study comprise bcc templates of Nb, W, V, and Fe. Each bcc layer provides for (1) variations in strain at the interface with the subsequent misfit dislocation network differences and (2) a difference in chemical bonding across the interface (surface energy). Hence the selection of these different bcc metals allows for a wide range of experimental variables to study. The lattice misfit between bcc Ti and the bcc metals are tabulated in **Table 1**, using the equation

$$m_0 = (a_{bcc} - a_{Ti}) / a_{Ti} \quad (3)$$

where a_i is the lattice parameter. Since Ti/Nb has been shown to be coherent [16], the choice of W, V, and Fe allows the degree of misfit to be changed to investigate differences between purely coherency driven transformations and those associated with semi-coherent driven transformations. Differences in surface energy can be studied by comparing similar bcc templates that yield the same strains, *e.g.* V and Fe with Ti.

From their respective phase diagrams [33], bcc Ti has partial to complete solubility with each of these bcc template layers. In the following chapters, the compositional intermixing across these interfaces and within the bulk of the film will be measured using atom probe tomography to understand how such mixing changes as a function of lattice matching, phase stability, and stress

evolution during growth. Clearly, the coherency strain and the phase state of these multilayers should result in some discernable differences in intermixing.

Table 1.1. Lattice misfit and surface energies of Ti and bcc metals

	Lattice parameter(Å)	Lattice mismatch to bcc Ti (%)	Young's Modulus(GPa)	Melting Point(K)	Surface energy RT (J/m ²)
hcp Ti	a=b=2.95 c=4.68		116	1941	2.57
bcc Ti	3.3065	0	N/A	N/A	N/A
Nb	3.3066	0.003	105	2750	2.983
W	3.16	-4.431	411	3695	3.468
V	3.03	-8.362	128	2183	2.876
Fe	2.87	-13.201	211	1800	2.939

1.5 Thin Film Deposition and Structural Characterization

1.5.1 Sputter deposition

The thin films will be grown in an AJA ATC-1500 stainless steel sputtering chamber that is evacuated by mechanical and turbo-molecular pumps with a load lock for the retrieval of specimens. The substrate can be rotated during deposition to yield $\pm 2\%$ thickness uniformity. The base pressure of the chamber is $< 1 \times 10^{-8}$ Torr. There are four 2 inch magnetron sputtering guns with variable power supplies automated with LabView to regulate deposition rate.

The sputtering chamber is also equipped with the k-Space ® Multi-beam Optic Stress Sensor (MOSS) that provides *in situ* wafer curvature measurements. This provides real-time stress evolution during growth and the opportunity to relate the intrinsic growth stresses to phase stability and the post growth characterization. During deposition, various forces and moments are experienced as atoms nucleate and coalesce on the substrate causing the substrate to bend. The relationship that connects the curvature change of the substrate to the film stress is given by the Stoney equation [34]

$$\sigma_f = \frac{E_s}{6(1-\nu_s)} \frac{t_s^2}{t_f} \left(\frac{1}{R} - \frac{1}{R_0} \right) \quad (4)$$

where σ_f is the film stress, E_s is the Young's modulus of the substrate, ν_s is Poisson's ratio for the substrate, t_s is the substrate thickness, t_f is the film thickness and $1/R_0$ and $1/R$ are measured curvatures of the film before and during/after deposition, respectively. From this equation, changes in curvature are proportional to the product of the mean film stress and the film thickness, if the film thickness is much less than the substrate thickness [35].

1.5.2 X-ray reflectivity (XRR) and X-ray diffraction (XRD)

XRR is used to analyze the x-ray reflection intensity curves from grazing incident x-ray beam to determine thin film properties including thickness, density and surface and/or interface roughness [36]. In this research, XRR is crucial in determining the deposition rate of each species upon depositing the multilayers, as the thickness of each individual layer needs to be precisely controlled. The XRR scans are performed on Philips X'pert XRD with a $\text{CuK}\alpha$ source, followed by a curve fitting of the intensity profile. XRD provides a global characterization of the phase content, texture and lattice strain in the thin films sample. The Bragg-Brentano geometry determines that only the highly textured growth orientation's diffraction condition is met.

1.5.3 Transmission Electron Microscopy (TEM)

TEM provides the structural information from both plan-view and cross-section samples. Selected electron diffraction (SAD) patterns taken from plan-view samples are used to determine the phase constitution in the thin films. High-resolution TEM (HRTEM) images are used to determine the interface structure and can be correlated to the independently measured real-time growth stresses. These interface strains are also coupled to the degree of intermixing characterized by atom probe tomography. STEM-High Angle Annular Dark Field (HAADF) images are used to ascertain the interface roughness/intermixing as this imaging mode is created by atomic number (Z) scattering and gives a chemical based image of the sample analogous to a backscattered electron image in a SEM. In this imaging mode, the collected intensities are relatively insensitive to Bragg scattering (crystallography) but scale with a near Z^2 dependence with the atomic number.

1.5.4 Atom Probe Tomography (APT)

The atom probe tomography (APT) provides a 3D reconstruction of the atomic positions of the thin films and can assist in quantifying the chemical distribution at the interfaces and within the ‘bulk’ of the film. It works by applying a high voltage pulse to a specimen tip that has radius of curvature of ~ 50-100 nm where upon atoms on the surface field evaporate [37]. The needle-like specimens are prepared using the FIB by milling a hemispherical-shape tip from specimens mounted to planar Si posts following a lift-out procedure. Details can be found in reference [38]. The tips were run in Cameca Instruments Local Electrode Atom Probe (LEAP) 3000XSi, in either voltage or laser mode depending upon the parameters most advantageous for the evaporation of the varying compositions and bilayer thickness. The collected data were reconstructed using the IVAS software platform 3.6.8.

1.6 Dissertation Layout

This dissertation is composed of seven chapters. Chapter 1 provides a background introduction of phase stability and stress evolution in thin film multilayers. Approaches of modeling the phase transformation by strain-induced concept and thermodynamic biphasic diagram have been briefly reviewed. The idea of how to correlate the *in situ* stress measurements and the phase stability in a series of Ti/bcc multilayers has been brought.

Chapter 2 discusses the allotropic hcp to bcc phase transformation of Ti in Ti/Nb multilayers. The transition thickness is confirmed using electron diffraction. The *in situ* stress measurement technique is used to monitor the intrinsic growth stresses for a series of multilayers with various bilayer thicknesses. This stress slope transition has been related to the bcc to hcp Ti transformation. Atom probe tomography has been utilized to show the grain boundary segregation

as well as the intermixing across the interfaces. A molecular dynamic deposition model was found helpful in explaining the experimental findings.

Chapter 3 is mainly focused on investigating the kinetic path for phase stability in Ti/Nb multilayers. With the dynamic nature of the deposition process, the kinetic path for the phase transformation is not readily apparent through experiments. Hence, Molecular Dynamic (MD) simulations of thin film growth processes has been shown to be a powerful tool in understanding the subsurface phase transformation and how the underlayer/toplayer impacts pseudomorphic phase evolution.

Chapter 4 aims to elucidate the interrelationship of growth stress evolution with a possible Ti phase transformation in Ti/W thin film multilayers. The critical transition thickness for Ti has been determined by both XRD and electron diffraction. STEM-HAADF image was shown to examine the interface roughness as well as intermixing. The stress states for each film, during film growth, was rationalized by the lattice matching of the phase with the growth surface.

Chapter 5 talks about the phase transformation and *in situ* stress evolution in Ti/V multilayered thin films. The mobility of each species are manifested in the growth behavior, i.e. stress slope of one on each other. XRD peak shift was observed and used to measure the out-of-plane stress. Cross-sectional HRTEM imaging was performed to determine the orientation relationship of the Ti/V multilayer.

Chapter 6 is a study of the phase transformation and the influence of the underlayer thickness on the growth stress behavior in Ti/Fe multilayers. This thickness-dependent stress behavior were explained through a mobility change of the species.

Chapter 7 concludes the previous chapters and highlights the key findings under the frame of this dissertation. Possible directions related to the current progress of this research are also given as the future work.

Chapter 8 are appendices. An example is given for interfacial stress measurements in Appendix A. Appendix B provides the MD code for the phase stability study of a Nb/Ti/Nb stack.

The simulation code was originally made by Dr. Xiao-xiang Yu and the simulation results have been shown in Chapter 2, 3 and 4.

1.7 References

- [1] Roco MC, Williams R, Alivisatos P. Nanotechnology Research Directions: IWGN Workshop Report. Vision for Nanotechnology R&D in the Next Decade 1999
- [2] Koch CC. Nanostructured materials: processing, properties and applications. William Andrew, 2006.
- [3] Shen J, Kirschner J. Surf.Sci. 2002;500:300.
- [4] Dai Y, Zhang Y, Li Q, Nan C. Chemical Physics Letters 2002;358:83.
- [5] Feng X, Hu Y, Zhai J, Wang C, Song S, Song Z. J.Appl.Phys. 2014;115:204303.
- [6] Bavykin DV, Friedrich JM, Walsh FC. Adv Mater 2006;18:2807.
- [7] Chuang C, Chao C, Chang R, Chu K. J.Mater.Process.Technol. 2008;201:770.
- [8] Koch R. Journal of Physics: Condensed Matter 1994;6:9519.
- [9] Miyamura A, Kaneda K, Sato Y, Shigesato Y. Thin Solid Films 2008;516:4603.
- [10] Boher P, Giron F, Houdy P, Beauvillain P, Chappert C, Veillet P. J.Appl.Phys. 1991;70:5507.
- [11] Vavra W, Barlett D, Elagoz S, Uher C, Clarke R. Physical Review B 1993;47:5500.
- [12] Bruinsma R, Zangwill A. Journal de physique 1986;47:2055.
- [13] Bruinsma R, Zangwill A. EPL (Europhysics Letters) 1987;4:729.
- [14] Dregia S, Banerjee R, Fraser H. Scr.Mater. 1998;39:217.
- [15] Thompson G, Banerjee R, Dregia S, Fraser H. Acta materialia 2003;51:5285.

- [16] Thompson G, Banerjee R, Dregia S, Miller M, Fraser H. *J.Mater.Res.* 2004;19:1582.
- [17] Li J, Liu W, Jiang Q. *Acta materialia* 2005;53:1067.
- [18] Pereira Z, da Silva E. *Physical Review B* 2009;79:115404.
- [19] Wu F, Narayan J. *Crystal Growth & Design* 2013;13:5018.
- [20] Redfield AC, Zangwill AM. *Physical Review B* 1986;34:1378.
- [21] Banerjee R, Ahuja R, Fraser HL. *Phys.Rev.Lett.* 1996;76:3778.
- [22] Li JC, Liu W, Jiang Q. *Acta Materialia* 2005;53:1067.
- [23] Friesen C, Thompson C. *Phys.Rev.Lett.* 2004;93:056104.
- [24] Cammarata R, Trimble T, Srolovitz D. *J.Mater.Res.* 2000;15:2468.
- [25] Abadias G, Fillon A, Colin JJ, Michel A, Jaouen C. *Vacuum* 2014;100:36.
- [26] González-González A, Polop C, Vasco E. *Phys.Rev.Lett.* 2013;110:056101.
- [27] Pao C, Foiles SM, Webb III EB, Srolovitz DJ, Floro JA. *Phys.Rev.Lett.* 2007;99:36102.
- [28] Shin JW, Chason E. *Phys.Rev.Lett.* 2009;103:056102.
- [29] Chason E, Sheldon B, Freund L, Floro J, Hearne S. *Phys.Rev.Lett.* 2002;88:156103.
- [30] Chason E, Shin J, Hearne S, Freund L. *J.Appl.Phys.* 2012;111:083520.
- [31] Taylor C, Barlett D, Chason E, Floro J. *The Industrial Physicist* 1998;4

- [32] Shull AL, Spaepen F. *J.Appl.Phys.* 1996;80:6243.
- [33] Massalski TB, Okamoto H, Subramanian P, & Kacprzak L. *Binary alloy phase diagrams.* ASM international, 1990.
- [34] Stoney GG. *Proceedings of the Royal Society of London.Series A, Containing Papers of a Mathematical and Physical Character* 1909:172.
- [35] Klein CA. *J.Appl.Phys.* 2000;88:5487.
- [36] Yasaka M. *The Rigaku Journal* 2010;26:2.
- [37] Seidman DN. *Annu.Rev.Mater.Res.* 2007;37:127.
- [38] Giannuzzi LA, Kempshall B, Schwarz S, Lomness J, Prenitzer B, & Stevie F. *FIB lift-out specimen preparation techniques.* In: *Introduction to Focused Ion Beams*, Springer, 2005. p. 201.

CHAPTER 2

PHASE STABILITY AND IN SITU GROWTH STRESSES IN TI/NB THIN FILMS

COPYRIGHT© 2014 Acta Materialia Inc. Published by Elsevier Ltd.

Phase Stability and *in situ* Growth Stresses in Ti/Nb Thin Films

L. Wan¹, X.X. Yu¹, and G.B. Thompson¹

¹The University of Alabama, Department of Metallurgical and Materials Engineering, Tuscaloosa, Alabama USA 35487-0202

Key words: Thin film, multilayer, phase transformation, *in situ* stress, grain boundary segregation

2.1 Abstract

The thin film growth evolution associated with changes in Ti's bcc to hcp phase transformations in Ti/Nb multilayered thin films is addressed. An *in situ* laser interferometer curvature measurement technique was used to monitor the intrinsic growth stresses for a series of these multilayers, with each multilayer having a different bilayer spacing but equivalent individual layer thickness. The initial Ti layer grows on Nb with a positive stress-thickness product slope up to ~2 nm, where upon it transitions to a slightly negative growth stress slope. This transition has been associated with the bcc to hcp Ti transformation. The Nb growth exhibited a significantly

steeper stress-thickness product slope regardless of the Ti phase state. The decreasing interfacial stress between the two layers contributed to a collectively more compressive stress state for the multilayer. Atom probe tomography revealed Ti segregation to the columnar grain boundaries and significant Nb intermixing into the bcc Ti layer, which is rationalized as a surface exchange process driven by interfacial thermodynamic considerations. Using a molecular dynamic deposition simulation, this intermixing was found to be paramount in stabilizing the bcc Ti layer to larger layer thicknesses.

2.2 Introduction

Material structures with large surface area-to-volume ratios exhibit size-dependent physical and chemical properties that are different than their bulk forms [1,2]. Some of these changes can be related to the material adopting a different crystallographic phase. Often these phase transformations in the nanometer regime are serendipitously observed. Dregia *et al.* reported a phase diagram which can predict these changes in multilayered thin film architectures [3]. The phase stability is determined by a competition between the volumetric energy increases, ΔG_v , versus the interfacial energy reduction, $\Delta\gamma$, for the transformation. When the layer thickness becomes sufficiently thin, alternatively the volume reduced because the surface area is fixed, the $\Delta\gamma$ value can dominate ΔG_v and a new phase, referred to as a pseudomorph, is stabilized. This phase diagram has been successfully applied to a number of multilayers including Ti/Al [4], Ti/Nb [5], Zr/Nb [6] and Mg/Nb [7]. In this prospective, the pseudomorph is at thermodynamic equilibrium or the lowest free energy state. Alternatively, other theories have suggested changes in phase are driven by coherency strains [8]. Since volumetric strain increases the free energy [9], these strain-induced transformations would be at a higher but local metastable energy state. In order to accommodate the influence of strain in the Dregia *et al.* model, the predicted phase

boundaries are easily modified by including the strain energy per unit area of the interface [10] and has been successfully shown to fit a semi-coherent to coherent transformation of α -Zr to β -Zr in a Zr/Nb multilayer [6]. Clearly, the interplay of interfacial energy reduction and strain has a significant impact on the stability of pseudomorphs in the nanoscale regime.

In this paper, we have applied a laser interferometry technique to measure the growth stresses as a multilayered thin film is deposited. In doing so, we aim to provide real-time analysis on how stress (alternatively strain) evolves as a function of film thickness, phase stability, and adatom mobility. Such *in situ* diagnostics can be used to infer the mobility of adatoms during the nucleation and growth of a thin film [11,12,13] and yield new insights to the underlying behavior of these nanoscale phase transformations. In such measurements, a tensile stress is associated with the grains within the film ‘stretching’ towards each other to reduce the grain boundary energy. Compressive stress, in the initial growth state, is associated with the nucleation of the adatoms coming together [14,15] whereas post-coalescence compressive stress is still debated [16,17,18,19]. This latter compressive stress has been hypothesized to be from adatoms migrating into grain boundaries creating this stress state [20,21].

Shull and Spaepen have used the technique to show the evolution of adatom growth in Ag/Cu multilayers [22]. Their results provided quantitative measurements of the interfacial stress of each layer. The interfacial stress measurements, in this system, revealed that the tensile stress of the new layer growing on the previously deposited layer was dependent on the immediate contact surface and not the collective stress state of the film. This implies that the growth surface for the new deposits is critical in regulating the growth stresses for the new depositing layer. Since Ag and Cu are both face centered cubic (fcc) phases, no phase transformation to another crystal structure would be expected. Unlike Ag/Cu, the Ti/Nb system has been reported to undergo a α -

Ti (hexagonal close placed, hcp) to β -Ti (body centered cubic, bcc) transformation [5]. To date, it is not known how such a change in phase may influence the growth stress (adatom mobility) behavior of either layer. Moreover, atom probe tomography of the β -Ti/Nb layers reveals significant Nb interdiffusion into the Ti layer [5]. Through the use of *in situ* stress measurements, the influence of the phase growth surface as well as the interfacial compositional stability (intermixing) will be explored. The results of which will help to elucidate how film growth is altered by interfacial energy reduction and strain.

2.3 Experimental and Computational Details

A series of Ti/Nb multilayers with varying bilayer thicknesses, from 20 nm to 4 nm, at a fixed 0.5 volume fraction were sputter-deposited onto Si [001] substrates in an AJA ATC-1500 sputtering chamber. The base pressure of the sputtering system was $< 10^{-8}$ Torr. Ultra-high purity Argon, with a flow rate of 10 standard cubic centimeters per minute, was introduced to 2 mTorr as the working gas. Total film thicknesses were approximately 200 nm. All the thin films were deposited at ambient temperature (~ 25 °C).

The sputter chamber is equipped with the k-Space multi-beam optic sensor (MOS) [23] that provided *in situ* substrate curvature measurements. The dependence of substrate curvature on the film stress is given by the Stoney equation [24]

$$\sigma_f = \frac{E_s}{6(1-\nu_s)} \frac{t_s^2}{t_f} \left(\frac{1}{R} - \frac{1}{R_0} \right) \quad (1)$$

where σ_f is the film stress, E_s is the Young's modulus of the substrate, ν_s is Poisson's ratio for the substrate, t_s is the substrate thickness, t_f is the film thickness and $1/R_0$ and $1/R$ are measured curvatures of the film before and during/after deposition, respectively. The growth rate of Ti (0.029 nm/s) and Nb (0.053 nm/s) was determined by measuring the film thicknesses by small angle x-

ray reflectivity (XRR) [25] and verified by transmission electron microscopy (TEM) cross-section micrographs, divided by the time of deposition. XRR was conducted on X'pert Philips diffractometer with Cu K_{α} radiation source at 40 kV and 30 mA.

TEM studies were conducted on FEI Tecnai F20 TEM. Plan-view foils were prepared and used to determine the phases within each multilayer. Plan view foils have been shown to be less susceptible to possible artifacts in the stabilization of pseudomorphic phases [10,26,27]. These plan-view TEM foils were prepared by cutting a 3 mm disc from the deposited wafer, back-side grinding the disk to less than 100 μm followed by dimpling with diamond abrasive to less than 12 μm and subsequently ion-milling to electron transparency. Ion-milling was performed at 4.0 keV in Gatan precision ion polishing system (PIPS) using Ar^+ ions. The cross-sectional TEM foils were prepared by a focus ion beam (FIB) lift out procedure [28] in either a FEI Quanta 3D dual electron-FIB or Tescan Lyra dual electron-FIB microscopes. A final 5 keV mill was done to reduce any potential Ga^+ implantation.

The multilayers were also characterized by atom probe tomography (APT). The atom probe tips were analyzed in a Cameca Scientific Instruments Local Electrode Atom Probe (LEAP[®]) 3000XSi. The tips were analyzed at a 60K base temperature, 0.5% evaporation rate, and 200 kHz voltage mode. Similar to the TEM cross-sectional foils, the atom probe tips were prepared by a FIB lift out technique [29] with a low keV clean-up step to reduce Ga^+ implantation into the tip surface. The reconstructions of the data followed the procedures as outlined in reference [30].

The experimental data was coupled to computational simulations of the deposition to provide insights on possible pathways for how the final structure and stress states were achieved, which can only be inferred from the experimental *in situ* stress measurements. The molecular dynamic (MD) simulations, which have been shown to be a powerful tool in investigating thin film

growth [31,32,33,34], were performed by utilizing the LAMMPS code [35] with the Ti-Nb binary embedded atom model potential found in reference . This potential uses a rapid-fitting procedure to generate an accurate representation of the binary potential from the existing single-element potentials [36]. The in-plane directions for the thin film model were periodic and the growth direction fixed. For the Nb polycrystal initial growth layer, $2 \times 2 \times 2$ grains were randomly produced by the Voronoi construction [37] in a $9 \text{ nm} \times 9 \text{ nm} \times 9 \text{ nm}$ simulation cell with the average grain size being 4.5 nm. During the deposition simulation onto the Nb polycrystalline layer, the incident atoms were given a kinetic energy, E_k , of 1 eV and injected normal to the surface at time intervals of 1 ps. The simulated deposition rate is faster than the experimental deposition rate because MD solves for atomic vibrations which must be less than the shortest lattice vibration, typically a Debye frequency. Therefore the simulation is accelerated to deposit enough atoms in the available computational time to reveal structural features. A virtual wall was used to re-sputter the atoms reflected by the initial growth layer with initial kinetic energy E_k to improve the simulation efficiency. During the deposition simulations, the lowest four layers of the initial growth layer were fixed to prevent movement of this layer by the incident atoms. The microcanonical ensemble (NVE) was used for all other layers. In the rest time, the velocity Verlet algorithm and Nosé-Hoover thermostat [38,39,40,41] were used to solve the motion equations for the atoms and control the system temperature at 300K. After deposition the structures were fully relaxed for 500 ps to equilibrium configurations. The outputs were visualized by OVITO software [42] and the phases were distinguished by the common neighbor analysis (CNA) method [43].

2.4 Experimental Results

Fig. 2.1(a) and **(b)** are representative cross-sectional TEM micrographs of a 10 nm/10 nm and 2 nm/2 nm Ti/Nb multilayers respectively. The image clearly demonstrates the layered

morphology of the multilayers with each interfaces relatively smooth and flat between each layer. The plan-view image of the 10 nm/10 nm multilayer shows in-plan grain size **Fig. 2.1(c)**. The dashed arrow in **Fig. 2.1(b)** directs the reader to a vertical columnar grain boundary within the stack. The plan-view diffraction patterns, **Fig. 2.1(d)** and **(e)**, confirm the hcp Ti/bcc Nb and bcc Ti/bcc Nb phases respectively in each multilayer. A tabulation for the phases for the Ti/Nb multilayers is given in **Table 2.1** and is in good agreement with previous literature [44]. It's worth to note that the earlier report of the hcp to bcc Ti transformation at 0.5 volume fraction was previously given at ~ 3 nm/3 nm by XRD and electron diffraction [5], but in these electron diffraction results it was found closer to ~ 2 nm/2 nm. Genç [44] provided follow-up cross-sectional high-resolution TEM images in an aberration corrected TEM of the prior reported specimen which revealed that the Ti layers were indeed closer to 2 nm/2 nm rather than the prior XRD satellite peak estimation of the bilayer spacing. This current work confirms that the layer thickness for the transformation appears to be closer to 2 nm/2 nm.

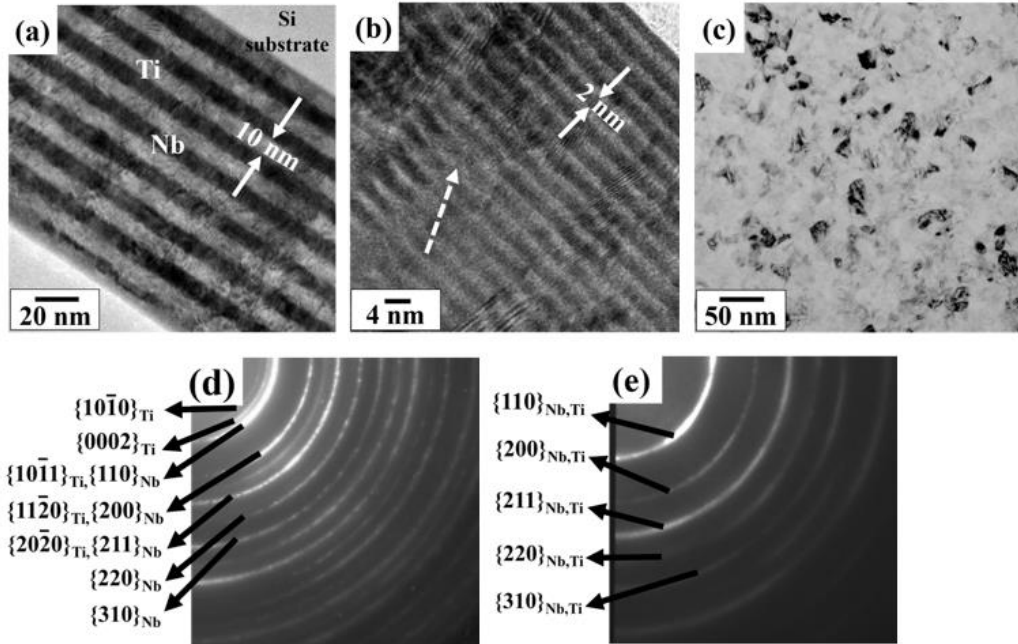


Fig. 2.1 (a) Cross-section TEM image of the 10 nm/10 nm Ti/Nb multilayer. (b) Cross-section TEM image of the 2 nm/2 nm Ti/Nb multilayer; the dashed arrow points to a columnar grain boundary. (c) Representative plan-view TEM image of the 10 nm/10 nm Ti/Nb multilayer. (d) Electron diffraction pattern taken in the plan-view orientation for the 10 nm hcp/10 nm bcc Ti/Nb multilayer. (e) Electron diffraction pattern taken in the plan-view orientation for the 2 nm bcc/2 nm bcc Ti/Nb multilayer.

Fig. 2.2(a) shows the evolution of the stress-thickness product for each of the multilayers. There are three main observations of note. First, as the thin films grow into the post-coalescence state [11], the stress-thickness product decreases indicating an overall increase in compressive stress with each subsequent layer. Second, as the bilayer thickness reduces, the film for an equivalent overall thickness becomes more compressive. Lastly, the absolute value of the stress-thickness product slope is steeper for the Nb layers than the Ti layers. **Fig. 2.2(b)** is the MD simulated stress plot for the 10 nm/10 nm hcp/bcc and 2 nm/2 nm bcc/bcc Ti/Nb multilayers. Compared to the experimental stress plot, the average stress is in the same order of magnitude and exhibits the same trends. Since the simulation assumed a single crystal growth surface whereas the experimental data is on a polycrystalline growth surface, where adatom migration to grain boundaries can also influence the stress behavior [20], and the simulation deposition rates are significantly faster for the reasons previously described, these may contribute to the differences in absolute values. Regardless of these differences, the model appears to reasonably capture the experimental behavior providing confidence in its simulation to yield insights into the growth behavior. Magnified images of the experimental curve, **Fig. 2.2(a)**, are shown in **Fig. 2.2(c)** and **(d)** for the 2 nm/2 nm and 10 nm/10 nm multilayer, respectively. The 2 nm/2 nm multilayer, **Fig. 2.2(c)**, has the pseudomorphic bcc Ti phase and a positive slope during Ti's growth over this thickness range. For the 10 nm/10 nm multilayer, **Fig. 2.2(d)**, the Ti layer has a positive slope over the same thickness where upon its transition to a slightly negative slope for thicknesses $> \sim 2$ nm. In contrast to the Ti slopes, the Nb layer, regardless of Ti phase state, has a steep, negative slope in stress-thickness product upon its deposition.

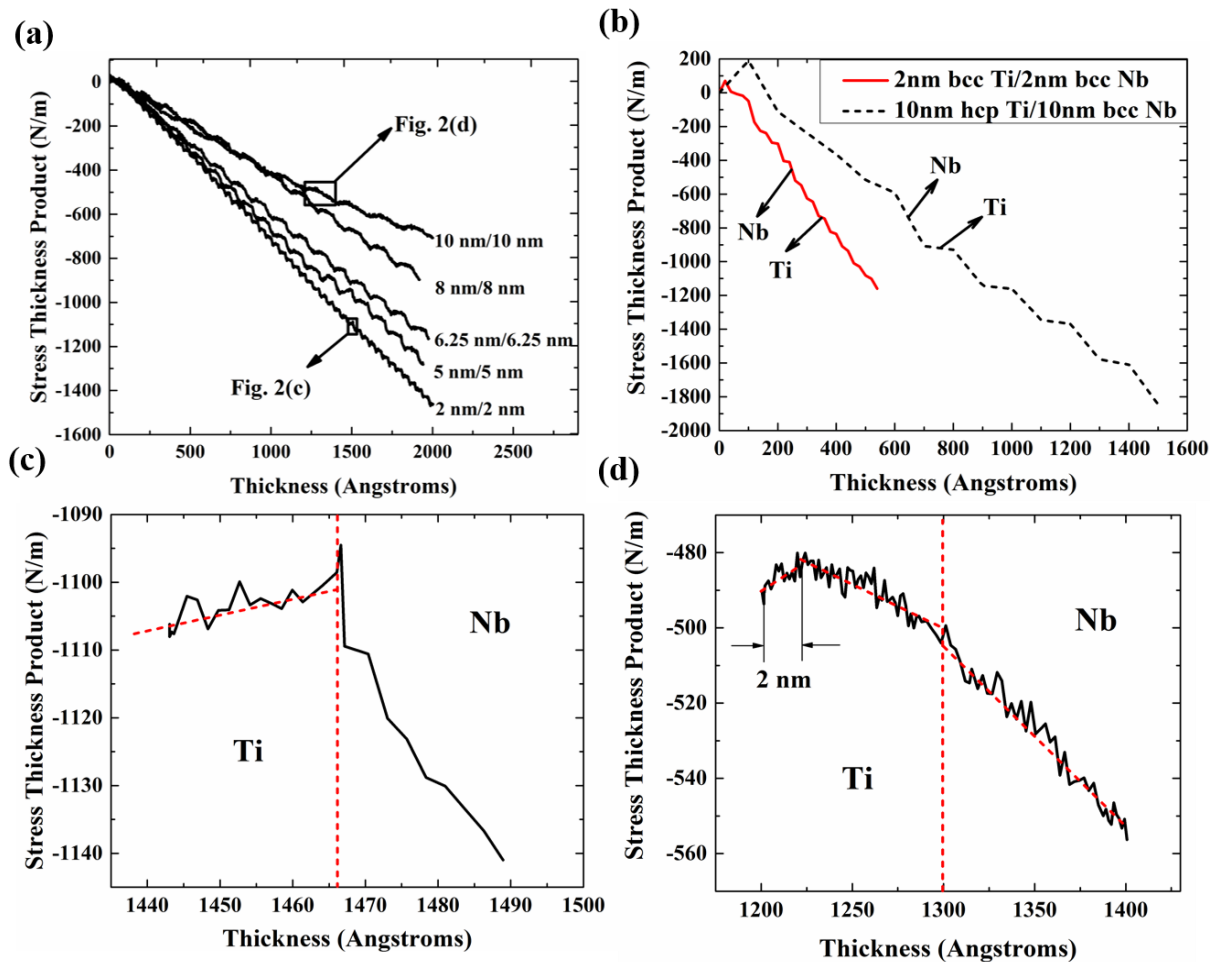


Fig. 2.2 (a) Stress evolution of the stress-thickness product versus thickness for various multilayers listed by their bilayer thickness. (b) MD simulated stress plot for the 10 nm hcp/10 nm bcc and 2 nm bcc/2 nm bcc Ti/Nb multilayers. (c) Magnified image of the experimental 2 nm bcc Ti/2 nm bcc Nb multilayer. Note the positive slope for the Ti growth. (d) Magnified image of the experimental 10 nm hcp Ti/10 nm bcc Nb multilayer. Note the initial positive than negative slope for the Ti growth.

The interfacial stress for each multilayer is tabulated in **Table 2.1**. These values are determined by subtracting the stress-thickness product value of the new, deposited layer extrapolated to zero thickness (i.e. initial state) against the value at the final thickness of the prior deposited layer [22]. The interfacial stress is divided into two thickness regions for the Ti growth based on the observed slope transition used for extrapolation to zero thickness. The average interfacial stress for the bilayer was computed by weighting each interfacial value by its thickness, i.e.

$$\Delta_{\text{avg}} = [(2 \cdot \Delta_{\text{Ti on Nb}} (< 2 \text{ nm}) + (t_{\text{Ti}} - 2) \cdot \Delta_{\text{Ti on Nb}} (> 2 \text{ nm}) + (\lambda - t_{\text{Ti}}) \cdot \Delta_{\text{Nb on Ti}})] / \lambda \quad (2)$$

where t_{Ti} is the individual thickness of the Ti layer (nm) and λ is the bilayer thickness or $t_{\text{Ti}} + t_{\text{Nb}}$, $\Delta_{\text{Ti on Nb}}$ or when $\Delta_{\text{Ti on Nb}}$ in the respective thickness range. The overall interfacial stress behavior decreased with decreasing bilayer thickness, which would also contribute to the overall compressive stress evolution of the film and will be discussed in Section 4.

Table 2.1. Interfacial stress values for various multilayers listed by their bilayer thickness

Number	Measured bilayer (nm)	Expected bilayer (nm)	Phase ID	Interfacial stress (N/m)	Average Interfacial stress (N/m)
1	20.17	20	hcp Ti /bcc Nb	$\Delta_{\text{Ti on Nb}} (< 2 \text{ nm}) = -2.91 \pm 0.16$ $\Delta_{\text{Ti on Nb}} (> 2 \text{ nm}) = 7.45 \pm 0.35$ $\Delta_{\text{Nb on Ti}} = -0.33 \pm 0.18$	2.52±0.25
2	14.08	16	hcp Ti /bcc Nb	$\Delta_{\text{Ti on Nb}} (< 2 \text{ nm}) = -4.20 \pm 0.20$ $\Delta_{\text{Ti on Nb}} (> 2 \text{ nm}) = 3.85 \pm 0.23$ $\Delta_{\text{Nb on Ti}} = 2.35 \pm 0.17$	2.09±0.19
3	12.53	12.5	hcp Ti /bcc Nb	$\Delta_{\text{Ti on Nb}} (< 2 \text{ nm}) = -5.45 \pm 0.15$ $\Delta_{\text{Ti on Nb}} (> 2 \text{ nm}) = 2.22 \pm 0.01$ $\Delta_{\text{Nb on Ti}} = 3.43 \pm 0.06$	1.59±0.06
4	9.90	10	hcp Ti /bcc Nb	$\Delta_{\text{Ti on Nb}} (< 2 \text{ nm}) = -6.77 \pm 0.13$ $\Delta_{\text{Ti on Nb}} (> 2 \text{ nm}) = 1.18 \pm 0.12$ $\Delta_{\text{Nb on Ti}} = 4.40 \pm 0.18$	1.20±0.15
5	3.96	4	bcc Ti /bcc Nb	$\Delta_{\text{Ti on Nb}} (< 2 \text{ nm}) = -9.49 \pm 0.21$ $\Delta_{\text{Ti on Nb}} (> 2 \text{ nm}) = \text{N/A}$ $\Delta_{\text{Nb on Ti}} = 4.65 \pm 0.21$	-2.42±0.21

The atom probe results are shown in **Fig. 2.3**. Significant differences in the compositional profile are revealed between the 5 nm/5 nm and 2 nm/2 nm multilayers, **Fig. 2.3(b)** vs. **2.3(f)**, with the latter multilayer exhibiting significant Nb interdiffusion into the Ti layer. This is in agreement with a prior report [5]. Unlike the prior atom probe findings [5], which were done in an older generation atom probe with field of views less than 15 nm, these new findings on the LEAP allow a wider field of view capturing the columnar grain boundary compositions within the layered stacking, **Fig. 2.3(c)-(d)** and **2.3(g)-(h)**, which reveals clear Ti segregation to the grain boundaries regardless of bilayer thickness.

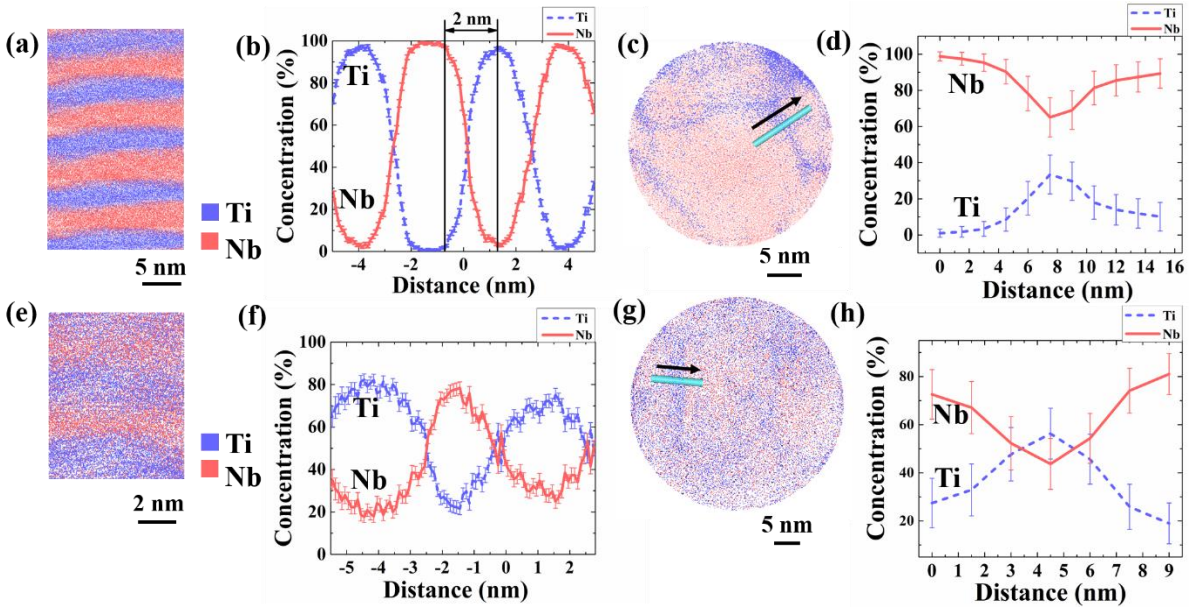


Fig. 2.3 (a) Atom ion map of the 5 nm hcp Ti/5 nm bcc Nb multilayer. (b) Proximate histogram of the 5 nm hcp Ti/5 nm bcc Nb multilayer along the growth direction. (c) Atom map of the plan-view slice of a 1 nm thick Nb layer. The map clearly shows Ti segregation to the grain boundaries. The cylindrical tube and arrow mark the region of interest from which the compositional profile is plotted in (d). (d) 1D profile of the ROI shown in (c). (e) Atom ion map of the 2 nm bcc Ti/2 nm bcc Nb multilayer. (f) Proximate histogram of the 2 nm bcc Ti/2 nm bcc Nb multilayer along the growth direction. (g) Atom map of the plan-view slice of a 1 nm thick Nb layer. The map clearly shows Ti segregation to the grain boundaries. The cylindrical tube and arrow mark the region of interest from which the compositional profile is plotted in (h). (h) 1D profile of the ROI shown in (g).

2.5 Discussions

In Dregia *et al.*'s [3] classic thermodynamic model, when the Ti layer in the bilayer transforms to the pseudomorphic state, the bilayer's total free energy change per area, Δg_T , is given as

$$\Delta g_T = 2\Delta\gamma + (\Delta G_{Ti}f_{Ti})\lambda \quad (3)$$

where $\Delta\gamma$ is the change in interfacial energy, ΔG_{Ti} is the volumetric free energy change per unit volume and f_{Ti} is the volume fraction of Ti in the bilayer (0.5, for this film). The hcp to bcc transformation will result in a positive increase in the volumetric free energy at room temperature and 1 atm. with the interfacial energy change, $\Delta\gamma$, being negative to stabilize the phase change. The experiments have confirmed the bcc β -Ti phase for the 2 nm/2 nm multilayer and the hcp α -Ti phase for the 5 nm/5nm multilayer.

The MD simulation of the Ti deposition onto the polycrystalline Nb substrate are presented in **Fig. 2.4**. **Fig. 2.4(a)-(f)** are colored by elements, allowing for easier visualization of the Nb substrate and Ti layer, where **Fig. 2.4(g)-(l)** are colored by the structure using the CNA method. **Fig. 2.4(a)** and **(g)** is the initial state with only the Nb layer. **Fig. 2.4(h)** shows a bcc Ti phase when Ti grows to 1 nm on the Nb substrate, **Fig. 2.4(b)**. When Ti grows up to 2 nm, shown in **Fig. 2.4(c)**, the Ti film starts to transform from bcc to hcp, **Fig. 2.4(i)**, evident by the onset of both bcc and hcp stacking within the Ti layer. By adding 2 nm of a bcc Nb top layer onto the 2 nm Ti film, **Fig. 2.4(d)**, the vast majority of the hcp Ti phase is no longer present in the dominate bcc Ti layer, **Fig. 2.4(j)**. The addition of this Nb top layer provides the second of the two interfaces for $\Delta\gamma$ given in equation (3) indicating that two bcc Nb interfaces is sufficient to stabilize the bcc Ti at 2 nm.

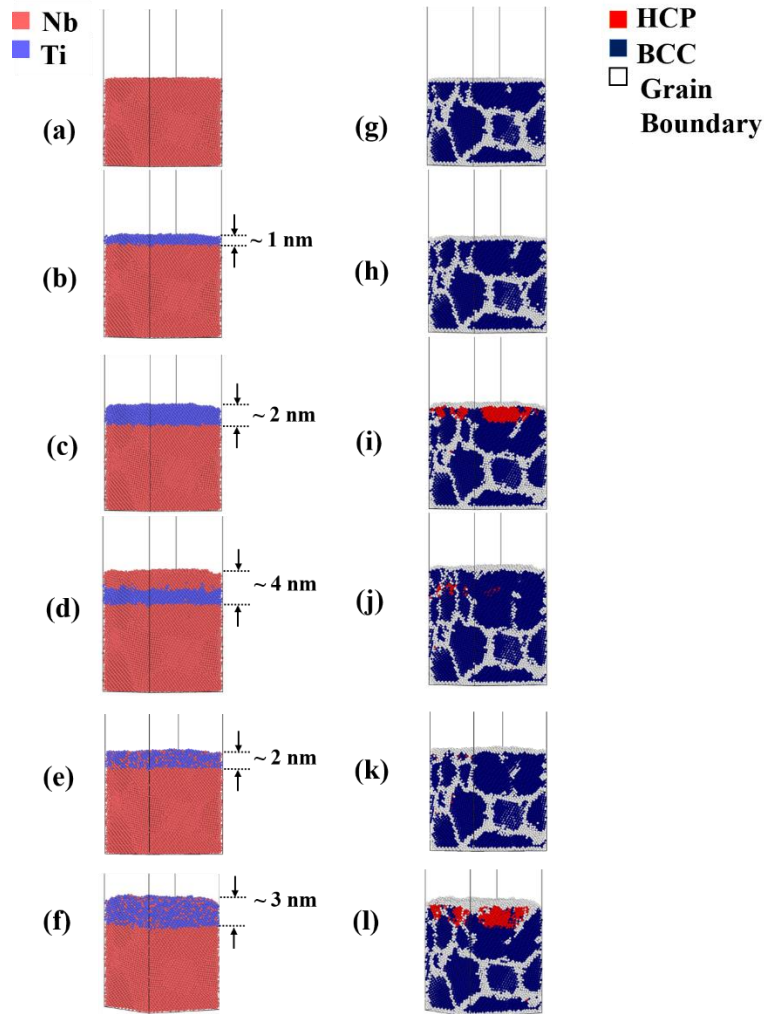


Fig. 2.4 (a) Initial state of the Nb substrate with no Ti deposition on the surface. (b) 1 nm of Ti on the Nb substrate. (c) 2 nm of Ti on the Nb substrate. (d) Addition of a 2 nm bcc Nb top layer onto the 2 nm Ti film on the Nb substrate. (e) 2 nm Ti layer with 20 at. % Nb intermixing on the Nb substrate. (f) 3 nm Ti layer with 20 at. % Nb intermixing on the Nb substrate. (g) Initial state of the bcc Nb substrate. (h) 1 nm of Ti grown on bcc Nb with Ti adopting a bcc structure. (i) 2 nm of Ti grown on bcc Nb with Ti predominately adopting the hcp structure. (j) 2 nm bcc Nb top layer on a 2 nm Ti film on a bcc Nb substrate with Ti adopting a bcc structure. (k) 2 nm of Ti intermixed with Nb grown on bcc Nb with Ti adopting a bcc structure. (l) 3 nm of Ti intermixed with Nb grown on bcc Nb with Ti adopting a predominately hcp structure.

Though two interfaces have been simulated, the real time stress of the Ti deposit shows the continual positive slope up to ~ 2 nm, **Fig. 2.2(c)**, without this second Nb surface, strongly suggestive that bcc Ti was stabilized to a larger layer thicknesses than predicted by MD. As will be discussed in detail below, bcc Ti will grow in a tensile state to match the bcc Nb subsurface layer. This tensile condition would manifest itself as a positive stress-thickness slope. This initial, positive slope was also observed to occur in the first ~ 2 nm of Ti in the 10 nm/10 nm film, **Fig. 2.2(d)**. Upon growing thicker, the stress-thickness product slope became negative indicative of a relaxation in the Ti film. This slope change is attributed to the phase transformation from bcc Ti to hcp Ti, as this was Ti's final phase characterized in the 10 nm/10 nm multilayer.

In **Fig. 2.3(f)**, significant Nb intermixing was noted in the bcc Ti stabilized film. In **Fig. 2.4(e)**, a 2 nm Ti layer was mixed with 20 at. % Nb. The resulting Ti layer, without the top Nb film, stabilized the bcc Ti phase, **Fig. 2.4(k)**. The increased intermixing of Nb, a β -stabilizer for Ti [45], reduced the ΔG positive energy penalty allowing the bcc Ti to be stabilized to a larger layer thickness. When the intermixed layer was simulated to ~ 3 nm thickness, **Fig. 2.4(f)**, the bcc phase was no longer stabilized and the presence of hcp Ti was found in the layer, **Fig. 2.4(l)**. This particular simulation provides additional confirmation that the positive slopes for Ti's stress-thickness plots in **Fig. 2.2(c)** and **(d)** were indeed the stabilization of bcc Ti, with further thickness increases resulting in the destabilization of bcc and the stabilization of hcp.

The change in positive to negative slope for the Ti growth layer, **Fig. 2.2(d)**, indicates a conversion in the film's stress state which would impact the interfacial energy change, $\Delta\gamma$. There are a number of different factors that contribute towards $\Delta\gamma$ including a chemical and a structural contribution [9]. The chemical component $\Delta\gamma^{\text{chem}}$ arises from the change in bonding across the interface and the structural component $\Delta\gamma^{\text{struc}}$ arises from the change in misfit at the interface

accompanying the phase transformation. With the phase transformation from bcc Ti to hcp Ti, the interface of Ti and Nb changed from a coherent bcc β -Ti/bcc Nb interface [5] to a semi-coherent hcp α -Ti/bcc Nb interface [46]. Note that β -Ti has a near equivalent lattice parameter to bcc Nb, 3.3065 Å (ICDD 00-044-1288) and 3.3066 Å (ICDD 00-035-0789) respectively. It is worth to note that the referenced β -Ti lattice parameter is the value at equilibrium (or high temperature). The β -Ti lattice parameter would undergo some amount of reduction at lower temperatures because of the nominal contraction associated with thermal expansion. By using the coefficient of thermal expansion and linear extrapolation to room temperature (298K), the lattice parameter was calculated as 3.2763 Å [47]. This room temperature β -Ti layer would undergo a tensile stress to be coherent with bcc Nb, which rationalizes the positive slope in the growth stress when it was deposited, **Fig. 2.2(c)** and **(d)**.

The orientation relationship of α/β Ti has been reported to be $\langle 11\bar{2}0 \rangle_{\alpha} // \langle 111 \rangle_{\beta}$; $\{0001\}_{\alpha} // \{011\}_{\beta}$ [5]. Considering this orientation relationship of hcp Ti on a bcc surface, a 3% misfit strain would now be present. As the bcc Ti layer grows, the strain is relieved by the transformation to the stable hcp Ti phase with its misfit dislocations at the interface. This change at the interface resulted in a compressive state for the hcp Ti film on Nb which is manifested by the change in slope during the hcp Ti growth phase.

The APT results of **Fig. 2.3** demonstrated a clear segregation of Ti into the columnar grain boundaries and even within the Nb layers. The preference of Ti in the grain boundaries provides clues on a possible atom exchange mechanism that can help rationalize the intermixing. Mezey *et al.*[48] have measured the surface free energy ratio of $\gamma_{\text{Nb}}/\gamma_{\text{Ti}}$ being 1.2, which suggests that Nb atoms would preferentially exchange with Ti across the interface in an attempt to enrich its surface in Ti to reduce its interfacial energy. In addition, Ti-Nb alloy formation energy decreases with Nb

composition [49]; or in other words, the thermodynamic driving force is greater for intermixing for bcc Ti and bcc Nb than for hcp Ti and bcc Nb. This is observed between the two APT results in **Fig. 2.3**. The Nb concentration within the bcc Ti layer, **Fig. 2.3(f)**, is ~ 20 at% as compared to Nb's concentration in the hcp Ti layer of ~ 2 at.% Nb, **Fig. 2.3(b)**. The latter alloy mixing is consistent with the binary phase diagram's low temperature solid solubility [50].

The enrichment of Ti in the grain boundaries is clear experimental confirmation of Ti's preference to interfaces in this system. Considering a growth surface is dynamical with a high concentration of point defects, a surface exchange mechanism, driven by thermodynamic energy considerations, appears feasible. Such atomic exchanges have been observed and simulated in CoFe/Cu multilayers [51] where intermixing occurred across the interfaces.

From **Fig. 2.3(b)** we can see that for 5 nm/5 nm multilayer, the intermixing between the two layers (intermixing width) is approximately 2 nm. As the Nb deposits, Ti will thermodynamically be driven to enrich its surface, but eventually this surface is overwhelmed with continual Nb deposition. As the Nb layer thickens, the amount of Ti intermixed into it is no longer present at the larger layer thicknesses. This initial intermixing at the growth surface could also explain the compositional overlap (lack of abrupt interfaces) for Nb's growth. Conversely, if Ti is growing on the Nb surface, one could expect a more abrupt surface since Ti would be the lower surface energy atom. To rationalize the intermixing width of Ti grown on the Nb surface one must consider Ti's segregation to the grain boundaries which would create site defects in the Ti layer. Such defects provide a vacancy concentration mechanism that could also promote intermixing that is driven by the compositional gradient at the interface. Clearly, the intermixing of species across interfaces, particularly during a dynamical event such as film growth, is complex with likely more than one event occurring simultaneously.

Finally, Chason *et al.* [20] has suggested that the infusion of excess adatoms at grain boundaries may be associated with the post-coalescence compressive stress. The presence of excess Ti in the grain boundaries, **Fig. 2.3**, would provide experimental confirmation of these concepts. The MD deposition simulations did not take into account segregation, rather elastic bonding behavior. By considering the lattice matching between the layers, the simulation was successful at capturing the overall compressive growth with decreasing by bilayer thickness. Though such segregation could be contributing to the post coalescence compressive stress, it appears to be a secondary effect based on the close matching of the MD simulation to the experiments, which did not account for such segregation effects.

The decreasing interfacial stress value with bilayer thickness, **Table 2.1**, also appears to help drive the greater compressive behavior observed in these multilayers. Upon the hcp to bcc Ti phase transformation, the average interfacial stress became negative or compressive. Other cubic on cubic phase multilayers [22,52] have shown compressive interfacial stress. This change from tensile to compressive interfacial stress in the Ti/Nb multilayers is believed to be a result of the crystallographic matching a semi-coherent hcp Ti/bcc Nb interface to a coherent bcc Ti/bcc Nb interface. The absolute values of the stress are dependent on the thickness of each layer in each phase state, as noted by the delineated stress values for Ti grown on Nb and Nb grown on Ti. The compressive interfacial stress for the 2 nm/ 2 nm multilayer may have also contributed to the minor wavy appearance of the layer pairs in cross-section, **Fig. 2.1(b)**, as a mechanism of stress relaxation as such a morphology was not qualitatively present in the thicker bilayer film, **Fig. 2.1(a)**. The ability to tune the interfacial stress state by the phase stability of the layer offers a potentially interesting means to engineer stress states in thin films and is the subject of future investigations.

2.6 Summary

During the initial growth of Ti on a Nb film surface, the Ti layer was stabilized as a bcc phase up to ~ 2 nm. This resulted in a tensile stress state for bcc Ti which was manifested as a positive stress-thickness product slope in the *in situ* stress measurements captured deposition. The tensile condition is a result of the slight bcc lattice contraction Ti undergoes from its high temperature β -Ti value. For films grown to thicker thicknesses, the Ti stress-thickness slope transitions to a slightly negative stress-thickness slope. This transition has been rationalized to be the bcc to hcp Ti transformation with its accompanying compressive misfit strain for hcp Ti on bcc Nb. The bcc Nb growth exhibited a significantly steeper stress-thickness product slope regardless of the Ti phase state.

The decreasing interfacial stress between the two layers contributed to a collectively more compressive stress state for the multilayer with decreasing bilayer thickness. Using a MD deposition simulation, the collective compressive stress of the multilayer, which showed reasonable agreement with experimental data, suggested that lattice matching between layers was a significant mechanism contributing to the overall stress evolution of these films.

APT revealed Ti segregation to the columnar grain boundaries in the multilayers and significant Nb intermixing into the bcc Ti layer. This partitioning was rationalized as a surface exchange process driven by interfacial thermodynamic considerations. The MD deposition simulation indicated that bcc Ti would be stabilized up to ~ 1 nm, but the coupling of the APT mixing results with modification to the simulated Ti layer revealed stabilization up to ~ 2 nm with intermixing and was consistent with experimental findings. The results of this work have provided new insights into the complex stress evolution and phase stability behavior in nanoscale thin films.

2.7 Acknowledgements

The authors gratefully recognize the National Science Foundation (Grant NSF-DMR-1207220) and the Central Analytical Facility in the University of Alabama for support. Dr. Xiaoxiang Yu also acknowledges the UA post-doctoral fellowship program.

2.8 References

- [1] Siegel RW, Hu E, Roco MC, Cox DM, Goronkin H. Nanostructure Science and Technology. A Worldwide Study 1999
- [2] Roco MC, Williams R, Alivisatos P. Nanotechnology Research Directions: IWGN Workshop Report. Vision for Nanotechnology R&D in the Next Decade 1999
- [3] Dregia S, Banerjee R, Fraser H. *Scr.Mater.* 1998;39:217.
- [4] Banerjee R, Ahuja R, Fraser HL. *Phys.Rev.Lett.* 1996;76:3778.
- [5] Thompson G, Banerjee R, Dregia S, Miller M, Fraser H. *J.Mater.Res.* 2004;19:1582.
- [6] Thompson G, Banerjee R, Dregia S, Fraser H. *Acta materialia* 2003;51:5285.
- [7] Li JC, Liu W, Jiang Q. *Acta Materialia* 2005;53:1067.
- [8] Bruinsma R, Zangwill A. *Journal de physique* 1986;47:2055.
- [9] Porter DA, & Easterling KE. *Phase Transformations in Metals and Alloys*, (Revised Reprint). CRC press, 1992.
- [10] Banerjee R, Zhang X, Dregia S, Fraser H. *Acta materialia* 1999;47:1153.
- [11] Spaepen F. *Acta Materialia* 2000;48:31.

- [12] Floro JA, Chason E, Cammarata RC, Srolovitz DJ. *MRS Bull* 2002;27:19.
- [13] Pletea M, Bruckner W, Wendrock H, Thomas J, Kaltofen R, Koch R. *J.Appl.Phys.* 2007;101:073511.
- [14] Friesen C, Thompson C. *Phys.Rev.Lett.* 2004;93:056104.
- [15] Cammarata R, Trimble T, Srolovitz D. *J.Mater.Res.* 2000;15:2468.
- [16] Abadias G, Fillon A, Colin JJ, Michel A, Jaouen C. *Vacuum* 2014;100:36.
- [17] González-González A, Polop C, Vasco E. *Phys.Rev.Lett.* 2013;110:056101.
- [18] Pao C, Foiles SM, Webb III EB, Srolovitz DJ, Floro JA. *Phys.Rev.Lett.* 2007;99:36102.
- [19] Shin JW, Chason E. *Phys.Rev.Lett.* 2009;103:056102.
- [20] Chason E, Sheldon B, Freund L, Floro J, Hearne S. *Phys.Rev.Lett.* 2002;88:156103.
- [21] Chason E, Shin J, Hearne S, Freund L. *J.Appl.Phys.* 2012;111:083520.
- [22] Shull AL, Spaepen F. *J.Appl.Phys.* 1996;80:6243.
- [23] Taylor C, Barlett D, Chason E, Floro J. *The Industrial Physicist* 1998;4
- [24] Stoney GG. *Proceedings of the Royal Society of London.Series A, Containing Papers of a Mathematical and Physical Character* 1909:172.
- [25] Sasanuma Y, Uchida M, Okada K, Yamamoto K, Kitano Y, Ishitani A. *Thin Solid Films* 1991;203:113.
- [26] Thompson GB. *Predicting polymorphic phase stability in multilayered thin films.* 2003.
- [27] Thompson G, Banerjee R, Fraser H. *Microscopy and Microanalysis* 2003;9:370.

- [28] Giannuzzi L, Stevie F. *Micron* 1999;30:197.
- [29] Thompson K, Lawrence D, Larson D, Olson J, Kelly T, Gorman B. *Ultramicroscopy* 2007;107:131.
- [30] Brons J, Herzing A, Henry K, Anderson I, Thompson G. *Thin Solid Films* 2014;551:61.
- [31] Pelliccione M, Lu T. *Evolution of Thin Film Morphology*, by M.Pelliccione and T.-M.Lu. Berlin: Springer, 2008. ISBN: 978-0-387-75108-5 2008;1
- [32] Zhou X, Wadley H. *Surf.Sci.* 1999;431:58.
- [33] Zhou X, Wadley H. *J.Appl.Phys.* 2000;87:8487.
- [34] Fu B, An W, Turner C, Thompson G. *Phys.Rev.Lett.* 2010;105:096101.
- [35] Plimpton S. *Journal of Computational Physics* 1995;117:1.
- [36] Ward L, Agrawal A, Flores KM, Windl W. arXiv preprint arXiv:1209.0619 2012
- [37] Li J. *Modell Simul Mater Sci Eng* 2003;11:173.
- [38] Martyna GJ, Tobias DJ, Klein ML. *J.Chem.Phys.* 1994;101:4177.
- [39] Parrinello M, Rahman A. *J.Appl.Phys.* 1981;52:7182.
- [40] Tuckerman ME, Alejandre J, López-Rendón R, Jochim AL, Martyna GJ. *Journal of Physics A: Mathematical and General* 2006;39:5629.
- [41] Shinoda W, Shiga M, Mikami M. *Physical Review B* 2004;69:134103.
- [42] Stukowski A. *Modell Simul Mater Sci Eng* 2010;18:015012.
- [43] Honeycutt JD, Andersen HC. *J.Phys.Chem.* 1987;91:4950.

- [44] Genc A. Phase stability in metallic multilayers. 2008.
- [45] Froes F, Bomberger H. JOM 1985;37:28.
- [46] Bhattacharyya D, Viswanathan GB, Denkenberger R, Furrer D, Fraser HL. Acta Materialia 2003;51:4679.
- [47] Touloukian Y, & Buyco E. Thermophysical Properties of Matter. The TPRC Data Series. A Comprehensive Compilation of Data by the Thermophysical Properties Research Center (TPRC), Purdue University. 5: Specific Heat. Nonmetallic Solids. Comp. by EH Buyco. IFI/Plenum, 1970.
- [48] Mezey L, Giber J. Jpn.J.Appl.Phys 1982;21:1569.
- [49] Raabe D, Sander B, Friák M, Ma D, Neugebauer J. Acta Materialia 2007;55:4475.
- [50] Moffat D, Kattner U. Metallurgical Transactions A 1988;19:2389.
- [51] Zhou X, Wadley H, Johnson RA, Larson D, Tabat N, Cerezo A et al. Acta materialia 2001;49:4005.
- [52] Zhang X, Misra A. J.Appl.Phys. 2004;96:7173.

CHAPTER 3

ELUCIDATING TI'S SUB-GROWTH SURFACE PHASE TRANSFORMATION IN NB/TI/NB NANOLAMINATES

To be submitted for publication

Elucidating Ti's Sub-growth Surface Phase Transformation in Nb/Ti/Nb Nanolaminates

L. Wan¹, X.X. Yu¹, and G.B. Thompson¹

¹The University of Alabama, Department of Metallurgical and Materials Engineering,

Tuscaloosa, Alabama USA 35487-0202

3.1 Abstract

As the thickness of a thin film is decreased, the interfacial structure becomes paramount and crystals can undergo phase transformations. Molecular dynamics (MD) simulations have been performed to capture how such transformation could occur under the growth surface of a film. An hcp to bcc transition in Ti for Ti/Nb multilayers was used as the case studies. The simulations had good agreement with experiments. The simulations further predicted a mixed phase state for Ti for particular equal layer thicknesses.

3.2 Introduction

Materials structures with large surface area-to-volume ratio such as thin films can exhibit size dependent physical and chemical properties [1,2] that are different from their bulk form. These properties enable new devices with exceptional functionality to be developed including capacitors [3,4], optical switches [5,6] and magnetic sensors [7,8]. Many of these changes are related to the material adopting a different crystallographic structure [9,10,11]. In multilayered thin films, the stability of different phases have been investigated through thermodynamic approaches [12,13,14,15] by determining the lowest energy configuration. However, the kinetic path that allows that phase to be achieved is not readily apparent. Since the growth of thin film is a very dynamic process [16], it is critical to understand how it impacts pseudomorphic phase evolution. In this letter, we provide Molecular Dynamic (MD) simulations of thin film growth to understand possible sub-growth surface phase transformations.

According to Dregia *et al.*'s classic thermodynamic model [12] for phase stability in a multilayered thin film, the stabilization is governed by a competition between volumetric and interfacial energy penalties. In the multilayer stacking of two species, the layer thickness of each can be represented as the volume fraction of that layer multiplied to the combined or bilayer spacing of both layers. Using this bilayer construction, the relative thermodynamics can then be easily expressed in terms of the volumetric and interfacial energies within the bilayer. For example, consider the growth of Ti/Nb, our case study for this letter. Here we will fix the volume fraction of each layer to be 0.5 or equal layer thicknesses where it has been previously reported [14,17] that hcp Ti adopts a bcc Ti phase. This could be expected as Ti undergoes a α -hcp to β -bcc polymorphic transformation with temperature in the bulk form. Here, as a multilayer, the total free

Gibbs energy change per area in the bilayer, Δg_T , has only one degree of freedom, which is the bilayer thickness λ . This is expressed fully as

$$\Delta g_T = (\Delta G_{Ti} \cdot 0.5)\lambda + 2\Delta\gamma \quad (1)$$

where ΔG_{Ti} is the volumetric free energy change from α to β and $\Delta\gamma$ is the interfacial energy change with that change in phase at the interface. The two represents the interface below and above the Ti layer that is in contact with Nb. The deviation from the equilibrium α -hcp phase to β -bcc will result in an energy penalty or positive change in volumetric energy. This is offset by the reduced interfacial energy change, which must be negative, to stabilize the pseudomorphic bcc Ti at ambient temperature and atmosphere.

One of the outstanding questions concerning this model and predictions for transformations [13,18] would be the possibility that the phase transformation occurs after its growth and below the new growth surface. According to equation (1), strictly speaking, the stabilization of the pseudomorphic phase requires two interfaces. During its growth, in this case Ti, it would only be in contact with one bcc Nb interface. Only upon ceasing the deposition and the growth of a new Nb layer on the now deposited Ti surface would the second interface be manifested to Ti. This would imply the possibility that Ti could grow and adopt an hcp phase only to undergo a bcc transformation at a later stage of growth of the film. As such an experimental *in situ* study would be difficult, we have explored the use of a MD simulation to study when the transformation in Ti would occur for various bilayer thicknesses. Simulations of thin film growth processes present an attractive and unique means to gain a deeper insight into this phase stability. Using the computational information, we performed post-mortem diffraction analysis of selected experimental films to verify and validate the MD predictions. Through correlated computational

and experimental approaches, the behavior between the hcp and bcc transformation in Ti/Nb can then be more fully realized.

3.3 MD Simulations of 2 nm Ti/2 nm Nb Multilayer

The MD simulations were performed using LAMMPS [19] code with the embedded atom method (EAM) potential model [20] used for the Ti-Nb system from reference [21]. Periodic boundary conditions was used for the two in-plane coordinate directions or growth surface to minimize the effect of small length scales in these two particular directions. To simulate the growth, a free boundary condition was used for the third coordinate direction. Vapor deposition is then simulated by continuously injecting adatoms towards the free surface of the crystal at a frequency determined by the deposition rate. Because MD simulations solves for atom vibrations, the time step must be less than the shortest lattice vibration period (typically a Debye frequency of around 10^{-15} sec.). Consequently, an accelerated rate of deposition is used in order to deposit enough atoms in the available computational time to reveal structural features [22]. To prevent the simulated crystal from shifting because of the momentum transfer during adatom impact, several monolayers of atoms at the other free surface are fixed. Further details of the simulation can be found in reference [17].

The MD simulation of the Ti deposition (up to 2 nm) onto the polycrystalline Nb substrate is illustrated in **Fig. 3.1**. The top subfigures are colored by the element while the bottom subfigures are colored by the crystallographic structures using the common neighbor analysis (CNA) method. **Fig. 3.1(a)** is the initial condition of the simulation, i.e. the Nb substrate. As the Ti grows to 1 nm, **Fig. 3.1(b)**, the Ti remains as a bcc structure. As Ti continues to grow to 2 nm, **Fig. 3.1 (c)**, a large portion of the Ti layer has now adopted the bulk stabilized hcp phase. This reveals that Ti

thicknesses much greater than 1 nm are too thick to stabilize the pseudomorphic phase. As discussed above, the pseudomorphic stabilization can occur if the Ti is placed in contact with another bcc Nb surface. To determine if this occurs in our simulation, we deposited a 1 nm of Nb onto the 2 nm hcp Ti layer. Upon placing Ti into contact with this new surface, **Fig. 3.1(d)**, the Ti indicates some hcp destabilization evident by the mixed hcp and bcc coordination within its layer. Upon further increasing the Nb layer to 2 nm, the Ti layer is nearly fully stabilized bcc, **Fig. 3.1(e)**. It is interesting to note that the few remnant regions of hcp coordination in this bilayer are qualitatively located at the initial Nb/Ti growth surface. This simulation confirms the prior thermodynamic model in that two interfaces can and indeed stabilize the pseudomorph. In the MD simulation this transformation occurred under the growth surface.

To this point, our MD simulation did not account for intermixing within the layers. Prior reports from experimentally deposited films characterized by atom probe tomography revealed that Nb intermixes into the Ti layer to approximately 20 at. %. The details of this intermixing and characterization can be found in references [14,17]. Using this information, we have refined the simulation to now include a Ti layer that has 20 at. % Nb. Here, the 2 nm Ti-20 at. % Nb layer is able to stabilize the bcc phase at 2 nm without the need for the additional Nb surface contact, **Fig. 3.2(f)**. Assuming the intermixed Ti-20 at. % Nb layer is a regular solution, the entropy of the mixing can then be written as

$$\Delta S_{mix} = -nR(a \ln a + b \ln b) = -nR(a \ln a + (1-a) \ln(1-a)) \quad (2)$$

Since a is less than 1 in a binary mixing system, ΔS_{mix} is positive. For this intermixed layer, the thermodynamic stability is also dependent on the formation enthalpy. Rabbe *et al.* [23] has employed ab initio simulations to Ti-Nb alloy systems and reported that the formation energy is always negative when Nb concentration are higher than 20 at. %. Thus this mixing reduced the

volumetric energy change penalty for the β phase stabilization. Upon depositing the 2 nm Nb layer onto the surface of this bcc Ti-20at. % Nb layer, the Ti, as would be expected, retained the bcc phase while in contact with two Nb interfaces.

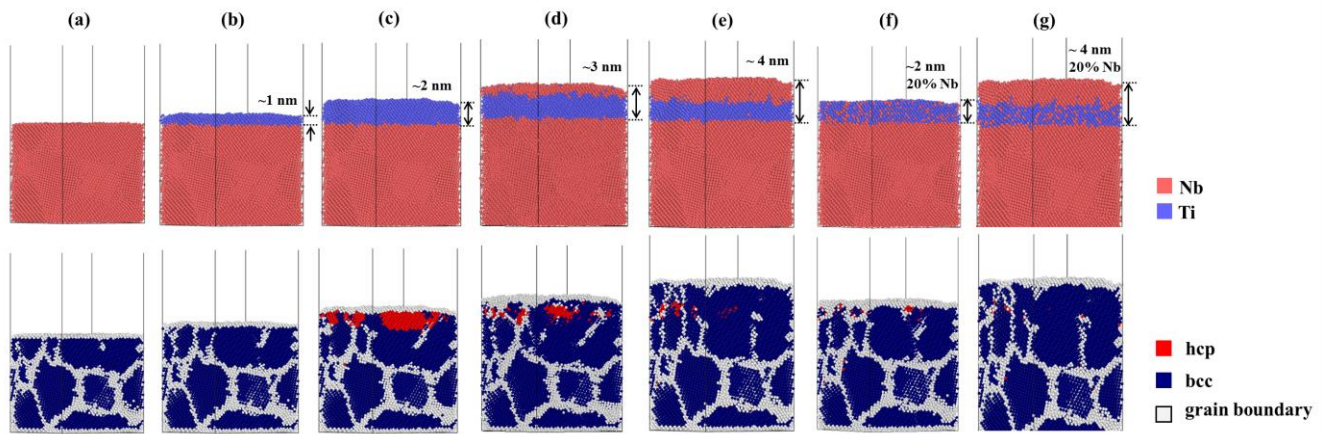


Fig. 3.1 MD simulation of 2 nm Ti/2 nm Nb multilayer deposition onto Nb substrate. Top figures are distinguished by element species and bottom figures are distinguished by structures **(a)** Initial Nb substrate. **(b)** 1 nm Ti on Nb. **(c)** 2 nm Ti on Nb. **(d)** 1 nm Nb on 2 nm Ti. **(e)** 2 nm Nb/2 nm Ti on Nb. **(f)** 2 nm Ti (with 20 at. % Nb mixing) on Nb. **(g)** 2 nm Nb/2 nm Ti (with 20 at. % Nb mixing) on Nb. **Fig. 3.1(a)-(f)** has been published on Acta Materialia, Volume 80, page 490-497, 2014.

3.4 MD Simulations of 3 nm Ti/3 nm Nb Multilayer

In **Fig. 3.2**, we now investigate the phase stabilization of the Ti-20at. % Nb or what will be referred to as the mixed Ti layer, which is more representative to the prior experimental findings. **Fig. 3.2(a)** reveals that as the mixed Ti layer reaches ~ 3 nm, the bcc phase destabilizes and the majority film's crystallography adopts the hcp structure. By growing ~ 0.5 nm of Nb onto this surface, portions of the intermixed Ti layer qualitatively appear to show more bcc stabilization, **Fig. 3.2(b)**. Further incremental increasing of the Nb thickness up to ~ 3 nm reveals this bcc stabilization in the mixed Ti layer, **Fig. 3.2(c)-(g)**. Comparing the equivalent bilayer fraction between the ~ 3 nm mixed Ti/ ~ 3 nm Nb, **Fig. 2(g)**, to the ~ 2 nm mixed Ti/ ~ 2 nm Nb, **Fig. 3.1(g)**, the mixed Ti layer qualitatively appears not to yield a complete bcc stabilized phase as compared to its thinner thickness counterpart. To quantify this change bcc and hcp coordination of the mixed Ti layer, **Fig. 3.3(a)** quantitatively reveals how the bcc and hcp coordination of the Ti changes with increasing Nb layer thickness on its surface. For comparison the values for the ~ 2 nm mixed Ti layer at the initial condition (i.e. no Nb top surface) and at its equivalent layer thickness of a ~ 2 nm Nb top surface are also included on this plot. As the Nb layer grew on the ~ 3 nm mixed Ti layer, the mixed Ti stabilized a larger fraction of its atoms as bcc. However, this bcc stabilization is not complete throughout the ~ 3 nm of Nb top surface growth. The largest extent of bcc stabilization occurred within the first ~ 1.5 nm of Nb growth on the ~ 3 nm mixed Ti surface. Arguably, the majority of prior literature on multilayer phase transformations has suggested that these layers are either all or not transformed. This simulation provides new insight that the transformations, within a single layer, may be mixed phase. Since the very thin Ti layers can undergo a transformation, the coordination of the Nb layer on the ~ 3 nm mixed Ti surface is also plotted in **Fig. 3.3(b)**. Here the majority of the Nb atoms adopt an hcp coordination at layer

thicknesses less than 1 nm. Thompson *et al.* has reported for very thin Nb in Zr/Nb multilayers hcp Nb stabilization [13].

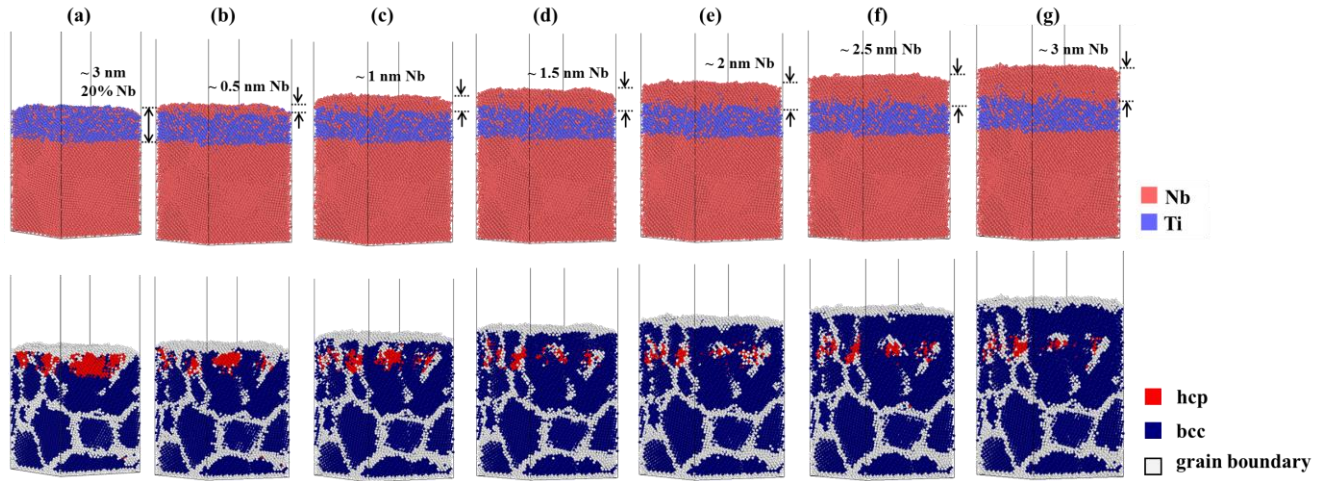


Fig. 3.2 MD simulation of 3 nm Ti/3 nm Nb multilayer deposition. The Nb layer thickness is increased at a 0.5 nm interval up to 3 nm. **(a)** Initial 3 nm mixed Ti layer on Nb. **(b)** 0.5 nm Nb on 3 nm mixed Ti layer. **(c)** 1 nm Nb on 3 nm mixed Ti layer. **(d)** 1.5 nm Nb on 3 nm mixed Ti layer. **(e)** 2 nm Nb on 3 nm mixed Ti layer. **(f)** 2.5 nm Nb on 3 nm mixed Ti layer. **(g)** 3 nm Nb on 3 nm mixed Ti layer. **Fig. 3.2(a)** has been published on *Acta Materialia*, Volume 80, page 490-497, 2014.

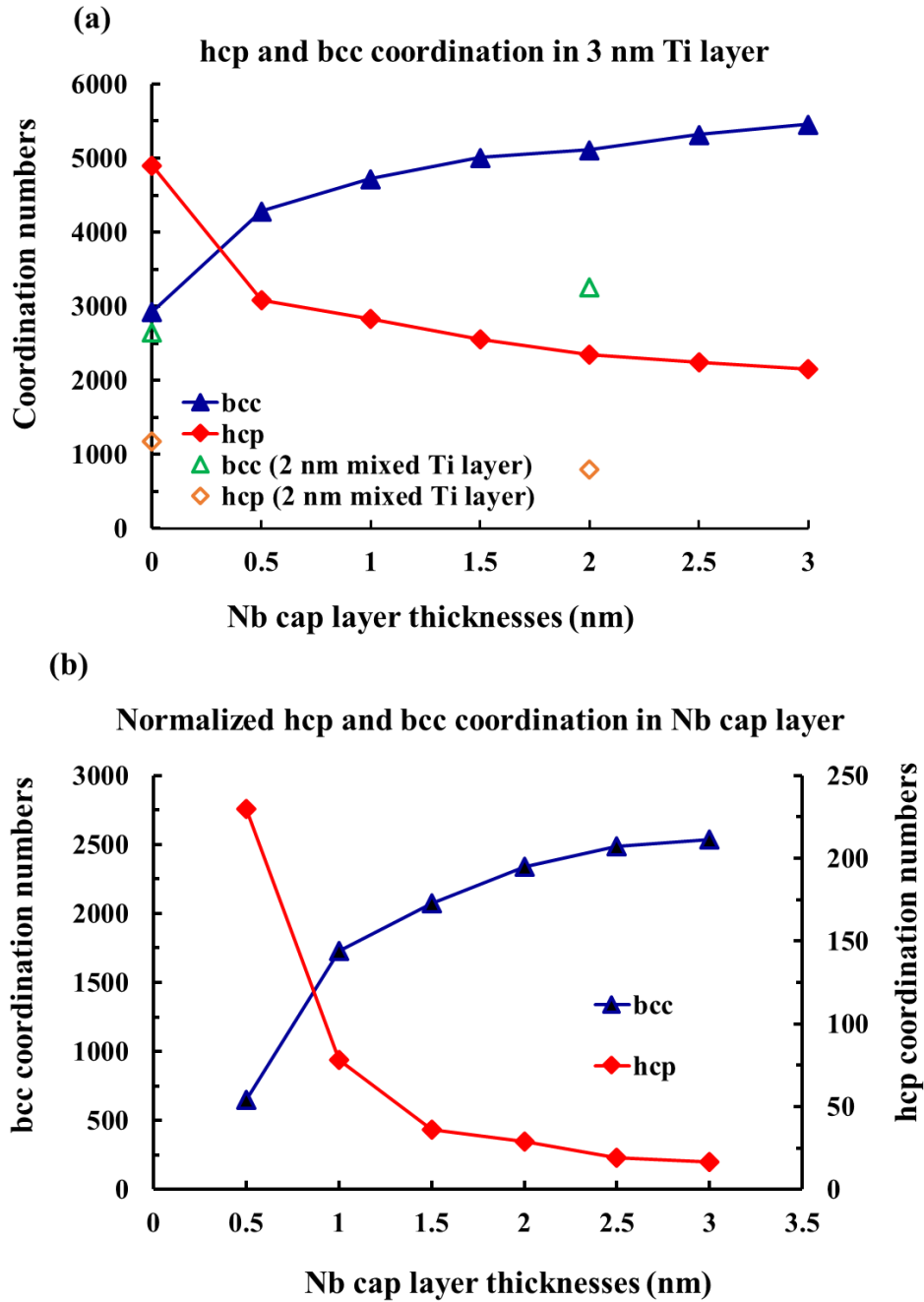


Fig. 3.3 (a) hcp and bcc coordination numbers in the 3 nm Ti layer. The bcc and hcp coordination numbers in 2 nm mixed Ti layer were also plotted for comparison. (b) Normalized hcp and bcc coordination numbers in Nb top layer versus Nb top layer thickness in the 3 nm Ti/3 nm Nb multilayer.

3.5 Experimental Confirmation of BCC Ti

To confirm that the hcp phase (or a portion thereof) is indeed stabilized for a 3 nm Ti/3 nm Nb multilayer, such a film was sputter deposited under the conditions reported previously [17]. Since this film was grown in a manner similar to the prior report, the intermixing between the layers occurred. We note that the growth of Ti/Nb on a completely different sputtering system revealed similar and reproducible levels of intermixing [14]; this intermixing appears to be a common feature of this multilayer regardless of the chamber from which it is sputtered. The Transmission Electron Microscopy (TEM) plan view and cross-sectional images are shown in **Fig. 3.4(a)-(b)**. The inset diffraction pattern in the plan view orientation for the experimental film does indeed show the hcp Ti phase reflections. For comparison, the 2 nm Ti/2 nm Nb plan view and cross-sectional image is given in **Fig. 3.4(c)-(d)** and its inset diffraction pattern revealed only bcc stabilization (note the clear absence of the $\{10\bar{1}0\}$ reflection seen in the prior pattern). These experimental diffraction reports confirm the prior simulation findings in **Fig. 3.1 and 3.2**.

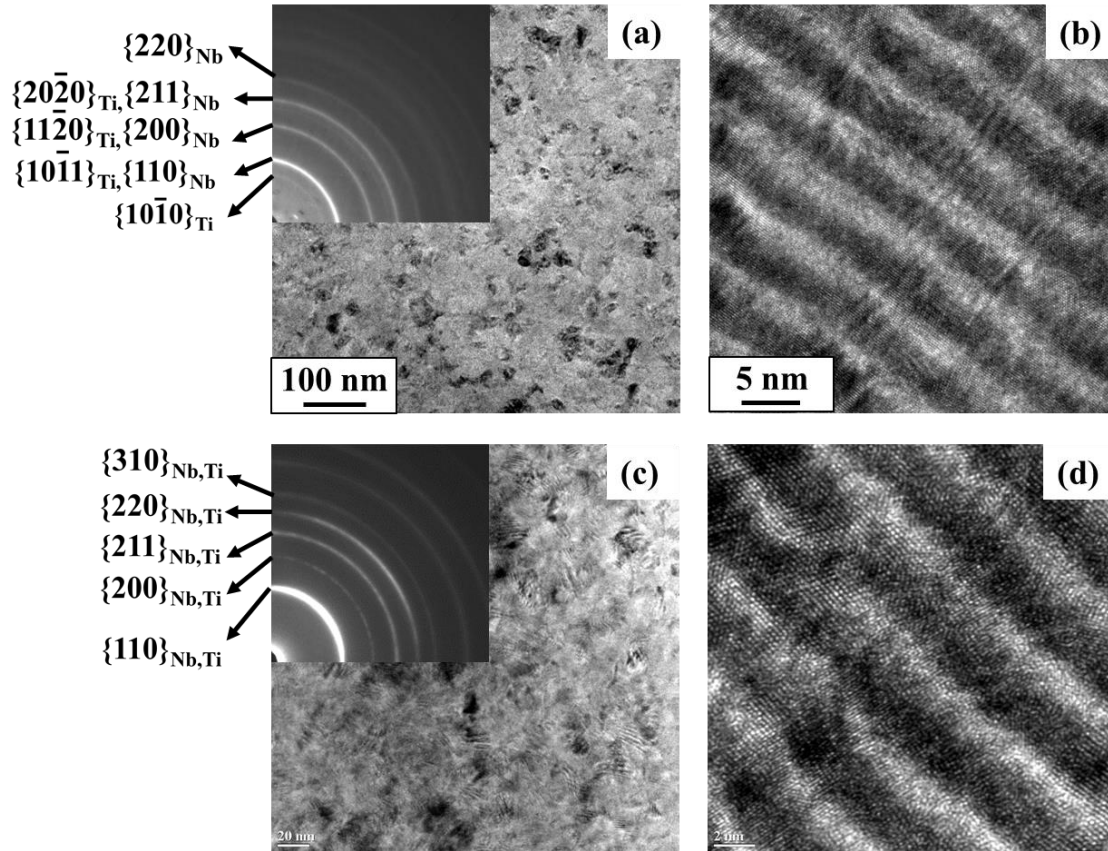


Fig. 3.4 (a) Plan-view TEM image of the 3 nm Ti/3 nm Nb multilayer. The inset is the electron diffraction pattern taken on this multilayer. Note that the distinctive hcp Ti ring has determined this multilayer to be hcp/bcc Ti/Nb. (b) Cross-section TEM image of the 3 nm/3 nm multilayer. (c) Plan-view TEM image of the 2 nm Ti/2 nm Nb multilayer. The inset is the electron diffraction pattern taken on this multilayer. The extinction of the hcp confirms the bcc/hcp phase in this multilayer. (d) Cross-section TEM image of the 2 nm/2 nm multilayer. The interface remains sharp.

One of the challenges in determining if bcc Ti is also stabilized with hcp Ti in a single layer for the 3 nm/3 nm multilayer is that β -Ti and bcc Nb have near equivalent lattice parameters resulting in overlapping reflections. Attempts at dark field imaging bcc grains in the Ti layer were also not possible. The {0002} hcp Ti d-spacing of 0.2341 nm (ICDD PDF 00-044-1294) is very near the {110} bcc Nb 0.2338 nm (ICDD PDF 00-035-0789) value. By selecting the {110} reflection for imaging, the close-packed reflection is also captured. Thus any grains that are imaged in the Ti layer could be either β -Ti or hcp Ti. Unlike the plan-view condition, where the electron beam is parallel to this closed packed hcp direction and the diffraction condition for these reflections is not satisfied; in the cross-section, the electron beam is now perpendicular to this direction and satisfies the diffraction condition and is problematic in the proposed dark field imaging scheme from bcc {110}. Similar d-spacing values for other hcp and bcc reflections had similar near close proximity issues where the smallest aperture in the TEM could not separate only bcc symmetric reflections. Consequently, any dark film imaging of grains in the Ti could not conclusively indicate bcc in the layer, as it could be either bcc or hcp. High Resolution TEM was also inconclusive because bcc and hcp share a similar ABAB stacking in the close packed direction, which these films grew [17], and have near similar d-spacings as noted above. Regardless of these experimental challenges, the agreement of the simulation for the existence of the hcp phase provides confidence in its predictive capability and support for the possibility of mixed phase layers within these types of multilayers.

3.6 Summary

In summary, a MD deposition code was used to investigate the phase stability in a Ti/Nb multilayer. The simulations were able to provide insights into the possibility of sub-growth surface

transformations within the Ti layer as a result of a second bcc Nb interface. The results revealed that Ti, in a 2 nm/2 nm configuration, was nearly completely stabilized as bcc Ti, which agreed with experiments. However, a 3 nm/3 nm configuration resulted in mixed bcc and hcp phase predictions for the Ti layer. This hcp phase was confirmed experimentally; however, conclusive determination of the bcc Ti within the Ti layer was elusive because of similar diffraction reflections between β -Ti and α -Ti. This work demonstrates how simulations can provide further insight into the stability behavior of nanoscale thin film materials, particularly when experimental methods are unable to capture the event.

3.7 Acknowledgements

This work has been supported by the National Science Foundation (Grant NSF-DMR-1207220). The author thanks the Central Analytical Facility in the University of Alabama for support.

3.8 References

- [1] Wu F, Narayan J. *Crystal Growth & Design* 2013;13:5018.
- [2] Parker C, Maria J, Kingon A. *Appl.Phys.Lett.* 2002;81:340.
- [3] Natori K, Otani D, Sano N. *Appl.Phys.Lett.* 1998;73:632.
- [4] Bavykin DV, Friedrich JM, Walsh FC. *Adv Mater* 2006;18:2807.
- [5] Zhang S, Kats MA, Cui Y, Zhou Y, Yao Y, Ramanathan S et al. *Appl.Phys.Lett.* 2014;105:211104.
- [6] Fukaya T, Tominaga J, Nakano T, Atoda N. *Appl.Phys.Lett.* 1999;75:3114.
- [7] Shen J, Kirschner J. *Surf.Sci.* 2002;500:300.
- [8] Shen J, Gai Z, Kirschner J. *Surface science reports* 2004;52:163.
- [9] Wilson, L, Bienenstock, A. 1987;103:69.
- [10] Boher P, Giron F, Houdy P, Beauvillain P, Chappert C, Veillet P. *J.Appl.Phys.* 1991;70:5507.
- [11] Vavra W, Barlett D, Elagoz S, Uher C, Clarke R. *Physical Review B* 1993;47:5500.
- [12] Dregia S, Banerjee R, Fraser H. *Scr.Mater.* 1998;39:217.
- [13] Thompson G, Banerjee R, Dregia S, Fraser H. *Acta materialia* 2003;51:5285.
- [14] Thompson G, Banerjee R, Dregia S, Miller M, Fraser H. *J.Mater.Res.* 2004;19:1582.
- [15] Li JC, Liu W, Jiang Q. *Acta Materialia* 2005;53:1067.
- [16] Hwang RQ, Bartelt MC. *Chem.Rev.* 1997;97:1063.
- [17] Wan L, Yu X, Thompson GB. *Acta Materialia* 2014;80:490.
- [18] Banerjee R, Ahuja R, Fraser HL. *Phys.Rev.Lett.* 1996;76:3778.
- [19] Plimpton S. *Journal of Computational Physics* 1995;117:1.
- [20] Daw MS, Baskes MI. *Physical Review B* 1984;29:6443.
- [21] Ward L, Agrawal A, Flores KM, Windl W. *arXiv preprint arXiv:1209.0619* 2012

[22] Zhou X, Wadley H. Surf.Sci. 1999;431:42.

[23] Raabe D, Sander B, Friák M, Ma D, Neugebauer J. Acta Materialia 2007;55:4475.

CHAPTER 4

INTERRELATIONSHIP OF *IN SITU* GROWTH STRESS EVOLUTION AND PHASE TRANSFORMATIONS IN Ti/W MULTILAYERED THIN FILMS

Submitted for Publication in Journal of Applied Physics

Interrelationship of *in situ* Growth Stress Evolution and Phase Transformations in Ti/W Multilayered Thin Films

L. Wan¹, X.X. Yu¹, and G.B. Thompson¹

¹The University of Alabama, Department of Metallurgical and Materials Engineering, Tuscaloosa, Alabama USA 35487-0202

Keywords: *in situ* stresses; phase transformation; Ti/W; multilayered thin films

4.1 Abstract

This paper addresses the *in situ* growth stress evolution and phase transformation of bcc to hcp Ti in Ti/W multilayered thin films. A series of equal layer thicknesses from 20 nm to 1 nm were deposited. The bulk phase multilayers grew with the Potter orientation relationship $\langle 11\bar{2}0 \rangle_{\alpha} // \langle 111 \rangle_{\beta} | (\bar{1}011)_{\alpha} // (011)_{\beta}$. As the bilayer thickness reduced, the overall film stress became

less compressive until the hcp to bcc Ti transformed in the 1 nm/1 nm multilayer. The pseudomorphic bcc stabilization resulted in a recovery of the compressive stress to values near that for the bulk phase stabilized 5 nm/5 nm multilayers. A discernable change in stress slope was noted for the bcc to hcp Ti transition as a function of Ti layer thickness. The stress states for each film, during film growth, is rationalized by the lattice matching of the phase with the growth surface. These results are coupled to a molecular dynamics deposition simulation which revealed good agreement with the experimentally observed transformation thickness.

4.2 Introduction

Phase transformations of materials in the nanometer regime are often serendipitously discovered [1,2,3]. Multilayered thin films are an ideal architecture to study such length scale dependent phase transformations since these materials exhibit large interfacial-to-volumetric ratios that can be readily controlled through layer thicknesses. The structural and chemical nature of the interfaces can be easily modified as well through the sequence of deposition of different contact compositions and deposition energies [4]. During deposition, these thin films experience significant stress states [5,6,7] that exceed elasticity limits for their bulk counterparts. Such stress conditions likely control and/or influence the stability of the phases formed within these films.

In general, the prediction of phase transformations in multilayered thin films has been explained using both strain induced transformation concepts [8,9] and classical thermodynamics [10,11,12,13]. In the former model, the film transforming layer achieves a metastable condition which is associated with a local minimum energy state as the lattice parameter undergoes strain. In the thermodynamic approach [10,11,12,13], the reduced layer thickness results in the interfacial

energy reduction dominating the volumetric energy penalty for the phase transformation. Hence, from a thermodynamic prospective, the change in phase is placing the system at its equilibrium condition considering the balance of the interfacial and volumetric energies. In either case, these strains result in stresses in the film which would change the stabilization energy criteria. Thompson *et al.* reported a transition from hcp to bcc Zr within a series of Zr/Nb multilayers [11] and related the transformation to coherency strains within a thermodynamic approach. Other hcp to bcc transformations have been noted for Ti in Ti/Nb multilayers [12,14]. In this system, significant Nb interdiffused into the Ti layers and chemically stabilized the transformation to larger layer thicknesses. The role of stress evolution and its interrelationship to interface intermixing and the thermodynamics of a phase transformation remain a fertile area of research.

The intrinsic stresses generated when a thin film grows will alter the thermodynamic energies of the system and provide a connection between the strain induced and thermodynamic based approaches described above. It is generally accepted that the initial compressive stress at the first stage of growth is a result of the atomic-scale migration into embryonic islands that form to minimize surface area to volumetric energies as the atoms nucleate on the substrate [15,16,17]. The subsequent tensile stress originates from the elastic strain associated with the coalescence of these islands to minimize the grain boundary energy. Upon post coalescence of the grains, the stress may retain either a tensile or compressive state depending on the mobility of the adatoms [18,19,20,21].. Elemental films with low atomic mobility, such as Fe, Cr, and Al, tend to retain the tensile condition with continued growth unless acted upon by external stimuli, such as heating the substrate. For films with atoms of higher intrinsic, such as Cu, Nb and Ti, they exhibit a return to compressive stress in the post coalescence condition. The mechanism of post-coalescence compressive stress is still under discussion [22,23,24,25]. All of these stresses can be captured by

measuring the substrate bending moments creating by the growing film using a laser reflection technique [26]. The relations of the film stress and the substrate curvature is given by the Stoney equation [27]

$$\sigma_f = \frac{E_s}{6(1-\nu_s)} \frac{t_s^2}{t_f} \left(\frac{1}{R} - \frac{1}{R_0} \right) \quad (1)$$

where σ_f is the film stress, E_s is the Young's modulus of the substrate, ν_s is the Poisson's ratio for the substrate, t_s and t_f are the thicknesses of the substrate and the film, and $1/R$ and $1/R_0$ are measured curvatures of the film before and during/after the deposition. This equation considers the force balance between the substrate and the film. By knowing the Young's modulus and Poisson's ratio of the substrate, as well as the detecting the curvature change, the biaxial stress in the film is determined.

Shull and Spaepen [28] have applied the measurements of single film stress growth to that of Ag/Cu multilayered films. These stress states were used to deduce atomic mobility [29] of each film on the other, where a tensile state is related to low adatom mobility and compressive state to higher adatom mobility. The interfacial stress of each layer was determined by comparing how the stress changed when on layer grew on the other [28]. This type of stress measurement would provide a very interesting diagnostic tool to investigate how phase transformations influence adatom mobility during growth. The authors here have recently used such *in situ* stress measurements to successfully monitor the hcp to bcc Ti transformation in Ti/Nb multilayers [14]. It was observed that Ti initially grew in a tensile condition up to ~ 2 nm where Ti transformed to hcp and the stress reverted to a compressive stress state in the Ti layer.

This research will elucidate the interrelationship of *in situ* growth stress evolution with a possible Ti phase transformation in Ti/W thin film multilayers. Unlike the prior Ti/Nb multilayers

[14] , where the bcc lattice values between β -Ti ($a=0.327$ nm, extrapolated to room temperature [14]) and bcc Nb ($a=0.330$ nm) are nearly equivalent yielding a coherent interface, the Ti/W system offers a much more strained interface of β -Ti with W ($a=0.316$ nm). Under such conditions, the stress states should be altered and provide new insights into Ti's stabilization. These results will help to explain how film growth is altered by interfacial energy reduction and strain. This will bridge our knowledge gaps between strain induced and thermodynamic driven phase transformations.

4.3 Experimental and Computational Details

4.3.1 Thin films deposition and post-growth characterization

The Ti/W multilayered thin films with equivalent individual layer thicknesses were sputter-deposited from > 99.95% pure elemental targets onto [001] Si substrates to a thickness of ~200 nm. These films had equivalent layer thicknesses which ranged from 20 nm to 1 nm or bilayers from 40 nm to 2 nm. The base vacuum pressure prior deposition was $< 10^{-8}$ Torr. For sputtering, ultra-high purity Argon was flowed as the working gas at 10 standard cubic centimeters per minute flow rate to a pressure of 2 mTorr.

The *in situ* stress evolution during the deposition was monitored using a laser reflection measurement technique with the *k*-Space Associates (kSA[®]) Muti-beam Optic Sensor (MOS). The details about this wafer curvature-based technique can be found elsewhere [26] . The deposition rates of Ti and W were determined by dividing the film thickness, measured from X-Ray Reflectivity (XRR) [30] and confirmed by the Transmission Electron Microscopy (TEM) cross-sectional micrographs, by the deposition time. XRR was performed on a X'pert Philips diffractometer operated with Cu K_{α} radiation at 40 kV and 30 mA. The growth rates of Ti and W

were 0.029 nm/s and 0.060 nm/s, respectively. X-Ray Diffraction (XRD) was conducted *ex situ* on Bruker Discovery D8 General Area Diffraction Detector Systems (GADDS) with Co K_{α} radiation operated at 40 kV and 35 mA for phase identification of the post deposited films. Selected Area Electron Diffraction (SAED) patterns were also taken from thin plan-view/cross-section foils in the FEI Tecnai F20 (S)TEM. The plan-view foils were prepared by cutting a 3 mm diameter disc from the bulk sample and SiC grinding the disc to be $< 100 \mu\text{m}$, followed by dimpling the disc in a Fischione Model 200 Grinder to a thickness of $\sim 10 \mu\text{m}$ at the bottom of the dimple. The dimpled discs were ion milled using a Gatan 691 Precision Ion Polishing System (PIPS) that utilizes Ar ions to create electron transparent perforations in the dimpled region. The diffraction pattern together with XRD results provided phase identification and preferential growth orientation results. Cross-sectional TEM foils were prepared by Focused Ion Beam (FIB) lift out technique [31] with a 5 kV clean up step to reduce any Ga^+ implantation on the foil surface using the FEI Quanta 3D dual beam FIB-SEM.

4.3.2 Simulation method

The experimental results were coupled with a Molecular Dynamic (MD) simulation to provide insights on how the lattice mismatch and elastic strain at the interfaces contributes to the final crystal structure of the thin films. The MD simulations was performed utilizing the LAMMPS code. The monatomic potentials have to be normalized to a unique state instead of being simply combined from the two potentials [32]. The binary Ti-W EAM potential was generated from a developed alloy EAM potential database [33,34] of sufficient generality with normalized elemental potentials. The in-plane directions of the model were periodic boundary conditions while the out-of-plane (growth) direction was fixed. For the W initial growth layer, $2 \times 2 \times 2$ grains were

randomly produced by the Voronoi construction [35]. Four regions were created in the model. 1) A fixed region with the atoms in the bottom 1 nm immobile to prevent the movement of the initial W layer by the incident atoms. 2) A temperature region where the incoming atoms interact with the underlayer. 3) An insertion region where the incident Ti atoms at a kinetic energy, E_k , of 1 eV were injected in a normal fashion towards the initial W layer every 1 ps. And 4) a virtual wall region was used to re-sputter the atoms reflected by the W layer with initial kinetic energy E_k to improve the simulation efficiency. It should be noted that for the deposition process, the microcanonical NVE (number, volume, energy) ensemble was first used for all the regions until the canonical NVT (number, volume, temperature) ensemble was introduced for the temperature region to solve the equations of motion for the atoms such that the system temperature was maintained at 300K. The structures were then fully relaxed for 500 ps after deposition to achieve equilibrium. OVITO software [36] was used to visualize the outputs and the results of which will be discussed in the next session.

4.4 Results and Discussions

4.4.1 Phase identification

Similar to what has been observed in the Ti/Nb metallic multilayered thin film system [14], Ti adopts a bcc structure when it grows sufficiently thin within the Ti/W stacking structure. The stabilization is determined by the XRD and electron diffraction patterns shown in **Fig. 4.1** and **Fig. 4.2**. This pseudomorphic transition is believed to be the interplay of interfacial energy reduction and strain as noted in the introduction. The XRD scans for the Ti/W multilayered thin films, **Fig. 4.1**, indicate that the as-deposited 1 nm/1 nm Ti/W multilayer adopted a highly textured, bcc phase as evident by the singular peak at $\sim 45.9^\circ$, which is in close agreement with the bcc β -Ti phase at 45.0° (ICDD 00-044-1288). All other bilayer thicknesses did not reveal this bcc Ti stabilization.

At these very fine layer thickness, a single XRD peak could also suggest the formation of a textured, intermixed alloy film, as well be shown later, this 1 nm/1 nm multilayer retained its layered morphology. Interestingly, as the bilayer thickness is reduced, W's XRD intensity peak readily decreases in comparison to Ti making its phase identification difficult. Since a limited number of diffraction peaks were obtained from the highly textured XRD scans, the complimentary plan-view TEM diffraction, with its multiple $\{hkl\}$ reflections, confirms the XRD findings.

Fig. 4.2(a) and **(b)** are representative plan-view TEM micrographs of the 20 nm/20 nm and 1 nm/1 nm multilayers respectively. The in-plane grain size for each film varies from ~20 to ~50 nm. The SAED patterns for each film is shown in **Fig. 4.2(c)** and **(d)** and confirm the stability of each phase seen in the XRD scans. In the 20 nm/20 nm Ti/W film pattern (**Fig. 4.2(c)**), a distinctive $\{10\bar{1}0\}$ hcp Ti ring is present indicating a 'bulk' Ti phase. However, in the 1 nm/1 nm multilayer, this reflection is absent and only the bcc reflections can be indexed (**Fig. 4.2(d)**). Additionally, the 1 nm/1 nm $\{110\}$ ring is broad and includes in its range a d-spacing of ~ 2.22 Å, which is in close agreement the W $\{110\}$ d-spacing of 2.23 Å assisting in W's phase identification. The TEM cross section micrographs, **Fig. 4.2(e)** and **(f)**, reveal a chemically modulated layer structure for each multilayer with relatively smooth and abrupt interfaces. In particular to **Fig. 4.2(f)**'s 1 nm/1nm multilayer, this image was acquired under a scanning TEM – High Angle Annular Dark Field (HAADF) imaging condition. Unlike a bright field image, which is sensitive to contrast changes from Bragg scattering, contour bends, and thickness fringes, the HAADF collects incoherently scattered electrons whose intensity is directly proportional to nearly the square of the atomic number, Z^2 . Because of the large difference in atomic number between Ti (22) and W (74), clear chemical imaging differences can be readily observed. Even at this very thin layer spacing,

distinct contrast from the Ti (dark contrast) and W (bright contrast) is seen suggestive that intermixing through the layers was not present and minimal at the interfaces.

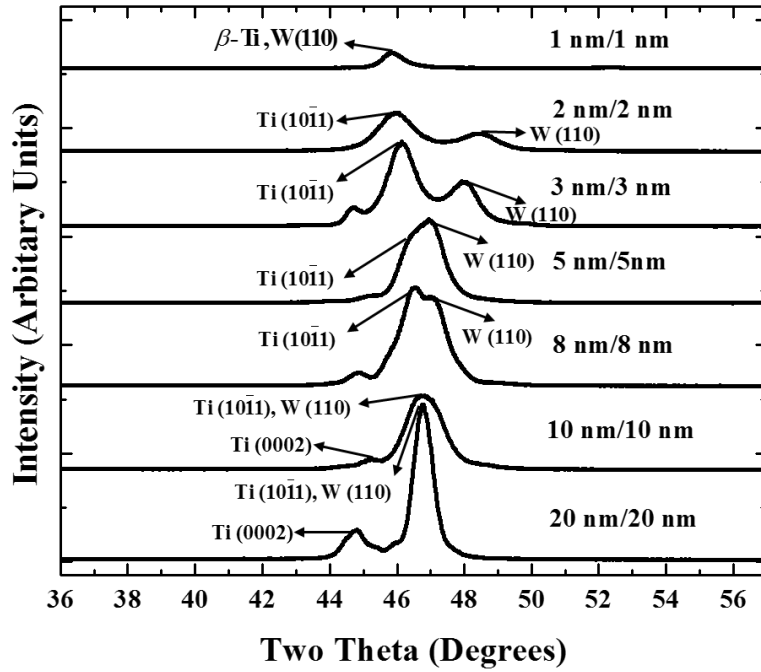


Fig. 4.1 XRD results of various multilayers listed by their bilayer thicknesses.

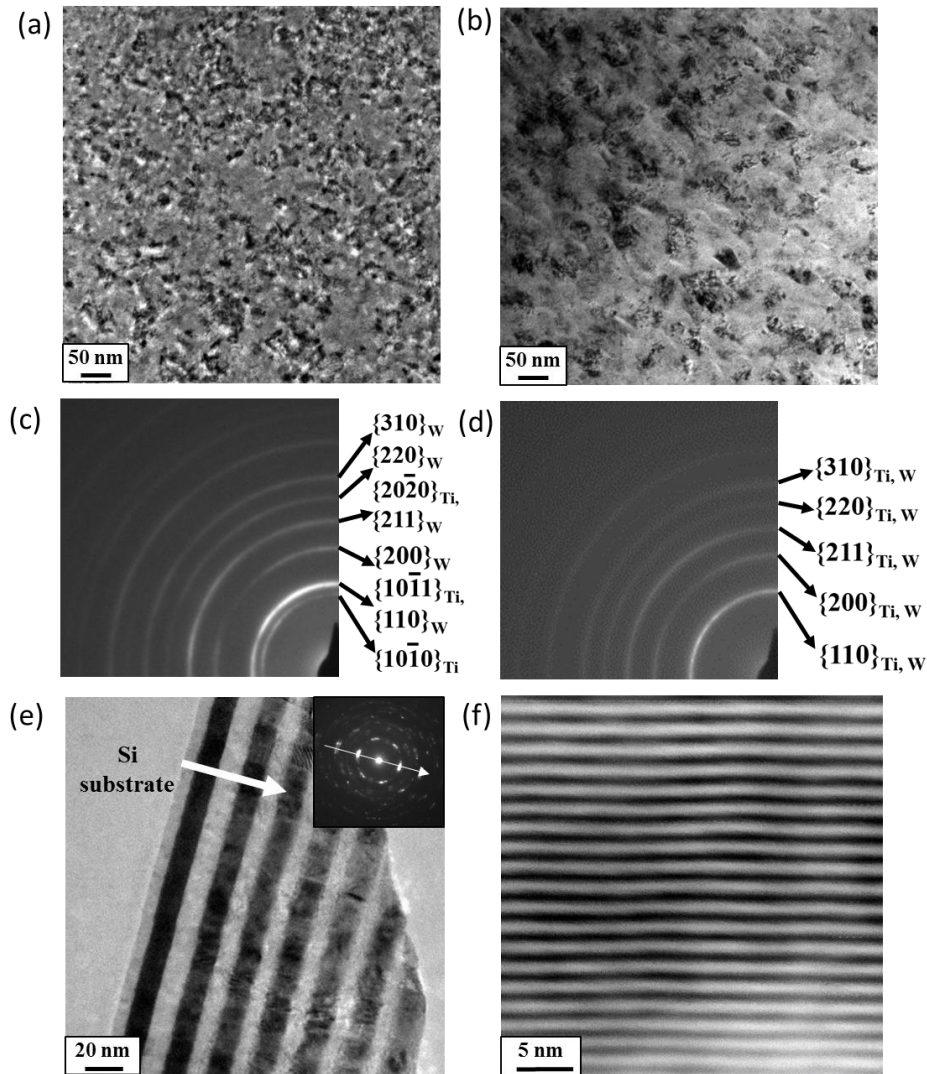


Fig. 4.2 (a) Plan-view TEM image of 20 nm/20 nm Ti/W multilayer. (b) Plan-view TEM image of 1 nm/1 nm Ti/W multilayer. (c) SAED pattern of 20 nm/20 nm, 10 nm/10 nm, 8 nm/8 nm, 5 nm/5 nm, 3 nm/3 nm, 2 nm/2 nm Ti/W multilayer. (d) SAED pattern of 1 nm/1 nm Ti/W multilayer. (e) Cross-section TEM image of 10 nm/10 nm Ti/W multilayer with an inset of SAED pattern. The white arrow shows the film exhibits a texture along the layer modulation direction. (f) STEM-HAADF image of 1 nm/1 nm Ti/W multilayer. The bright contrast corresponds to the W layer with the dark contrast being the Ti layer.

A closer investigation of the XRD results, **Fig. 4.1**, allows one to glean how this transformation proceeds. For all the hcp Ti/bcc W films, i.e., 20 nm/20 nm, 10 nm/10 nm, 8 nm/8 nm, 5 nm/5 nm, 3 nm/3 nm, and 2 nm/2 nm, the most intense peaks are indexed as Ti ($10\bar{1}1$) (47.0° , d-spacing 2.243 Å, ICDD 00-044-1294) and W (110) (47.1° , d-spacing 2.238 Å, ICDD 00-004-0806). For the 20 nm/ 20 nm multilayer, these Ti and W peaks overlap ($< 0.2\%$ d-spacing difference) due to each phase being relatively in a strain-free condition. However, with the reduction of the bilayer thickness, it is clearly observed that these two peaks tend to deviate from their ‘strain free’ designated two theta angles. This peak split is attributed to the strain in each layer as its volume (thickness) being reduced. Note that the XRD measurements display the out-of-plane reflection [37], with the Ti ($10\bar{1}1$) peak shifting to a higher d-spacing (tensile) indicating an interplanar stretching along the growth direction with a complimentary shift for the W (110) peak to a lower d-spacing (compression) along the out-of-plane direction. This type of lattice parameter shift was not observed in the Ti/Nb multilayers [12].

Fig. 4.2(e) and **4.2(f)** are representative cross-sectional TEM micrographs of the 10 nm/10 nm and 1 nm/1 nm Ti/W multilayers. An inset of SAED pattern shows the 10 nm/10 nm film exhibit a ($10\bar{1}1$)Ti//(110)W texture along the layer modulation direction, as highlighted by the white arrow in **Fig. 4.2(e)**, and is in agreement with the XRD scans. Recall the orientation relationship of α -hcp/ β -bcc Ti has been reported to be either the Burgers $\langle 11\bar{2}0 \rangle_\alpha // \langle 111 \rangle_\beta | (0001)_\alpha // (011)_\beta$ [38] or Potter $\langle 11\bar{2}0 \rangle_\alpha // \langle 111 \rangle_\beta | (\bar{1}011)_\alpha // (011)_\beta$ [39]. The direction of $(\bar{1}011)_\alpha // (011)_\beta$ are perpendicular to the interface, and parallel to the film growth direction. Based on the XRD texture and TEM diffraction results, the hcp Ti/bcc W interface exhibits the Potter orientation relationship in Ti/W, as the direction of $(10\bar{1}1)$ Ti and (110) W planes parallel to the film growth

direction, i.e, interface normal. In contrast, Ti/Nb revealed a Burgers orientation [11]. Hence, the bcc W template surface appears to alter the growth texture of Ti from its (0001) low energy close packed surface to one, ($\bar{1}011$), that appears to accommodate the interface chemical and/or structural matching better. Considering the Potter orientation relationship, a 7% misfit strain can be calculated. This significant strain might lead to the in-plane shrinkage of the Ti lattice and enlarge the W lattice, which is consistent with the observed peak shifts in the XRD scans.

4.4.2 *In situ* stress evolution

The *in situ* stress evolution for the Ti/W multilayers are presented in **Fig. 4.3(a)**. The stress-thickness product for all the films are plotted as a function of film thickness. The observations are as follows: First, all the multilayers exhibit an overall compressive stresses in the post-coalescence regime [23], which is consistent with the prior Ti/Nb behavior [14]. Second, with a decreasing bilayer thickness, the overall stress becomes less compressive at an equivalent overall thickness among all hcp/bcc Ti/W multilayers. In contrast, Ti/Nb multilayers became even more compressive with decreasing bilayer thickness [14]. Third, both the Ti and W layers in each multilayer have a compressive stress-thickness product slope. Of these two elements, W's compressive slope is much steeper than its Ti counterpart. And finally, for the 1 nm/1 nm multilayer, which adopted a single bcc phase, the compressive stress was recovered to values near that of the 5 nm/5 nm multilayer, e.g. this multilayer exhibited a much more compressive overall stress-thickness compression product than either the 3 nm/3 nm or 2 nm/2 nm multilayers.

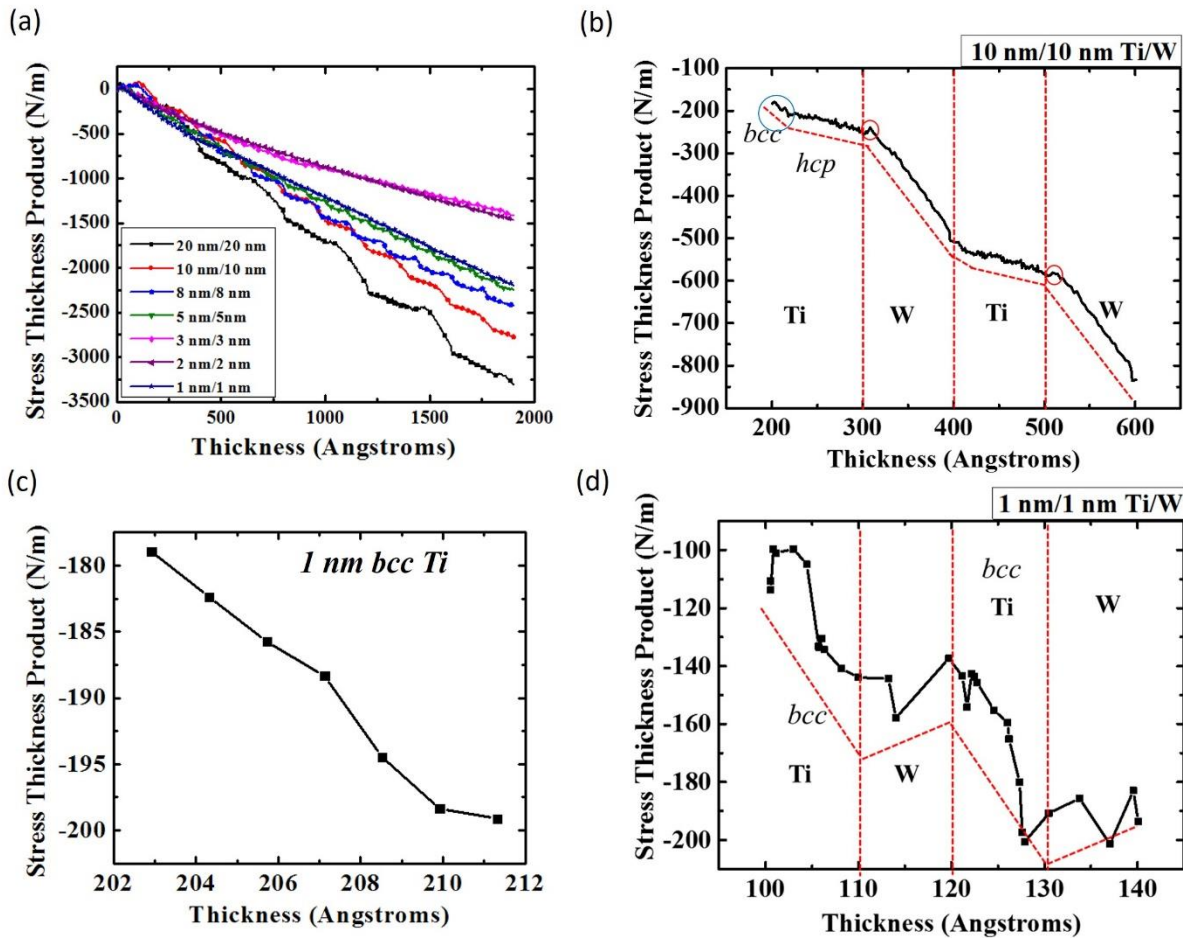


Fig. 4.3 (a) Stress evolution of the stress-thickness product versus thickness for various multilayer listed by their bilayer thickness. (b) Magnified stress-thickness product plot of the 10 nm/10 nm Ti/W multilayer. The inset reveals the large compressive stress slope for the first 1 nm of Ti growth. (c) The large compressive stress slope of the first 1 nm of Ti growth seen in **Fig. 4.3(a)**. (d) Magnified stress-thickness product plot of the 1 nm/1 nm Ti/W multilayer. Color available online.

Table 4.1. Interfacial stress values for various multilayers listed by their bilayer thicknesses

Number	Bilayer thickness (nm)	Interfacial stress (N/m)			Average interfacial stress (N/m)
		$\Delta_{\text{Ti on W}}$ (< 1 nm)	$\Delta_{\text{Ti on W}}$ (> 1 nm)	$\Delta_{\text{W on Ti}}$	
1	20	-1.75	-0.4	-19.03	-9.78
2	16	-1.64	-16.39	7.09	-3.73
3	10	-1.27	-8.93	2.48	-2.28
4	4	0.24	3.98	-3.5	-0.65

The decrease of compressive stress slope with decreasing bilayer thickness among the hcp/bcc Ti/W multilayers is rationalized by a reduction of compressive interfacial stress, as tabulated in **Table 4.1**. The measurement of interfacial stress was found by extrapolating the slope of the stress-thickness product data to zero thickness of the new layer and determining the difference between the absolute stress-thickness product value at the end of the old layer and that of the extrapolation back to zero thickness of the new layer [28]. The equation for interfacial stress measurement is shown below:

$$\Delta_{\text{avg}} = [(2 \cdot \Delta_{\text{Ti on W}} (< 1 \text{ nm}) + (t_{\text{Ti}} - 1) \cdot \Delta_{\text{Ti on W}} (> 1 \text{ nm}) + (\lambda - t_{\text{Ti}}) \cdot \Delta_{\text{W on Ti}})] / \lambda \quad (2)$$

where t_{Ti} is the individual thickness of the Ti layer (nm) and λ is the bilayer thickness or $t_{\text{Ti}} + t_{\text{W}}$, $\Delta_{\text{Ti on W}}$ or when $\Delta_{\text{Ti on W}}$ in the respective thickness range.

In **Table 4.1** the interfacial stress is divided into two thickness regions, $\Delta_{\text{Ti on W}} (< 1 \text{ nm})$ and $\Delta_{\text{Ti on W}} (> 1 \text{ nm})$, for the Ti growth based on the observed slope transition. The average interfacial stress for the bilayer was computed by weighting each interfacial value by its thickness. It can be observed that all multilayers studied in **Table 4.1** have negative interfacial stress values (compressive interfacial stresses). The increasing interfacial stress value with bilayer thickness appears to help drive the overall compressive behavior observed in these multilayers. It should be mentioned that the reported values are experimental measurements. As noted by Clemens *et al.* [40], interfacial intermixing can change the interfacial stress. In that work, the predicted calculations of the interfacial stress were altered by the extent of interface intermixing. Our equations described above are fitted to experimental measurements which accommodate whatever level of intermixing may or may not be present in the multilayer. **Fig. 4.2(f)**'s STEM-HAADF image suggests minimal intermixing between the layers and will be further discussed in relationship to a MD simulation

that predicted the phase transformation with no assumed intermixing. The interfacial stress findings, coupled to the XRD data of **Fig. 4.1**, suggests that each layer undergoes some amount of strain accommodation, i.e. peak splitting, for the hcp Ti/bcc W layers. Consequently the overall films were able to reduce their intrinsic compressive stress state with decreasing bilayer spacing. However, when the Ti layer undergoes an hcp to bcc transition, the compressive stress of the collective film increases indicating that the pseudomorphic stabilized phase is under a higher compressive stress state.

Fig. 4.3(b) and **(d)** are representative magnified stress-thickness product plots of 10 nm/10 nm and 1 nm/1 nm multilayers, respectively. In these images, one can understand how the stress is evolving at each thickness as it grows and infer how structural stability may influence the measured values. For the films at 10 nm/10 nm thickness, the growth stress for the first 1 nm of Ti exhibits a large compressive behavior (steeper slope). Upon growing to thicknesses greater than ~ 1 nm, the Ti growth stress was slightly less compressive (gradual slope). A magnified image of the first 1 nm Ti stress behavior is plotted in **Fig. 4.3(c)**. Based on the 1 nm stabilization of bcc Ti in the 1 nm/1 nm Ti/W multilayer, this change of slope indicates the phase change [14].

For the bcc Ti on W, with an orientation relationship of $(011)_{\beta} // (011)_{\text{bcc}} \mid \langle 111 \rangle_{\beta} // \langle 111 \rangle_{\text{bcc}}$, the coherency strain would be the following:

$$\varepsilon = \frac{d_{(011)_{\text{Ti}}} - d_{(011)_{\text{W}}}}{d_{(011)}} = \frac{a_{\text{Ti}} - a_{\text{W}}}{a_{\text{Ti}}} = \frac{3.27 - 3.16}{3.27} \approx 3\% \quad (3)$$

As the 1 nm bcc Ti grows on the W surface, such a misfit strain could result in a reduction of the interfacial energy by the removal of misfit dislocations. This would then contribute favorably towards a reduction in the interfacial energy contribution towards stabilization [11],

albeit at the expense of volumetric strain energy increases. It is note-worthy that the *in situ* stress reflects the in-plane strain information. Since the stress shows a negative slope, which indicates a compressive nature, this would be in agreement that β -Ti would undergo in-plane compression to match W as given above in equation (3).

When the W layer grows on the hcp Ti surface, a small region (< 1 nm) of modest positive slope is noted in the stress response. This suggests an initial tensile growth condition as a very thin layer of W lattice matches to the Ti surface. This is shown by the circle in **Fig. 4.3(b)** in the W film region. Once the W film coalesces over the Ti surface, the W film reveals a much more compressive stress behavior than either the bcc or hcp Ti states. Though the mechanism of compressive stress in the post-coalescence regime is still under investigation, it is widely accepted that this stress behavior can be related to the grain boundary mobility of the adatoms which segregates into the grain boundary and facilitate compression in the grains [18,19,21]. The variation in data points within an individual layer shown in **Fig. 4.3(d)** is attributed to experimental noise, i.e. instrument vibration, data collection delay, etc.

4.4.3 Atomistic simulation of phase transformation

To add further insights to the experimental results, MD simulations of Ti deposited onto a polycrystalline W substrate was performed and are presented in **Fig. 4.4**. The corresponding atoms are colored by either element type or crystal structure using the common neighbor analysis (CNA). **Fig. 4.4(a)**, **(c)** and **(e)** are colored by element allowing for easier visualization of the W substrate and the Ti layer, whereas **Fig. 4.4(b)**, **(d)** and **(f)** are colored by structure type using the CNA method. **Fig. 4.4(h)** is a schematic that represents the various regions and boundary conditions in the simulation as described in the modeling details found in Section II. At layer thicknesses at or less than 0.5 nm, the Ti revealed a bcc structure as shown in **Fig. 4.4(b)**. As the thickness continued

to thicken, the onset of hcp coordination initiated, evident by the very small volumes of destabilized regions of hcp Ti in the 1 nm layer, **Fig. 4.4(c)** and **(d)**. Finally, at 2 nm of thickness, **Fig. 4.4(e)** and **(f)**, the Ti layer is largely hcp. This is quantitatively captured on the hcp coordinated atom number plot versus thickness, **Fig. 4.4(g)**, which shows the increasing hcp coordination configuration with increasing Ti film thickness.

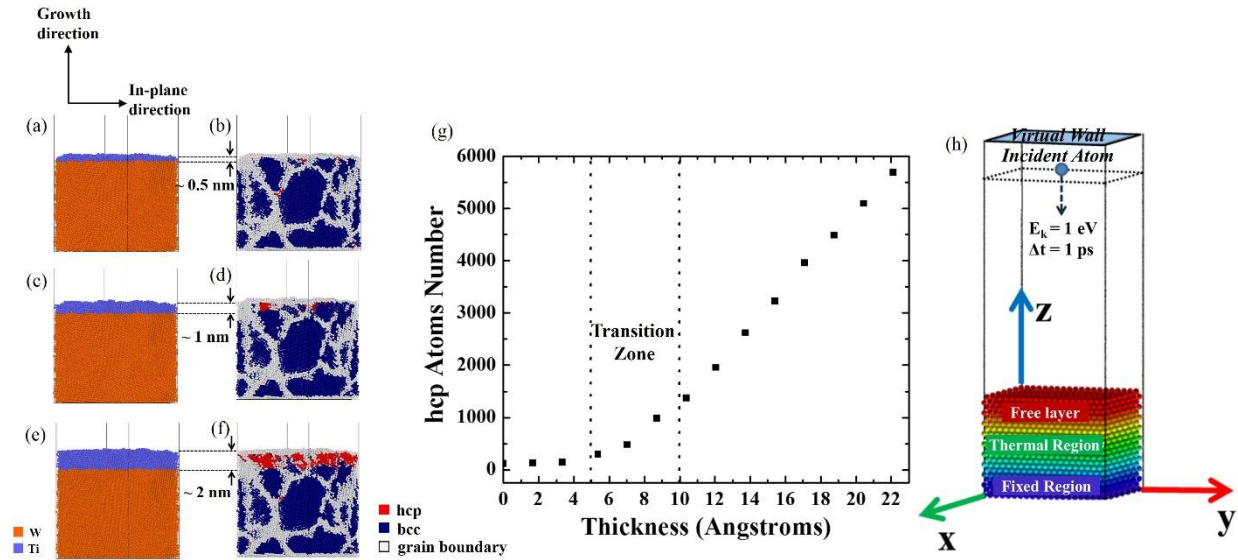


Fig. 4.4: The two sets of colors represent the atom types – Ti designation being purple and W designation being orange. The dark blue color represents the bcc atom coordination, red being the hcp atom coordination, and the gray being atoms with no long range coordinated structure, i.e. atoms at grain boundaries and surfaces (a) 0.5 nm of Ti on a W substrate. (b) 0.5 nm of bcc Ti grown on a bcc W. (c) 1 nm of Ti on W substrate. (d) 1 nm of bcc Ti grown on bcc W. (e) 2 nm of Ti on W substrate. (f) 2 nm of hcp Ti grown on bcc W. (g) Number of hcp coordinated atoms versus film thickness. (h) Schematic of simulation regions. Color available on line.

The simulation does suggest a transition zone to the hcp phase initiating near 0.6 nm and completing near 1 nm of thickness, **Fig. 4.4(g)**. One reason the experimental results may not show any hcp diffraction for the 1nm/1nm film could be either (1) a low volume fraction of the hcp phase was present but insufficient for the measurable diffracted intensities and/or (2) some amount of W intermixing with Ti during the deposition process which helped to stabilize the β -Ti phase. One could also argue that the top bcc W surface could be stabilizing the bcc Ti phase as well, since two bcc interfaces are now in contact with the Ti layer and contribute to the thermodynamic stabilization concepts proposed by Dregia *et al.* [10]. However, the *in situ* stress reveals no discontinuity in the slope over the continuous bcc Ti growth thickness suggesting that bcc Ti is continuously stabilized up to 1 nm without this top W surface.

As observed in other systems [14], intermixing can play an important role in stabilizing a pseudomorphic phase. However, the STEM-HAADF image in **Fig. 4.2(f)** revealed a reasonably pronounced layered morphology, even at the thinnest layers studied. The minimal intermixing between the layers could be attributed to several factors. The low homologous deposition temperature and low temperature solubility between the two species would not necessarily favor substantial mixing either kinetically or thermodynamically. In addition, the surface energy and crystallographic symmetry may not favor ease for mixing either. Zhou *et al.* [41] proposed and verified a sputter deposition mechanism where surface adatoms exchange with subsurface atomic layers to enrich the growth surface with the lowest surface energy species. Such behavior led to growth dependent intermixing. Mezey *et al.* [42] reported that the surface energy ratio of γ_W / γ_{Ti} to be 1.4. Hence, it would be unlikely that incoming Ti adatoms would exchange with the prior W deposited subsurface layer since the lower surface energy species (Ti) is already present on the surface. Additionally, when Ti grows on a W surface, it experiences a compressive stress which

would further hinder W's incorporation into the Ti layer. Based on these surface energy arguments, when W is grown on a Ti surface, W would preferentially exchange with Ti to reduce its surface energy. However, hcp Ti has limited solubility for bcc W at room temperature, as indicated by the binary phase diagram [43]. Likewise W is a larger atom than Ti (146 pm vs. 136 pm, respectively [44]) which would provide an additional mechanical strain for lattice incorporation. As a final point, from the binary phase diagram [43], a miscibility gap exists under $\sim 1250^{\circ}\text{C}$ for the two bcc phases. This suggests that even when the two phases are the same symmetry, neither species has a strong tendency to mix. Thus, for either case of one layer growing on the other, minimal intermixing could be expected and has been verified by the aforementioned cross-section micrographs in **Fig. 4.2**. Attempts to perform atom probe tomography to further quantify the extent of atomic intermixing was undertaken. Unlike the prior report by the authors for Ti/Nb [14], these multilayers did not successfully field evaporate. The specimens continually fractured under voltage and laser pulsing which is attributed to the very large evaporation field differences between Ti and W [45].

4.5 Conclusions

A series of Ti/W multilayered thin films with varying bilayer thicknesses have been sputter-deposited onto [001] Si substrates which had a native surface oxide. As the bilayer thickness was reduced from 40 nm to 4 nm, the overall compressive stress reduced. Upon stabilizing bcc Ti for the 2 nm bilayer film (1 nm/1 nm), the compressive stress increased again to values commensurate with the 5 nm/5 nm bulk phase multilayer. This change in stress is attributed to the compressive stress state of the stabilized bcc/bcc phases. The growth of bcc Ti onto the W surface showed a steep compressive slope whose gradient decreased, but was still compressive,

when compared to hcp Ti's growth. This discernable change in stress slope denoted the bcc to hcp Ti transition as a function of Ti layer thickness. Cross-sectional transmission electron microscopy micrographs confirmed the layered morphologies even at the thinnest layers studied. The stress states for each film, during film growth, was rationalized by the lattice matching of the phase with the growth surface. The lattice strain and the reduction of interfacial energy are two key factors to drive the bcc to hcp Ti phase transformation in the Ti/W multilayers. These results were coupled to a molecular dynamics deposition simulation which revealed good agreement with the experimentally observed transformation thickness.

4.6 Acknowledgements

The authors gratefully recognize the National Science Foundation, DMR-1207220 and the Central Analytical Facility in the University of Alabama for support.

4.7 References

- [1] Hoogeveen R, Moske M, Geisler H, Samwer K. *Thin Solid Films* 1996;275:203.
- [2] Boher P, Giron F, Houdy P, Beauvillain P, Chappert C, Veillet P. *J.Appl.Phys.* 1991;70:5507.
- [3] Vavra W, Barlett D, Elagoz S, Uher C, Clarke R. *Physical Review B* 1993;47:5500.
- [4] Hwang RQ, Bartelt MC. *Chem.Rev.* 1997;97:1063.
- [5] Koch R. *Journal of Physics: Condensed Matter* 1994;6:9519.
- [6] Miyamura A, Kaneda K, Sato Y, Shigesato Y. *Thin Solid Films* 2008;516:4603.

- [7] Chuang C, Chao C, Chang R, Chu K. *J.Mater.Process.Technol.* 2008;201:770.
- [8] Bruinsma R, Zangwill A. *Journal de physique* 1986;47:2055.
- [9] Bruinsma R, Zangwill A. *EPL (Europhysics Letters)* 1987;4:729.
- [10] Dregia S, Banerjee R, Fraser H. *Scr.Mater.* 1998;39:217.
- [11] Thompson G, Banerjee R, Dregia S, Fraser H. *Acta materialia* 2003;51:5285.
- [12] Thompson G, Banerjee R, Dregia S, Miller M, Fraser H. *J.Mater.Res.* 2004;19:1582.
- [13] Li J, Liu W, Jiang Q. *Acta materialia* 2005;53:1067.
- [14] Wan L, Yu X, Thompson GB. *Acta Materialia* 2014;80:490.
- [15] Cammarata R, Trimble T, Srolovitz D. *J.Mater.Res.* 2000;15:2468.
- [16] Spaepen F. *Acta Materialia* 2000;48:31.
- [17] Friesen C, Thompson C. *Phys.Rev.Lett.* 2002;89:126103.
- [18] Freund L, Chason E. *J.Appl.Phys.* 2001;89:4866.
- [19] Tello JS, Bower AF, Chason E, Sheldon BW. *Phys.Rev.Lett.* 2007;98:216104.
- [20] Chason E, Sheldon B, Freund L, Floro J, Hearne S. *Phys.Rev.Lett.* 2002;88:156103.
- [21] Floro JA, Chason E, Cammarata RC, Srolovitz DJ. *MRS Bull* 2002;27:19.
- [22] Abadias G, Fillon A, Colin JJ, Michel A, Jaouen C. *Vacuum* 2014;100:36.

- [23] González-González A, Polop C, Vasco E. Phys.Rev.Lett. 2013;110:056101.
- [24] Pao C, Foiles SM, Webb III EB, Srolovitz DJ, Floro JA. Phys.Rev.Lett. 2007;99:36102.
- [25] Shin JW, Chason E. Phys.Rev.Lett. 2009;103:056102.
- [26] Taylor C, Barlett D, Chason E, Floro J. The Industrial Physicist 1998;4
- [27] Stoney GG. Proceedings of the Royal Society of London.Series A, Containing Papers of a Mathematical and Physical Character 1909:172.
- [28] Shull AL, Spaepen F. J.Appl.Phys. 1996;80:6243.
- [29] Cammarata R, Trimble T, Srolovitz D. J.Mater.Res. 2000;15:2468.
- [30] Sasanuma Y, Uchida M, Okada K, Yamamoto K, Kitano Y, Ishitani A. Thin Solid Films 1991;203:113.
- [31] Giannuzzi L, Stevie F. Micron 1999;30:197.
- [32] Johnson R. Physical Review B 1989;39:12554.
- [33] Wadley HNG, Zhou X, Johnson RA, Neurock M. Progress in Materials Science 2001;46:329.
- [34] Zhou X, Wadley H, Johnson RA, Larson D, Tabat N, Cerezo A et al. Acta materialia 2001;49:4005.
- [35] Li J. Modell Simul Mater Sci Eng 2003;11:173.
- [36] Stukowski A. Modell Simul Mater Sci Eng 2010;18:015012.
- [37] Kline RJ, McGehee MD, Toney MF. Nature Materials 2006;5:222.
- [38] Burgers WG. Physica 1934;1:561.
- [39] Potter DI. Journal of the Less Common Metals 1973;31:299.

[40] Clemens B, Nix W, Ramaswamy V. *J.Appl.Phys.* 2000;87:2816.

[41] Zhou XW, Wadley HNG, Johnson RA, Larson DJ, Tabat N, Cerezo A et al. *Acta Materialia* 2001;49:4005.

[42] Mezey L, Giber J. *Jpn.J.Appl.Phys* 1982;21:1569.

[43] Murray J. *Bulletin of Alloy Phase Diagrams* 1981;2:192.

[44] Huheey JE, Keiter EA, Keiter RL. Harper and Row, New York 1983

[45] Miller MK, & Forbes RG. *Atom-Probe Tomography: The Local Electrode Atom Probe.* Springer, 2014.

CHAPTER 5

BCC STABILIZATION AND GROWTH STRESSES BEHAVIOR IN Ti/V MULTILAYERS

To be submitted for publication

BCC Stabilization and Growth Stresses Behavior in Ti/V Multilayers

Li Wan¹, Gregory Thompson¹

¹The University of Alabama, Department of Metallurgical Engineering, Tuscaloosa, AL 35487

Keywords: in situ growth stress; phase transformation; Ti/V; multilayered thin films

5.1 Abstract

As the length scale decreases, materials can undergo size-dependent phase changes. This work explores the hcp to bcc Ti transformations in Ti/V multilayers of equal volume fraction. A series of Ti/V multilayers were sputter-deposited and revealed a transition at ~ 1 nm Ti. This length scale stability is explained through a series of *in situ* growth stress measurements that are correlated to the epitaxial orientation of the Ti and V growth directions with respect to each other within the multilayer. It was found the hcp Ti undergoes in-plane compression while bcc V undergoes in-plane tension. It is believed that the interplay of large misfit strain and the surface energy driven intermixing, quantified by atom probe tomography, contributes to the stabilization of bcc Ti.

5.2 Introduction

When materials sizes are reduced in size, the crystal structure can change. This has been an area of active investigation for various thin films and multilayered thin film structures [1-3]. Such length scale dependent phase transformations can enable exceptional material properties for new devices with tailored functionality [4-6]. Since the interfacial-to-volumetric ratios of these types of material can be quite large, the structural and chemical nature of the interfaces is paramount. These surfaces can be modified through the sequence of deposition of different contact compositions and deposition energies [7]. In addition, these thin films can experience significant stress states during the growth that exceed elasticity limits for their bulk counterparts [8-10]. The interconnection of phase equilibrium, intrinsic growth stresses, and the stability of an interfacial compositional gradient in thin films is a fertile area of research.

Two general approaches have been used to model phase stability in thin films. The coherency model developed by Bruinsma and Zangwill [11,12] describes pseudomorphism as local minima in the free energy density function. As the film thickness is reduced, epitaxial strains created by the film matching a substrate raises the energy of the crystal; however, a crystallographic transformation to a new phase can lower the energy to this local minima and provide a metastable condition for the film. This model was explicitly developed for a thin film on a rigid substrate (single interface) in which a single transformation occurs. A series of stability maps for this transformation were then proposed based upon the strain.

Unlike a single film in contact with one interface, in a multilayered structure, the film is in contact with two interfaces – one below and above the film – and these growth surfaces may not necessarily be rigid. Furthermore, having more than one film within the stack provides opportunities for multiple transformations in the different layers that can affect the phase stability

behavior. Dregia *et al.* [13-16] proposed a classical thermodynamic model to explain these phase transformations in a two species multilayer stack. Here the competition between volumetric and interfacial energy was used to describe phase stability in a repeating bilayer. As one or both layers were reduced in thickness (or equivalently volume for a fixed surface area), the interfacial energy reduction for a phase change between the different layers becomes comparable or even larger than that of the bulk free energy penalty for such a transformation. Thus, for sufficiently thin layers, the interfacial energy reduction can thermodynamically drive a change in phase. Using this thermodynamic model, Thompson *et al.* reported a series of transitions from hexagonal close packed (hcp) to body centered cubic (bcc) Zr within a series of Zr/Nb multilayers [14]. In this paper, the influence of coherency strains on the volumetric energy was also considered and characterized as the Zr layer transformed. In this manner, the prior strain concepts proposed by Bruinsma and Zangwill [11,12] with the thermodynamic model proposed by Dregia *et al.* [13] were experimentally merged.

Other hcp to bcc transformations have also been reported using the thermodynamic approach. In Ti/Nb multilayers, the hcp-to-bcc Ti transformation was also found. Interestingly, the bcc transformed Ti layer revealed a significant amount of Nb interdiffusion into the Ti layer which provided an additional chemical stabilizing effect on the transformation layer thickness [15,17]. The most recent investigation of Ti/Nb stability using *in situ* stress measurements noted a change in tensile-to-compressive stress at the bcc-to-hcp transition [17]. The use of such real-time measurements, particularly the stress evolution of a thin film, provides insights into the relationship of how phase stability influences adatom mobility during film growth.

It is generally accepted that the initial compressive stress at the first stage of film growth originates from the adatoms forming embryonic islands [18,19]. The subsequent tensile stress is

generated from the coalescence of these islands to minimize the grain boundary energy. Elemental films with low atomic mobility tend to retain this tensile condition while adatoms with higher intrinsic mobility exhibit a return to compressive stress in the post coalescence condition, though the exact mechanism of post-coalescence compressive stress is still a matter of much discussion [20-23]. One area that has not been extensively explored in the use of *in situ* stress evolution has been its relationship to the phase stability of the film itself. As described by the prior stability models, strain (hence stress) is intimately related to phase stability as well as the thermodynamic energies for determining phase stability. Monitoring intrinsic growth stresses in real time can provide for a deeper understanding in the connection between the strain-induced and thermodynamic based phase stability concepts. Though Shull and Spaepen [24] have reported one of the earliest uses of *in situ* measurements from a multilayered film, the paper focused on the growth of Ag/Cu. Both of these films are face centered cubic (fcc) and a transformation would not necessarily be expected. To the authors' knowledge, the use *in situ* stress evolution and its connection with phase stability has only been explicitly reported in Ti/Nb [17].

This research aims on furthering the investigations of *in situ* stress behavior and its relationship to phase stability. In this paper, we explore the growth stresses for the allotropic hcp-to-bcc Ti phase transformation in Ti/V multilayers. Unlike the prior Ti/Nb investigation [17], where β -Ti, the high temperature allotrope bcc Ti phase, has near equivalent lattice spacing to bcc Nb (0.330 nm), this new bcc V template offers a considerable difference in lattice matching. The β -Ti lattice parameter is ~ 0.327 nm, extrapolated to room temperature [17], where bcc V is ~ 0.303 nm, which would generate considerably more strain at the interface and influence the adatom mobility behavior that is manifested in the stress measurements. Under such conditions, the growth stress states should be altered and provide new insights into Ti's stabilization from which

a better understanding between by interfacial energy reduction and strain can be developed. This comparative study to the former work will bridge our knowledge gaps between strain induced and thermodynamic driven phase transformations.

5.3 Experimental Details

The Ti/V multilayered thin films with equivalent individual layer thicknesses were sputter-deposited at ambient temperature (~ 25 °C) from $> 99.95\%$ pure elemental targets onto [001] Si substrates to a thickness of ~ 200 nm. The bilayer thickness (sum of the individual layer thickness) ranged from 40 nm to 2 nm. i.e. 20 nm/20 nm, 10 nm/10 nm, 5 nm/5 nm, 2 nm/2 nm, 1 nm/1 nm. The base vacuum pressure prior deposition was $< 10^{-8}$ Torr. For sputtering, ultra-high purity Argon was flowed as the working gas at 10 standard cubic centimeters per minute flow rate to a pressure of 2 mTorr.

During the deposition of the thin films, the *in situ* stress evolution was monitored using *k*-Space Associates (kSA[®]) Muti-beam Optic Sensor (MOS). The MOS system works by measuring the wafer curvature with real-time feedback. 2D laser spot arrays are reflected off the sample surface and as the wafer bends (or curves) in response to the growth stresses, the spot positions change. Using this in-plane displacement, the wafer curvature is measured and the stress determined by the classic Stoney equation given below [25]:

$$\sigma_f \cdot t_f = \frac{E_s t_s^2}{6(1-\nu_s)} \left(\frac{1}{R} - \frac{1}{R_0} \right) \quad (2)$$

where $\sigma_f \cdot t_f$ (also known as stress-thickness product) is the surface stress [26] for the film growth, E_s and ν_s are the Young's modulus and the Poisson ratio of the substrate, respectively, t_s is the thickness of the substrate, $1/R$ and $1/R_0$ are measured curvatures after and before the deposition. Further experimental details can be found in reference [17].

The deposition rates of Ti and V were determined by dividing the film thickness, measured from X-Ray Reflectivity (XRR) [27] and confirmed by the Transmission Electron Microscopy (TEM) cross-sectional micrographs, by the deposition time. XRR was performed on an X'pert Philips diffractometer operated with Cu K α radiation ($\lambda = 1.5406 \text{ \AA}$) at 40 kV and 30 mA. The growth rates of Ti and V were 0.029 nm/s and 0.031 nm/s, respectively.

A series of θ -2 θ scans of X-Ray Diffraction (XRD) was conducted *ex situ* on the same Philips diffractometer using the same operating settings. These scans provided for phase identification of the post deposited films. Selected area electron diffraction patterns (SAED) were also taken from thin plan-view and cross-sectional foils in the FEI Tecnai F20 (S)TEM to further examine the phase constitutions of each film. The plan-view foils were prepared by conventional TEM sample preparation method through cutting, polishing, dimpling and ion milling. The foil was a 3 mm disc with a small hole in the middle where electron transparent perforations were around the hole. These collected diffraction patterns, together with XRD results, provided phase identification and preferential growth orientation of the films. Cross-sectional TEM foils were prepared by Focused Ion Beam (FIB) lift out technique [28] followed by a 5 kV clean up step to reduce any Ga⁺ implantation on the foil surface using the FEI Quanta 3D dual beam FIB-SEM. Bright Field (BF) images were taken to reveal the layered structure of the multilayers. Fast Fourier Transformation (FFT) was generated on the high resolution TEM BF images to examine the orientation relationship between the two adjacent layers.

The multilayers were also characterized by atom probe tomography (APT) performed on a Cameca Scientific Instruments Local Electrode Atom Probe (LEAP®) 3000XSi. The atom probe tips were prepared by a FIB lift out technique [29] and were sharpened into the needle-like shape, with a 5 kV clean-up step to reduce Ga⁺ implantation into the tip surface. The atom probe tips

were analyzed at a base temperature of 40 K, 0.2 nJ laser pulse energy (wavelength 532 nm) and repetition rate of 200 kHz in laser mode. The reconstructions of the data was performed on IVAS 3.6.8 software. The mode of reconstruction was based on the ‘Tip Profile’ mode, as this approach takes into account the shank evolution and the different evaporation fields in multilayered samples [30].

5.4 Experimental Results

As the Ti was reduced in thickness in the Ti/V stack, a change in the XRD peak pattern was noted, **Fig. 5.1**. At larger layer thicknesses, two independent peaks can be identified for the hcp Ti and bcc V phases. For sufficiently thin layers, satellite reflection that originate from the superlattice structure of the multilayer can be observed around each of the fundamental phase peaks, denoted by the arrow insets in the figure. These fundamental phase peaks were indexed as hcp Ti (0002) (38.4° , ICDD 00-04401294) and bcc V (110) (42.2° , ICDD 00-02201058). For the 2 nm/2 nm and 1 nm/1 nm multilayer, only one main peak was diffracted. This could suggest a phase transformation; however identifying the phase transition is ambiguous by simply examining a single reflection that does not match either of the previous ‘bulk’ peaks.

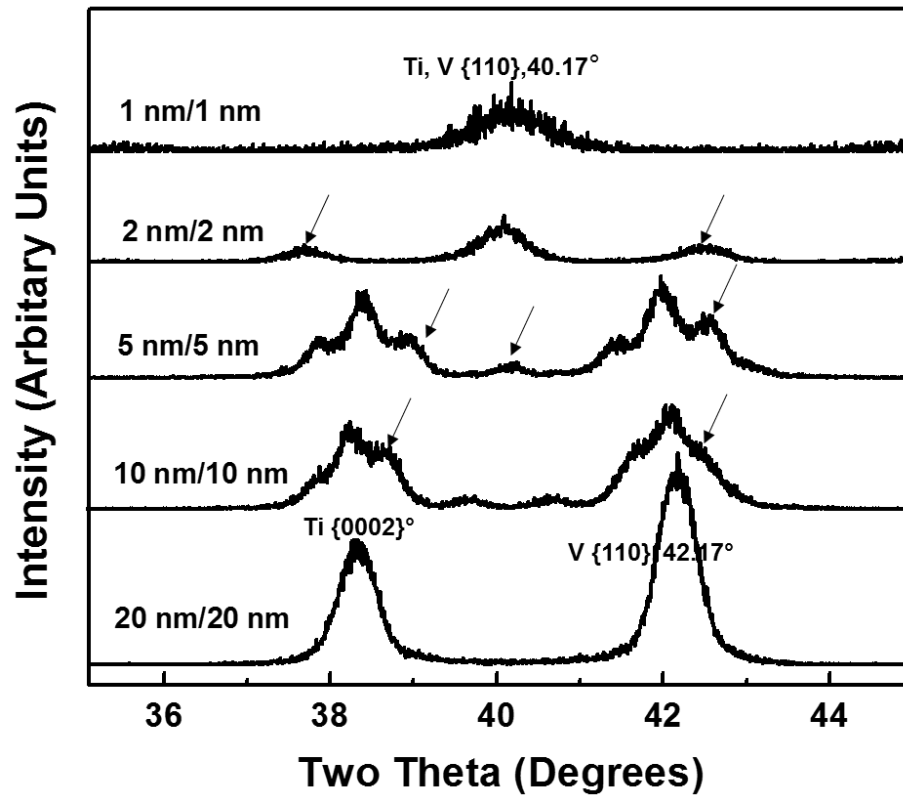


Fig. 5.1 XRD scans of Ti/V multilayers. The 20 nm/20 nm, 10 nm/10 nm, 5 nm/5 nm multilayers exhibit strong texture of Ti {0002} and V {110}. The 2 nm/2 nm and 1 nm/1 nm multilayer showed a similar pattern while the single diffracted peak is ambiguous to determine the phase transformations.

Fig. 5.2(a)-(c) show SAED patterns taken from 10 nm/10 nm, 2 nm/2 nm and 1 nm/1 nm multilayers respectively. In this orientation, multiple reflections can be seen and provide a more definitive phase identification. As seen in these patterns, the 10 nm/10 nm Ti/V film has distinctive hcp Ti rings, $\{10\bar{1}0\}$ and $\{11\bar{2}0\}$, indicating the ‘bulk’ phase of this multilayer and is in agreement with the fiber texture identification of this phase in the prior XRD results. The 2 nm/2 nm Ti/V multilayer, as shown in **Fig. 5.2(e)**, also has a $\{10\bar{1}0\}$ ring (though its intensity appears smeared or hazy) and the $\{11\bar{2}0\}$ ring is not evident. Upon reducing the bilayer to 1 nm/1 nm, only a series of reflections that can be consistently indexed to a single bcc phase is noted. Hence, the electron diffraction confirms the hcp-to-bcc transition for Ti at the thinnest spacing, with an equivalent lattice spacing for both bcc phases. Since the XRD fiber texture has changed in a similar manner between the 1 nm/1 nm and 2 nm/2 nm multilayers, it is possible that some portion of the Ti layers for the 2 nm/2 nm multilayer may contain isolated regions of bcc Ti along with the clearly identified hcp Ti phase. This conclusion is drawn from the thinnest layer’s electron diffraction, where only equivalent bcc rings were noted, but each of these films showed the same XRD fiber orientation. The in-plane grain size varied from approximately 20 to 50 nm in each of the films, **Fig. 5.2(d)-(f)**.

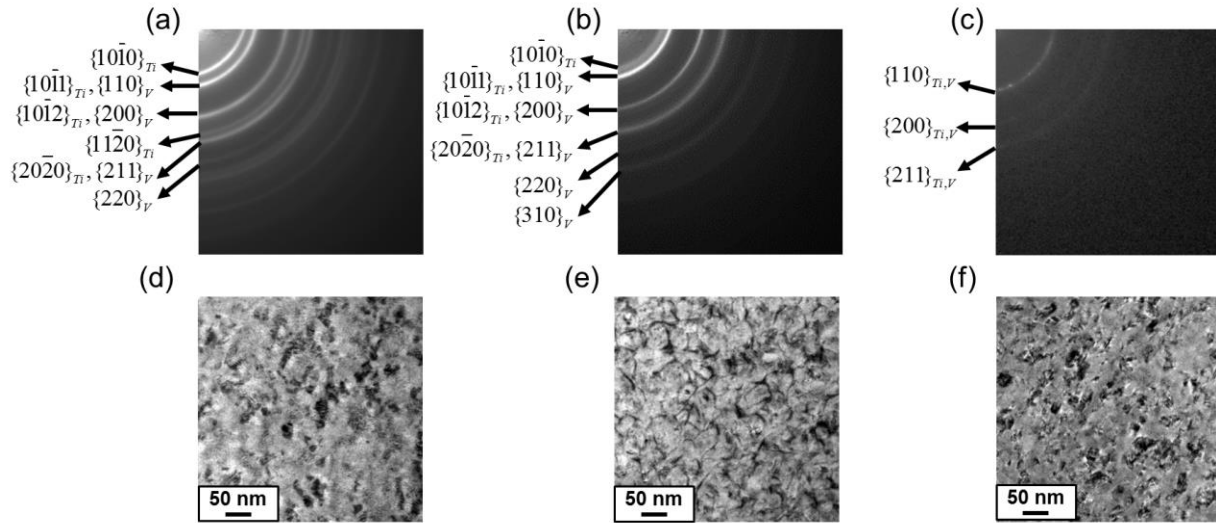


Fig. 5.2 (a) Electron diffraction pattern of 10 nm/10 nm multilayer. The distinctive hcp Ti rings, $\{10\bar{1}0\}$ and $\{11\bar{2}0\}$ confirmed this multilayer has a structure of hcp/bcc. (b) Electron diffraction pattern of 2 nm/2 nm multilayer, a hazy $\{10\bar{1}0\}$ ring was shown while the $\{11\bar{2}0\}$ ring was not evident. (c) Electron diffraction pattern of the 1 nm/1 nm multilayers. The disappearance of all the hcp ring and the rings present can only be indexed as bcc/bcc phases. (d)-(f) Representative plan-view TEM micrographs of 10 nm/10 nm, 2 nm/2 nm, 1 nm/1 nm Ti/V multilayers.

It is well known that Ti-V alloy [31] exhibits a Burgers orientation relationship [32], i.e. $\langle 11\bar{2}0 \rangle_{\alpha} // \langle 111 \rangle_{\beta}$; $\{0001\}_{\alpha} // \{011\}_{\beta}$. With the growth directions verified by XRD above, i.e. the closest packed planes parallel with each other in the growth direction, the in-plane directions were determined by diffraction taken in the cross-section view. In the 10 nm/10 nm multilayer, we can see fairly abrupt interfaces, **Fig. 5.3(a)**. Using the lattice fringe images from each layer, **Fig. 5.4(b)**, a FFT for each layer was obtained, **Fig. 5.3(c)-(e)**. These patterns reveal the associated planes and directions. Ratios of the principle spot spacings as well as the angles between the principle planes normal were calculated and consistently indexed to either α -hcp Ti $\langle 2\bar{1}\bar{1}0 \rangle$ zone axis or the bcc V $\langle \bar{1}11 \rangle$. Using the FFT from the distinct layers, overlapped spots in the collective pattern were distinctly identified to each phase. The two phases' pattern symmetry with respect to each other confirmed the Burgers orientation relationship, shown in **Fig. 5.3(f)**.

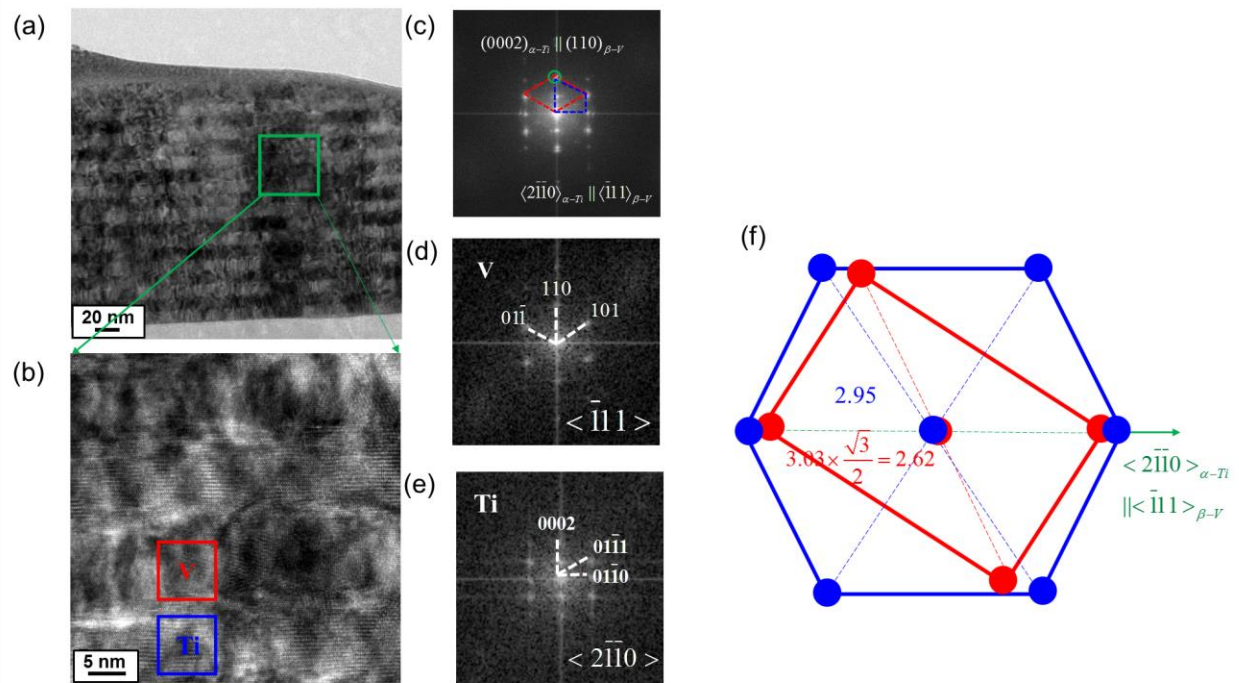


Fig. 5.3 (a) TEM BF image of cross-sectional 10 nm/10 nm Ti/V multilayer. Clear abrupt interfaces can be seen. (b) Magnified image from the ROI taken from **Fig. 5.3(a)**. A Ti and V layer were selected, shown in the two boxes. (c) Fast Fourier Transformation of **Fig. 5.3(b)**. Two sets of patterns were indexed and the zone axis were defined. (d) FFT taken from the V layer. (e) FFT taken from the Ti layer. (f) Burgers orientation relationship in Ti/V.

The *in situ* stress evolution for the Ti/V multilayers are shown in **Fig. 5.4(a)**, with the stress-thickness product plotted as a function of film thickness. For films with a negative slope, this is indicative of compressive stress whereas a positive slope indicates tensile growth. The ‘sinusoidal’ variation of slopes within one curve represent the growth of one layer on the other. There are three observations to be made from the stress behavior. First, all the films exhibit a large magnitude of an overall compressive stress condition in the post-coalescence regime [20-23]. Second, as the bilayer thickness decreases, the overall stress has a trend of becoming more compressive; however, the 1 nm/1 nm film exhibits an exception to this behavior with its overall compressive stress reduced as compared to the previously thicker bilayers. Interestingly, this 1 nm/1 nm multilayer also initially grows with a tensile stress until the overall film is ~20 nm after which the film is compressive. And third, Ti has an overall compressive behavior during its growth (negative slope) in the ‘sinusoidal’ modulation while V exhibits an opposite growth stress behavior (positive slope).

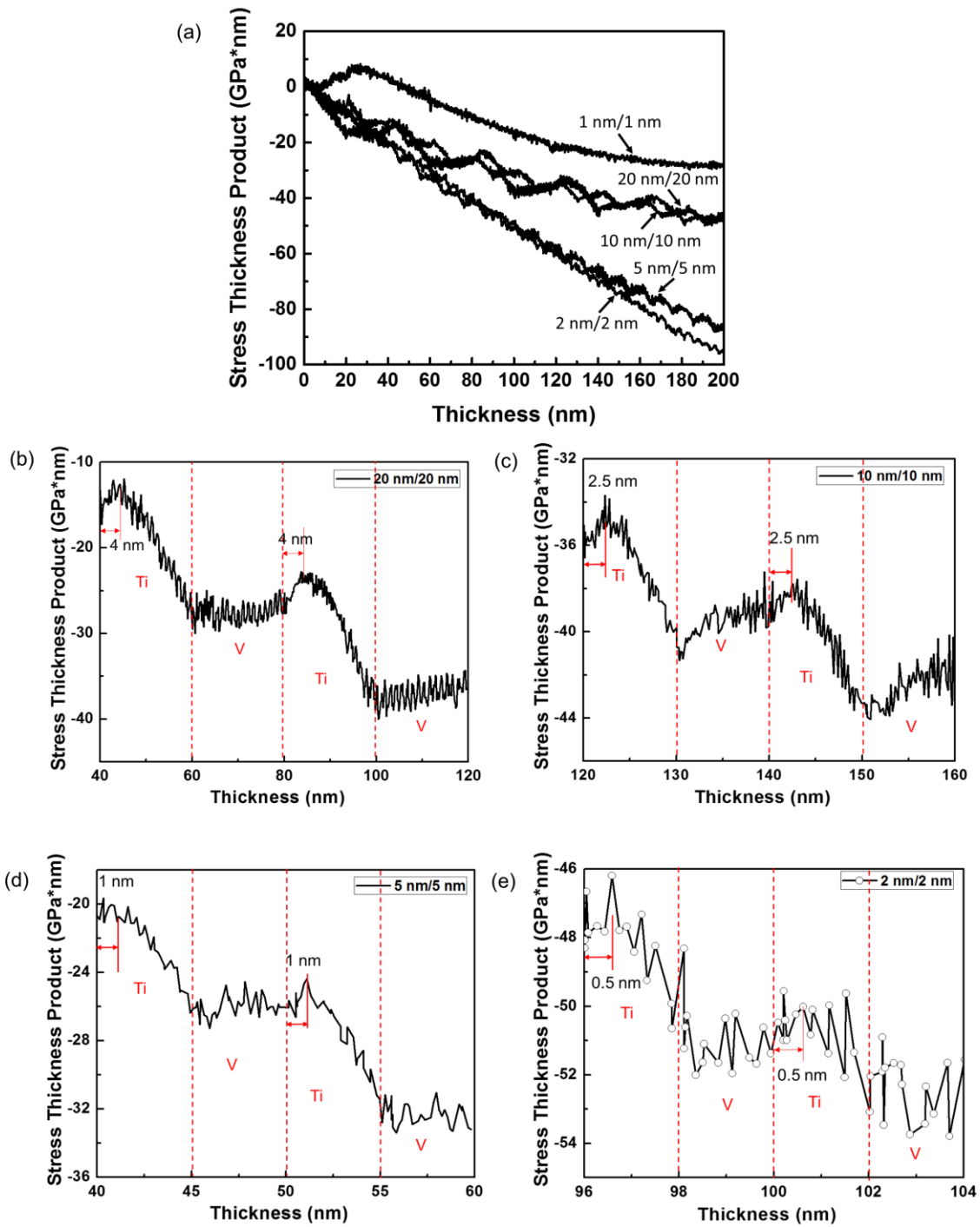


Fig. 5.4 (a) Stress evolution for Ti/V multilayers with various bilayer thicknesses. (b)-(e) Magnified growth stresses for 20 nm/20 nm, 10 nm/10 nm, 5 nm/5 nm and 2 nm/2 nm multilayers, respectively.

Magnified images of specific growth regions between Ti and V multilayers are plotted in **Fig. 5.4(b)**, **5.4(c)**, **5.4(d)** and **5.4(e)** for the 20 nm/20 nm, 10 nm/10 nm, 5 nm/5 nm and 2 nm/2 nm multilayers, respectively. For the 20 nm/20 nm thin film (**Fig. 5.4(b)**), the Ti first grows tensile up to ~ 4 nm with a slope of ~ 0.6 GPa and then reverts to a compressive growth stress with a slope of ~ -1.0 GPa for larger thicknesses. The V film exhibits a slightly positive slope (~ 0.1 GPa) for its growth throughout its 20 nm thickness. For the 10 nm/10 nm thin film (**Fig. 5.4(c)**), the growth stress for the first 2.5 nm of Ti has a tensile slope (~ 0.5 GPa) whereas a compressive slope (~ -0.8 GPa) is then noted to occur for a larger thickness. The V film in this multilayer retains the positive growth stress slope (~ 0.2 GPa). As the layer thicknesses decrease to 5 nm/5 nm (**Fig. 5.4(d)**), Ti's positive growth slope (~ 0.8 GPa) only occurs over the first ~ 1 nm and then exhibits the compressive growth stress with a slope of ~ -1.5 GPa. V retains a slightly positive growth stress of ~ 0.1 GPa. The data collection for the initial Ti growth in the 2 nm/2 nm multilayer was too noisy to definitively state if the tensile growth was evident; however the compressive growth stress is apparent revealed by the negative slope of ~ -1.7 GPa, **Fig. 5.4(e)**. The V again retains a slightly tensile or positive growth slope of ~ 0.1 GPa. The 1 nm/1 nm did not reveal any discernable changes in slope between the layers as noted in **Fig. 5.4(b)**. The dependency for the different tensile slope conditions for Ti are discussed in the preceding section.

Finally, to reveal the extent of intermixing within the multilayers, a series of atom probe compositional profiles were taken from the 10 nm/10 nm, 5 nm/5 nm, 2 nm/2 nm, and 1 nm/1 nm films, **Fig. 5.5(a)-(d)**. The 1D profile plots out the composition along the depth direction at a fixed increment of 0.3 nm. The radius of all the regions of interest were set as 2 nm while the length varies from sample to sample depending on the size of the run. The direction is to be as perpendicular to the interfaces as possible. The growth direction of the thin film and the depth

direction are opposite. Intermixing was noted in all four multilayers. Interestingly, for the thicker bilayers with the clearly discernable bulk phases, V was found to be throughout the Ti layer where Ti was not found to be throughout the V layer, **Fig. 5.5(a)-(b)**. The extent of V intermixing in the Ti increased with decreasing bilayer spacing, **Table 5.1**. Once the bilayer was 2 nm/2 nm and 1 nm/1 nm, **Fig. 5.5(c)-(d)**, intermixing of both species in each layer was present and a sinusoidal chemical modulation is seen. Even though the 1 nm/1 nm film is bcc, it is technically not a solid solution evident by the chemical modulations in the film.

Table 5.1. Intermixing width at the interfaces and the Extent of V intermixing into the Ti layer

Layer thicknesses (nm/nm)	Intermixing width (nm)		Extent of V intermixing
	Ti on V	V on Ti	
10/10	3.3±0.1	3.9±0.3	3%
5/5	1.5±0.1	2.7±0.2	5%
2/2	1.3±0.2	1.4±0.1	15%
1/1	0.9±0.1	0.9±0.1	30%

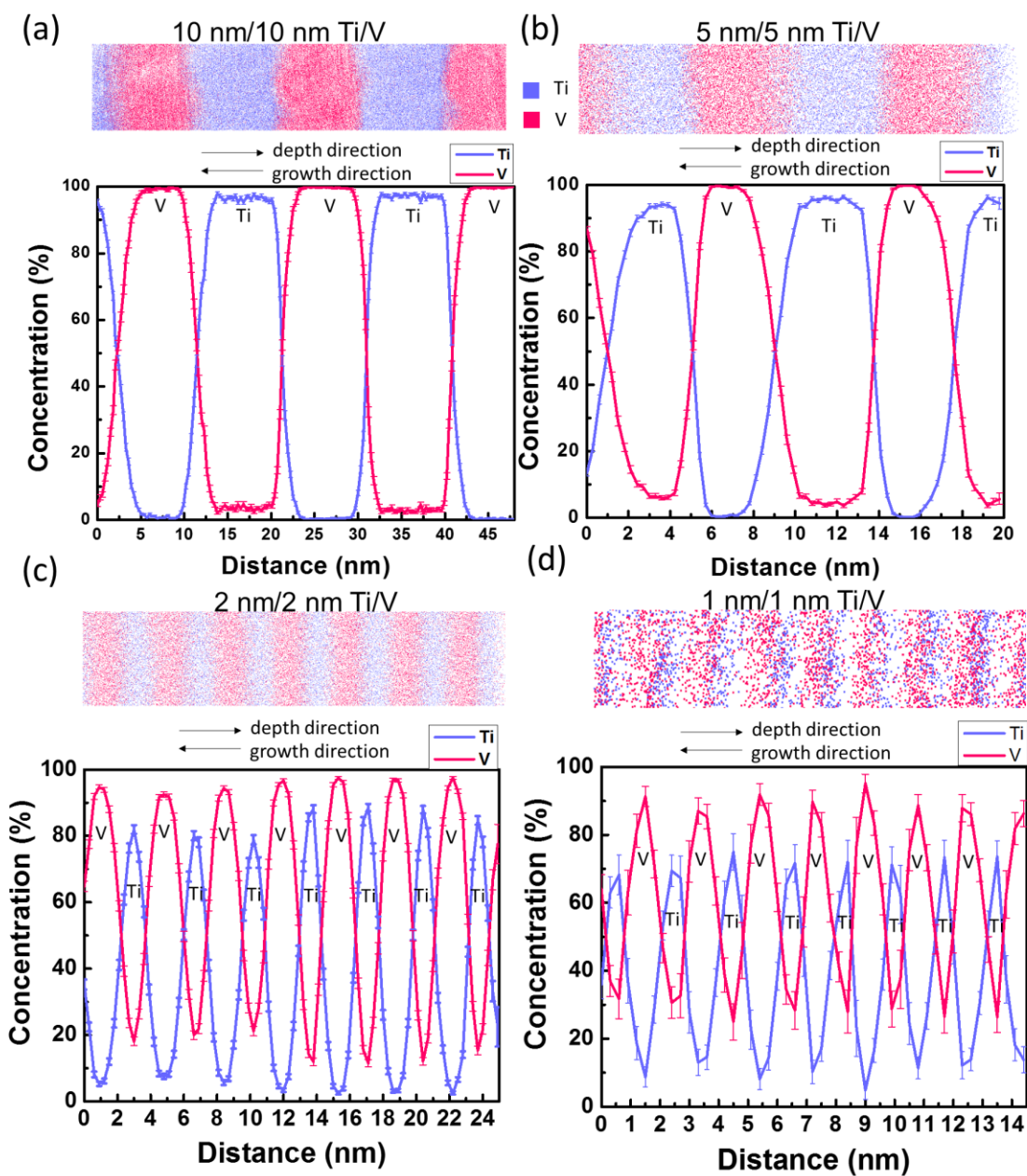


Fig. 5.5 (a)-(d) Atom probe 1D concentration profiles from 10 nm/10 nm, 5 nm/5 nm, 2 nm/2 nm, and 1 nm/1nm films. Ion maps were shown above the profile.

5.5 Discussions

Prior literature has reported that in a multilayered thin film with two dissimilar materials with a large lattice mismatch, significant stresses and strains can be manifested in the individual film layers [33,34]. This results in lattice distortions. Based on the XRD configuration shown in **Fig. 5.1**, this measurement is sensitive to lattice planes and strains perpendicular to the x-y plane or in-plane condition of the film, i.e. in the thin film's growth direction. This orientation reveals a clear fiber texture for the {0002} and {110} planes for the hcp and bcc bulk phases respectively. These surfaces are the closest packed planes with the lowest surface energy. Using these peaks, we will determine the amount of strain associated with these specific lattice planes in the z- or growth direction. In general, as the bilayer thickness was reduced from 20 nm/20 nm to 5 nm/ 5nm, the Ti {0002} peak shifted to a higher 2θ value whereas the V {110} peak shifted to a lower 2θ value. This is tabulated in **Table 5.2**, where the strain reported was calculated from

$$\varepsilon = \frac{d_1 - d_0}{d_1} \times 100\% \quad (1)$$

where d_1 is the calculated the lattice spacing from the peak position and d_0 is the 'strain-free' lattice spacing referenced from the 20 nm/20 nm multilayer. As the bilayer thickness decreases, the two individual phases appear to mechanical respond to the other with Ti out-of-plane spacing becoming compressive and V tensile. The strain values are relatively similar, with the absolute value of V being slightly higher than Ti. This difference is attributed to Ti [0002] being slightly stiffer than V [110] direction V [35,36].

For the 1 nm/1 nm multilayer, the electron diffraction confirmed the bcc phase for both Ti and V. In this case, the reported pseudomorphic bcc/bcc strain is an order of magnitude larger than the bulk phase strains. For the 2 nm/2 nm multilayer, the phase identification is somewhat

ambiguous. The electron diffraction indicated evidence of hcp Ti while the significant change in fiber texture, similar to the 1 nm/1 nm multilayer, could be suggestive of a bcc transition. We have tabulated both phases in **Table 5.2**. Either way, once bcc Ti forms, as evident in the 1 nm/1 nm multilayer, both phases significantly strain.

Table 5.2. Lattice strain calculated from XRD

Layer thicknesses (nm/nm)	Ti				V		
	Ti 2 θ peak position (°)	d_{Ti} (Å)	Ti {0002} strain (%)	Ti {110} strain (%)	V 2 θ peak position (°)	d_{V} (Å)	V {110} strain (%)
20/20	38.33	2.345	0.00	N/A	42.17	2.140	0.00
10/10	38.36	2.343	-0.10	N/A	42.11	2.143	0.14
5/5	38.45	2.338	-0.30	N/A	42.28	2.150	0.47
2/2	40.07	2.248	-4.14	-4.00	40.07	2.248	5.05
1/1	40.17	2.242	N/A	-4.39	40.17	2.242	4.77

As the film's bilayer is reduced, the overall compressive stress increased (except for the 1 nm/1 nm multilayer, which will be treated separately). This increased compressive stress is attributed to the increasingly negative compressive slope of the Ti's growth while the V growth slope was relatively constant. What is particularly interesting is that the hcp growth texture, {0002}, reveals a compressive strain, which would imply a corresponding tensile response in the growth plane. However, the majority of the film's growth is compressive. To reconcile this behavior, one must recall that the *in situ* stress measurements are a collection of both individual crystal behavior as well as the influence of adatom mobility on the growth conditions and microstructure of the film. By noting the crystal response above, we can conclude that the adatom behavior for the growing film appears to dominate the collective film's stress response.

In the early stages of Ti's growth, the Ti layer does reveal initial tensile stress, **Fig. 5.4**. This could be attributed to the intermixing of V into the Ti layer influencing the adatom mobility. From **Table 5.1**, the extent of the intermixing width between the interfaces is similar to the length scales over which the tensile slope formed. The intermixed width was defined as the length over which the compositional profile changed by more than 5 at. %. This intermixed region (**Table 5.1**) as well as the growth length of the initial tensile response (**Fig. 5.4**) similarly trend, e.g. as the bilayer thickness reduced, the intermixing width and length of tensile stress reduced. The influence of intermixing in regulating the stress states of films has been noted by others [37]. Once the V content is reduced, the Ti layer is able to exhibit post-coalescence compressive stress behavior consistent with its prior report [38].

The asymmetric intermixing width between Ti grown on V and V grown on Ti gives insights into the possible driving forces that lead to intermixing. First, the surface energy of V is slightly larger than Ti (2.88 J/m² vs. 2.57 J/m²) [39]. As V grows on the Ti surface, Ti would

preferably exchange with V to lower the surface energy. This can drive intermixing between the layers with the V on Ti being more intermixed. This type of surface exchange mechanism during growth was simulated and experimentally verified for a Cu/CoFe multilayer interface [40]. Secondly, the diffusion coefficient of V in α -Ti is two orders of magnitude higher than that of Ti in V [41,42]. Thus it is easier for V to quickly diffuse through the Ti layers. This significant diffusivity difference may also explain why V is able to completely intermix through the thicker Ti layers seen in **Fig. 5.5**. V has been reported to have a few at. % solubility within α -Ti near room temperature [43]. Finally, for the confirmed bcc Ti in the 1 nm/1 nm (and suspected 2 nm/2 nm) multilayer, V is a beta stabilizer and exhibits complete solubility between both species at high temperatures [44-46]. In this case, the amount of intermixing in both layers is acceptable and may explain why higher amounts of each species is present in each of the layers. As the extent of intermixing increased in each layer, the corresponding width of intermixing decreased as more of each species was incorporated into the other layer.

For the 1 nm/1 nm multilayer, the cumulative stress response for the film was markedly different than any of the other films grown. Using the atom probe data from **Table 5.1**, we can quantify that the intermixed width was on the same length scale as the layers themselves. Even though the film shows a chemical modulation, this chemical layering was insufficient to reveal a clear change in stress for each layer. Consequently, the compressive stress was reduced because there was no clear Ti layer which was previously shown to drive the overall compressive stress of the film by its negative slope. The mixed nature of this film also yielded a pronounced change in adatom mobility. The film exhibited a classical compressive-tensile-compressive stress response with thickness which is commonly noted in single phase films [47], though the lengths scale over which these transitions spans was larger. Though the 2 nm/2 nm multilayer exhibited the same

growth texture (and similar intermixing) as this 1 nm/1 nm film, the ability for it to retain some amount of hcp phase appears to help mitigate these growth stress changes. Thus, the change in growth stress may have to do more with phase, than intermixing and growth texture.

5.6 Conclusions

A series of Ti/V multilayered thin films with varying bilayer thickness have been sputter-deposited onto [001] Si substrates. As the bilayer thickness was reduced from 20 nm/20 nm to 2 nm/2 nm, the overall compressive stress reduced. This was attributed to Ti having a significant compressive growth stress slope as compared to the slightly tensile growth stress of V. For larger bilayer thicknesses, the initial Ti growth was tensile but reverted to a compressive stress at a thickness value dependent on the bilayer spacing. This initial Ti tensile stress is believed to be associated with the intermixing of V with Ti upon its initial growth, as the intermixing also was a function of the bilayer spacing.

The 20 nm/20 nm to 5 nm/5 nm bilayer films revealed XRD texture peaks consistent of each individual bulk phase, with each phase experiencing increasing strain with decreasing bilayer spacing. Cross-sectional electron diffraction confirmed the Burgers orientation relationship between the phases. For the 2 nm/2nm and 1 nm/1 nm bilayers, these individual XRD phase peaks were replaced by a single fiber textured peak that was in between the two peaks. However, the electron diffraction confirmed hcp Ti within the 2 nm/2 nm bilayer and only a single bcc phase for the 1 nm/1 nm. It is suspected that the 2 nm/2 nm multilayer, based on the similar XRD fiber texture as the 1 nm/1 nm multilayer, likely consisted of bcc and hcp Ti.

Upon stabilizing bcc Ti for the 1 nm/1 nm multilayer, the growth of film behavior did not show the separate elemental growth of the Ti and V and the compressive stress was significantly

reduced. Atom probe tomography confirmed a compositional modulation within this film; however, the intermixing width for this thinnest multilayer was on the same size as the individual layer thicknesses. This created a film that exhibited a classical compressive-to-tensile-to-compressive stress evolution as it grew albeit it over a larger film thickness as compared to a single element layer growth.

5.7 Acknowledgements

The authors gratefully recognize the National Science Foundation (Grant NSF-DMR-1207220) and the Central Analytical Facility in the University of Alabama for support.

5.8 References

- [1] R. Hoogeveen, M. Moske, H. Geisler, K. Samwer, *Thin Solid Films* 275 (1996) 203.
- [2] P. Boher, F. Giron, P. Houdy, P. Beauvillain, C. Chappert, P. Veillet, *J. Appl. Phys.* 70 (1991) 5507.
- [3] W. Vavra, D. Barlett, S. Elagoz, C. Uher, R. Clarke, *Physical Review B* 47 (1993) 5500.
- [4] A. Tonkikh, E. Voloshina, P. Werner, H. Blumtritt, B. Senkovskiy, G. Güntherodt, S. Parkin, Y.S. Dedkov, arXiv preprint arXiv:1510.04034 (2015).
- [5] K.M. Shahil, A.A. Balandin, *Solid State Commun.* 152 (2012) 1331.
- [6] Y. Feng, S.L. Burkett, *Journal of Vacuum Science & Technology B* 33 (2015) 022004.
- [7] R.Q. Hwang, M.C. Bartelt, *Chem. Rev.* 97 (1997) 1063.
- [8] R. Koch, *Journal of Physics: Condensed Matter* 6 (1994) 9519.
- [9] A. Miyamura, K. Kaneda, Y. Sato, Y. Shigesato, *Thin Solid Films* 516 (2008) 4603.
- [10] C. Chuang, C. Chao, R. Chang, K. Chu, *J. Mater. Process. Technol.* 201 (2008) 770.
- [11] R. Bruinsma, A. Zangwill, *Journal de physique* 47 (1986) 2055.

- [12] R. Bruinsma, A. Zangwill, *EPL (Europhysics Letters)* 4 (1987) 729.
- [13] S. Dregia, R. Banerjee, H. Fraser, *Scr. Mater.* 39 (1998) 217.
- [14] G. Thompson, R. Banerjee, S. Dregia, H. Fraser, *Acta materialia* 51 (2003) 5285.
- [15] G. Thompson, R. Banerjee, S. Dregia, M. Miller, H. Fraser, *J. Mater. Res.* 19 (2004) 1582.
- [16] J. Li, W. Liu, Q. Jiang, *Acta materialia* 53 (2005) 1067.
- [17] L. Wan, X. Yu, G.B. Thompson, *Acta Materialia* 80 (2014) 490.
- [18] C. Friesen, C. Thompson, *Phys. Rev. Lett.* 93 (2004) 056104.
- [19] R. Cammarata, T. Trimble, D. Srolovitz, *J. Mater. Res.* 15 (2000) 2468.
- [20] G. Abadias, A. Fillon, J.J. Colin, A. Michel, C. Jaouen, *Vacuum* 100 (2014) 36.
- [21] A. González-González, C. Polop, E. Vasco, *Phys. Rev. Lett.* 110 (2013) 056101.
- [22] C. Pao, S.M. Foiles, E.B. Webb III, D.J. Srolovitz, J.A. Floro, *Phys. Rev. Lett.* 99 (2007) 36102.
- [23] J.W. Shin, E. Chason, *Phys. Rev. Lett.* 103 (2009) 056102.
- [24] A.L. Shull, F. Spaepen, *J. Appl. Phys.* 80 (1996) 6243.
- [25] G.G. Stoney, *Proceedings of the Royal Society of London. Series A, Containing Papers of a Mathematical and Physical Character* (1909) 172.
- [26] J. Vermaak, C. Mays, D. Kuhlmann-Wilsdorf, *Surf. Sci.* 12 (1968) 128.
- [27] Y. Sasanuma, M. Uchida, K. Okada, K. Yamamoto, Y. Kitano, A. Ishitani, *Thin Solid Films* 203 (1991) 113.
- [28] L. Giannuzzi, F. Stevie, *Micron* 30 (1999) 197.
- [29] K. Thompson, D. Lawrence, D. Larson, J. Olson, T. Kelly, B. Gorman, *Ultramicroscopy* 107 (2007) 131.
- [30] D.J. Larson, T.J. Prosa, R.M. Ulfig, B.P. Geiser, T.F. Kelly, *Local Electrode Atom Probe Tomography*, Springer, 2014.
- [31] R. Banerjee, P. Collins, D. Bhattacharyya, S. Banerjee, H. Fraser, *Acta Materialia* 51 (2003) 3277.

- [32] D. Bhattacharyya, G.B. Viswanathan, R. Denkenberger, D. Furrer, H.L. Fraser, *Acta Materialia* 51 (2003) 4679.
- [33] J. Stevens, R. Hwang, *Phys. Rev. Lett.* 74 (1995) 2078.
- [34] V. Srikant, J. Speck, D. Clarke, *J. Appl. Phys.* 82 (1997) 4286.
- [35] D. Tromans, *Int.J.Res.Rev.Appl.Sci* 6 (2011) 462.
- [36] Y. Liu, H. Zhou, Y. Zhang, *J. Nucl. Mater.* 416 (2011) 345.
- [37] B. Clemens, W. Nix, V. Ramaswamy, *J. Appl. Phys.* 87 (2000) 2816.
- [38] J.A. Thornton, D.W. Hoffman, *Journal of Vacuum Science & Technology* 14 (1977) 164.
- [39] L. Mezey, J. Giber, *Jpn.J.Appl.Phys* 21 (1982) 1569.
- [40] X. Zhou, H. Wadley, R.A. Johnson, D. Larson, N. Tabat, A. Cerezo, A. Petford-Long, G. Smith, P. Clifton, R. Martens, *Acta materialia* 49 (2001) 4005.
- [41] Armed Services Technical Information Agency ASD-TDR-62-561 (1962).
- [42] N.L.Peterson, Wadd Technical Report WADD TR 60-793 (1960).
- [43] H. Okamoto, *Journal of phase equilibria* 14 (1993) 266.
- [44] K. Logan, (2012).
- [45] Castro, José Fernando Ribeiro de, S.F. Santos, T. Ishikawa, W.J. Botta, *Materials Research* 15 (2012) 753.
- [46] G. Thompson, R. Banerjee, H. Fraser, *Appl. Phys. Lett.* 83 (2003) 3471.
- [47] Z.Y. Hang, C.V. Thompson, *Acta Materialia* 67 (2014) 189.

CHAPTER 6

INFLUENCE OF FE UNDERLAYERS ON STRESS EVOLUTION OF TI IN TI/FE MULTILAYERS

To be submitted for publication

Influence of Fe Underlayers on Stress Evolution of Ti in Ti/Fe Multilayers

Li Wan¹, Gregory Thompson¹

¹The University of Alabama, Department of Metallurgical Engineering, Tuscaloosa, AL 35487

Keywords: phase transformations, Ti/Fe, multilayers, thin film growth stress, in situ growth measurements

6.1 Abstract

A series of 40 to 2 nm bilayer spacing Ti/Fe multilayers were sputter-deposited. As the length scale of individual Ti layers equaled to 2 nm, Ti phase transforms from a hcp-to-bcc crystal structures for equal layer thicknesses in Ti/Fe multilayers. Further equal reductions in bilayer spacing to less than 1 nm resulted in an additional transformation from a crystalline to amorphous structure. Atom probe tomography reveals significant intermixing between layers which contributes to the observed phase transformations. Real-time, intrinsic growth stress measurements were also performed to relate the adatom mobility to these phase transformations. For the hcp Ti/

bcc Fe multilayers of equivalent volume fractions, the multilayers undergo an overall tensile stress state to a compressive stress state with decreasing bilayer thickness for the multilayers. When the above phase transformations occurred, a modest reduction in the overall compressive stress of the multilayer was noted. Depending on the Fe thickness, the Ti growth was observed to be a tensile to compressive growth change to a purely compressive growth for thinner bilayer spacings. Fe retained a tensile growth stress regardless of the bilayer spacings studied.

6.2 Introduction

Multilayered thin films with large surface area-to-volume ratios have been widely applied in magnetic devices [1,2], semiconductors [3,4], thermal coatings [5,6], and optical filters [7,8]. As these multilayers individual layers are reduced in thickness, they can experience a change in phase. For example, in Co/Cr multilayers, Boher *et al.* [9] reported a change from hexagonal close packed (hcp) to body centered cubic (bcc) Co at $\sim 15 \text{ \AA}$ but later Vavra *et al.* [10] reported a bcc Cr phase transformed to hcp as the Cr thickness decreased 6 \AA . Thompson *et al.* [11,12] reported in a Zr/Nb multilayered system where Zr can undergo a hcp to bcc phase change while Nb undergoes a bcc to hcp phase change. Thus, the criteria for the phase stability of multilayers, as a function of length scale, has resulted in considerable interest in what governs phase stability at these smaller length scales.

One approach in explaining phase stability in thin layers is associated with the strain changes induced by a phase transformation [13,14]. In this model, the film's transforming layer achieves a local energy minimum whose energy is higher than the bulk phase created by the strain of the lattice on a rigid substrate. As the volume of the film was reduced, via a thinner layer thicknesses for fixed surface area, the material becomes more susceptible to such compliance

induced strains that can drive a phase transformation. Another model specifically designed for two alternating bilayers in a multilayer is based on the competition between volumetric and interfacial energy changes between different structures [11,15,16,17]. When the layer thickness is sufficiently thin, or alternatively the volume reduced for a fixed surface area, the interfacial energy reduction for a phase change can dominate the volumetric energy penalty for such a phase transformation. From a thermodynamic prospective, the change in phase is placing the system at its equilibrium condition considering the balance of the interfacial and volumetric energies. The strain contributions associated with a phase change can then be accommodated within the volumetric free energy term, with the chemical and strain contributions individual or collectively considered. Thompson *et al.* reported considered each contribution in the hcp to bcc transition of Zr for a series of Zr/Nb multilayers [11,12]. Other hcp to bcc transformations have also been reported for Ti in Ti/Nb multilayers [16,18]. In this system the coherency strains were minimal as both β -Ti and bcc Nb have similar lattice parameters; however, a significant amount of Nb interdiffusion into the Ti layers was noted that contributed to a reduction in the volumetric energy penalty for the transformation. Consequently, this additional chemically intermixing stabilized the transformation to a larger layer thicknesses [16]. How strain and/or stress evolves in multilayers and regulates phase stability, either coherency strains at interfaces or chemical intermixing across interfaces is active in both the Ti/Nb and Zr/Nb systems. The role of stress evolution and its interrelationship to coherency strains, interface intermixing, and phase stability offers a rich area of scientific investigation.

Shull and Spaepn [19] were one of the earliest reports in the use of *in situ* wafer curvature studies capturing the growth stresses in a multilayered film. In this study, the growth behavior of Cu/Ag were investigated. Since both phases are face centered cubic (fcc), one would not expect a

change in phase. Moreover, both metals are immiscible with respect to each other which would suggest a thermodynamic impedance to intermixing. Their results revealed a variation of both tensile and compressive stress evolution for a single layer as it grew on the other. Similar responses have also been noted in single films grown on rigid substrates. These stress states have been inferred to be related to the mobility of adatoms. It is generally accepted that initial compressive stress at the first stage of growth is a result of the atomic-scale migration into embryonic islands that form to minimize surface area to volumetric energies as the atoms nucleate on the substrate [20,21,22]. The subsequent tensile stress originates from the elastic strain associated with the coalescence of these islands to minimize the grain boundary energy. Upon post coalescence of the grains, the stress may retain either a tensile or compressive state depending on the mobility of their adatoms [23,24,25,26]. Elemental films with low atomic mobility tend to retain the tensile condition with continued growth but films with atoms of higher intrinsic mobility will exhibit a return to compressive stress in the post coalescence condition [27,28,29,30].

The ability to measure, in real time, the stress response of a growing film offers opportunities to infer how phase stability may affect the evolving stress. In a recent paper by the authors [18], it was noted that Ti initially grew with a tensile stress condition up to ~ 2 nm, where upon it was compressive. Using post-mortem analysis, Ti was stabilized up to ~ 2 nm and the stress behavior was consistent with the type of tensile strains the bcc Ti would undergo to coherently match the bcc Nb subsurface. In this paper, we further studied to better understand how stress evolution is affected by both phases as well as the subsurface growth layer thickness. As noted previously in the coherence strain based models [13,14], the change in phase was predicted for films on a rigid substrate (or growth surface). In a multilayer film, where the prior film deposited before the next layer is grown can be thin, its influence on the growth stress for the subsequent

layer has not been extensively addressed. Unlike the prior Ti/Nb multilayer investigations [18], Ti is the only species that known to have a bulk polymorph. In this investigation, we compare the growth stresses for Ti/Fe multilayers. Both species have known high temperature polymorphs – α hcp and β bcc Ti compared to α bcc to γ face centered cubic (fcc) for Fe. This provides an interesting case study in determining which of these elemental films will transform, if at all, with reduction in layer thickness for equal layer thickness as well as how different layer thicknesses may change the growth stress of the thicker film.

6.3 Experimental Details

The Ti/Fe multilayered thin films were sputter-deposited at equivalent individual layer thickness with bilayer thicknesses varying from 2 to 40 nm at ambient temperature (~ 25 °C) from $> 99.95\%$ pure elemental targets onto [001] Si substrates to a thickness of ~ 200 nm. Additionally two films with either 30 nm Ti/10 nm Fe and 10 nm Ti/30 nm Fe grown under the same sputtering conditions for a comparison that will be made more obvious once the experimental results are reported. The base vacuum pressure prior deposition was $< 10^{-8}$ Torr where upon ultra-high purity Argon was flowed as the working gas at 10 standard cubic centimeters per minute to a pressure of 2 mTorr.

In situ stress evolution was monitored using *k*-Space Associates (kSA[®]) Multi-beam Optic Sensor (MOS) during the deposition process. The details about this laser interferometer technique can be found elsewhere [31]. Concisely stated the technique shines a laser pattern onto a substrate surface from which the reflective rays are captured and their relative displacement measured as the substrate bends in response to the film's growth on the substrate. Using Stoney's equation [32], the amount of displacement is related to wafer curve and the stress in the film. The deposition rates

of Ti and Fe were determined by dividing the film thickness, measured from X-Ray Reflectivity (XRR) [33] and confirmed by the Transmission Electron Microscopy (TEM) cross-sectional micrographs, by the deposition time. XRR was performed on an X'pert Philips diffractometer operated with Cu K_{α} radiation ($\lambda = 1.5406 \text{ \AA}$) at 40 kV and 30 mA. The growth rates of Ti and Fe were found to be 0.029 nm/s and 0.053 nm/s, respectively.

A series of θ - 2θ scans of X-Ray Diffraction (XRD) was performed *ex situ* on a Bruker Discovery D8 General Area Diffraction Detector Systems (GADDS) with a Co K_{α} radiation source operated at 40 kV and 35 mA for phase identification. Electron diffraction patterns were also taken in the plan-view orientation (normal to the substrate) in a FEI Tecnai F20 (S)TEM to further examine the phase constitutions of each multilayer. The plan-view foils were prepared by conventional TEM sample preparation method of cutting, polishing, dimpling and ion milling. Cross-sectional TEM foils were also imaged in the (S)TEM and they were prepared by a Focused Ion Beam (FIB) lift out technique [34] followed by a 5 kV clean up step to reduce any Ga^+ implantation into the foil. Bright Field (BF) images were taken to reveal the layered morphology of the multilayers with Fast Fourier Transformation (FFT) from the higher magnification images were phase contrast imaging was evident to examine the orientation relationship between the two adjacent layers.

Finally, the multilayers were characterized by atom probe tomography (APT) performed in a Cameca Scientific Instruments Local Electrode Atom Probe (LEAP®) 3000XSi. The atom probe tips were prepared by a FIB lift out technique [35] and then sharpened into needle-like shapes with a 5 kV clean-up step to reduce any Ga^+ implantation into the tip surface. The atom probe tips were analyzed at a base temperature of 40 K, 0.3 nJ laser pulse energy (wavelength 532

nm) at a repetition rate of 200 kHz in the laser mode. The reconstruction of the data was performed on IVAS 3.6.8 software following the procedures in reference [36].

6.4 Results and Discussions

Fig. 1 shows the XRD scans of Ti/Fe multilayers at different equal bilayer thicknesses. It was observed that when the bilayer thickness is equaled or was larger than 6 nm (i.e. 20 nm/20 nm, 10 nm/10 nm, 5 nm/5 nm and 3 nm/3 nm multilayers), both the {110} Fe peak at 52.41° and {0002} Ti peak at 44.91° were present in the scans. When the bilayer thickness decreased to 4 nm (or the 2 nm/2 nm multilayer), a single phase peak with satellite peaks resulting from the periodic stacking of the layers appeared. When the two separate phase peaks are present, as the bilayer thickness is reduced, these two major material peaks shift closer to each other indicative of lattice straining at the interface between the two phases. These peaks were fitted to a Gaussian profile where upon the 2θ value was measured and converted to its d-spacing using Bragg's law. The change in d-spacing, or strain, was calculated using equation (1) where the 20 nm/20 nm multilayer was used as the reference value.

$$\varepsilon = \frac{d_1 - d_0}{d_1} \times 100\% \quad (1)$$

where ε is strains, d_1 is the calculated the lattice spacing from the peak position and d_0 is the referenced lattice spacing obtained from the 20 nm/20 nm multilayer.

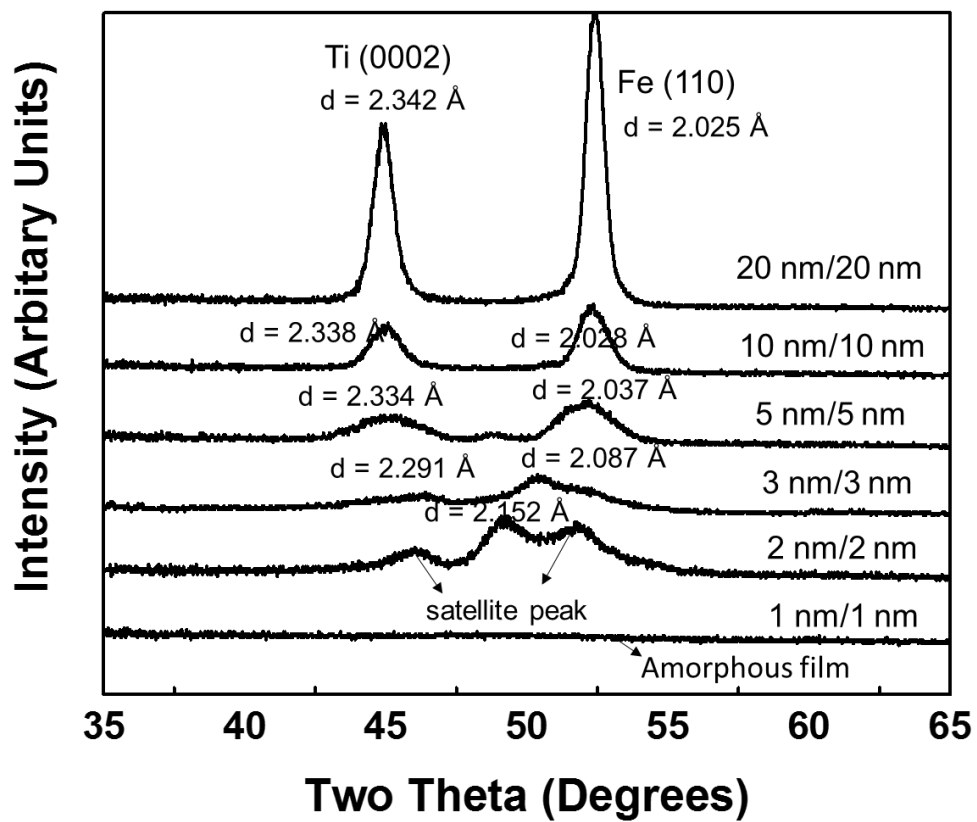


Fig. 6.1 XRD scans of Ti/Fe multilayers at various layer thicknesses

The Ti peak shift to a higher angle indicates a compressive stress response while the Fe peak shift yields an ever increasing tensile strain with decreasing bilayer spacing, **Table 6.1**. The strain values are relatively equivalent between the layers which would agree that each of these materials have similar elastic modulus values [37,38]. For the single phase peak noted for the 2 nm/2 nm multilayer, it is unclear which phase(s) this multilayer may have adopted since its peak position is not directly associated with either bulk phase. Furthermore any determination at this point would be inconclusive from a single reflection. As will be discussed below, electron diffraction provided a complementary means to achieve phase identification. Finally, the 1 nm/1 nm multilayer did not reveal any noticeable crystallographic peaks in the XRD scan. As with the 2 nm/2 nm multilayer, electron diffraction again will provided assistance in the confirmation of the phase.

Table 6.1. Lattice strain in Ti/Fe multilayers calculated from XRD

Layer thicknesses (nm/nm)	Ti				Fe		
	Ti 2 θ peak position (°)	d _{Ti} (Å)	Ti {0002} strain (%)	Ti {110} strain (%)	Fe 2 θ peak position (°)	d _{Fe} (Å)	Fe {110} strain (%)
20/20	44.91	2.342	0.00	N/A	52.41	2.025	0.00
10/10	44.99	2.338	-0.17	N/A	52.33	2.028	0.15
5/5	45.07	2.334	-0.34	N/A	52.11	2.037	0.59
3/3	46.90	2.291	-2.23	N/A	51.42	2.087	2.97
2/2	49.12	2.152	-8.83	-8.64	49.12	2.152	5.91
1/1	N/A	N/A	N/A	N/A	N/A	N/A	N/A

Fig. 2(a)-(d) are electron diffraction patterns from the 20 nm/20 nm, 3 nm/3 nm, 2 nm/2 nm, 1 nm/1 nm Ti/Fe multilayers in the in-plane orientation. In **Fig. 2(a)**, the first two rings were indexed as hcp Ti $\{10\bar{1}0\}$ and bcc Fe $\{110\}$ and the measured d-spacings from these patterns are close to their nominal lattice spacing 2.55 Å and 2.03 Å, respectively. This indicates, as did the XRD, both Ti and Fe are their bulk equilibrium phases and that neither film is experience significant strain while in contact with each other at these thicknesses. Since the Ti film is highly fiber textured along the closed packed (0001) planes, the $\{0002\}$ reflection is not evident since the electron beam is parallel to this direction. In contrast, the multiple cubic variants for $\{110\}$ could satisfy the diffraction condition and are seen in **Fig. 2(a)**. **Fig. 2(b)** shows the diffraction pattern for the 3 nm/3 nm multilayer. The brightest ring is indexed as hcp $\{10\bar{1}1\}_{Ti}$ and bcc $\{110\}_{Fe}$, which is very broad. This broadening of the diffraction ring is attributed to a spread of the d-spacings that could be occurring as this Fe layer attempts to accommodate the hcp Ti interface. The measured d spacing is ~ 2.04 Å and close to that of $\{110\}$ Fe and relatively further from the β -Ti 2.33 Å for the same reflection. The distinctive hcp rings in **Fig. 2(b)** also suggest that the Ti layer has retained the bulk phase. As the thickness decreased to 2 nm/2 nm, the prior distinctive hcp reflections are not present and a single series of reflections that can be consistently indexed to a bcc phase is shown in **Fig. 2(c)**. The lattice pattern of the first ring, $a = 2.160$, would match an equivalent lattice parameter for a $\{110\}$ reflection for the single phase peak noted in the XRD scan of **Fig. 1**. Thus, combining the X-ray and electron diffraction, we have confirmed that Ti has undergone a hcp to bcc transition for this bilayer thickness.

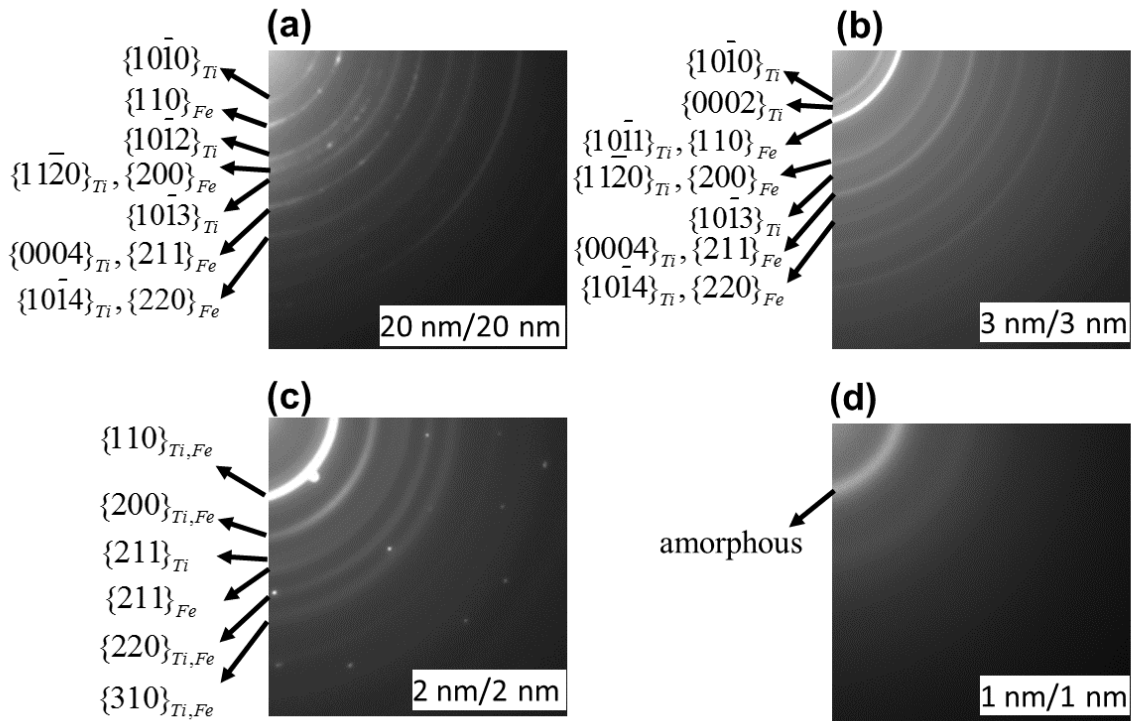


Fig .6.2 (a) Electron diffraction pattern of 20 nm/20 nm Ti/Fe multilayer. The distinctive hcp Ti rings were shown. **(b)** Electron diffraction pattern of 3 nm/3 nm Ti/Fe multilayer. Distinctive hcp Ti reflections have confirmed that this film maintained hcp/bcc phases. **(c)** Electron diffraction pattern of 2 nm/2 nm Ti/Fe multilayer. Only bcc reflections were observed. **(d)** Electron diffraction of 1 nm/1 nm Ti/Fe multilayer. This pattern showed a typical amorphous structure.

It is worthy to note that a bcc TiFe intermetallic is known to exist [39]; however, no superlattice reflections were found suggesting that this was separate bcc phases in each layer. **Fig. 3(a)** is a cross-sectional image of this multilayer along with an atom probe tomography compositional profile, **Fig. 3(b)**. From these images, it is clear a multilayered structure is present, and not a single solid solution film. Each ring in the 2 nm/2 nm diffraction pattern, **Fig. 2(c)**, is broad and can be attributed to the large strain created by the large lattice mismatch (~13 %) between the individual bcc Ti and Fe as well as the mixing of each species within each other's layer. Since Fe also has a possible option to undergo a polymorphic change, the presence of bcc Ti suggests that it is more favorable at these lower length scales. This is in agreement that the volumetric energy penalty for Ti hcp-to-bcc being modestly lower than that of Fe bcc-to-fcc, i.e.

$$\Delta G_{hcp/bcc}(\text{Ti}) = 4.57 \times 10^8 \text{ J} / \text{m}^3 \text{ versus } \Delta G_{bcc/fcc}(\text{Fe}) = 7.59 \times 10^8 \text{ J} / \text{m}^3 .$$

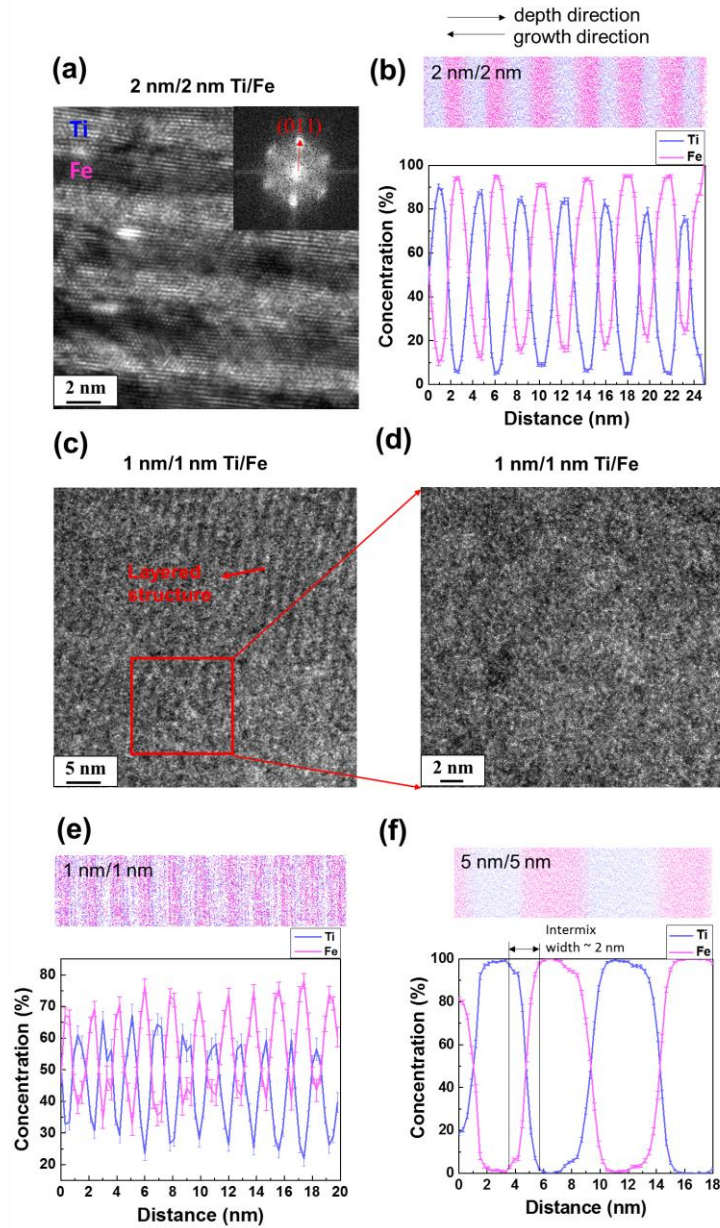


Fig. 6.3 (a) Cross-sectional TEM image of the 2 nm/2 nm Ti/Fe multilayer. The inset is the Fast Fourier Transformation for this image. It could be seen that the film has a texture of {011} which is in consistent with the out-of-plane texture in the previous XRD result. (b) Atom probe tomography compositional profile taken along the growth direction. (c) TEM cross-sectional image of the 1 nm/1 nm Ti/Fe multilayer. Some layering structure can still be observed but no crystalline structure was seen. (d) Magnified image from Fig. 6.3(c). The disordered structure has further supported the observations from the low intensity of this film by the XRD. (e) Atom probe compositional profile of the 1 nm/1 nm multilayer. Intermixing was till observed and more significant than that of the 2 nm/2 nm film. (f) Atom probe compositional profile of the 5 nm/5 nm multilayer. The intermixing width is about 2 nm. This indicated each layer grows continuously once the thickness reaches 1 nm.

For the 1 nm/1 nm thickness, the electron diffraction confirmed an amorphous ring, **Fig. 2(d)**, and would be consistent with the lack of XRD reflections. The TEM cross-sectional images, **Fig 3(c) and 3(d)**, also confirm a microstructure with a lack of any crystallinity. Interestingly, the atom probe compositional profile, **Fig. 3(e)**, does reveal the presence of a compositional modulations but whose intermixing is even larger than the prior 2 nm/2 nm profile in **Fig .3(b)**. The vitrification between Ti and Fe alloys has been reported by others [40,41,42,43] with Guo [43] reporting that amorphous phases are formed when the atomic size difference are large and the mixing enthalpy is largely negative, both of which are met for Ti-Fe [41,44,45,46]. As the sputtering process can be recognized as a rapid cooling event from the vapor to the solid [47], the intermixing between the layers at such a fine length scale, coupled with system driven to form an intermetallic equilibrium structure [39], may have simply kinetically constrained the system to become disordered as the adatoms attempted to migrate to their equilibrium lattice sites.

Fig. 4(a) is the stress-thickness product plot as a function of film thickness for all the multilayers for the various bilayer thicknesses ranging from 40 nm to 2 nm. Several observations can be made from the stress plot. First, as the bilayer thickness decreases, the overall stress moves from an overall tensile to compressive state, with a dramatic change between the 5 nm/5 nm to 3 nm/3 nm multilayers. By viewing the stress slopes changes as each layer grows on the other, we can decipher the driving force for these changes. For the thicker bilayers, the Ti layer shows an initial tensile to compressive stress evolution, **Fig. 4(b)**, with the extent of the tensile growth diminishing with reducing bilayer thickness, **Fig. 4(c)-(d)**. However, Fe retains a positive or tensile growth behavior regardless of the bilayer spacing. Hence, as the bilayer thickness is reduced, the increasing dominate compressive or negative slope of Ti's growth drives the system to an overall more compressive stress within the multilayer. Once the 3 nm/3 nm film is deposited, the Ti growth

shows no initial tensile or positive growth, **Fig. 4(e)**, creating the dramatic increase in compressive stress between it and the 5 nm/5 nm multilayer, **Fig. 4(d)**, which still retains a minor initial tensile growth component. The compressive stress slightly relaxes between the 3 nm/3 nm and the 2 nm/2 nm multilayer (**Fig. 4(f)**) which is attributed to the change in phase from hcp Ti/bcc Fe to bcc Ti/bcc Fe. Once the film forms the amorphous phase, the compressive stress slope value saturates to a value very near the bcc/bcc multilayer's stress.

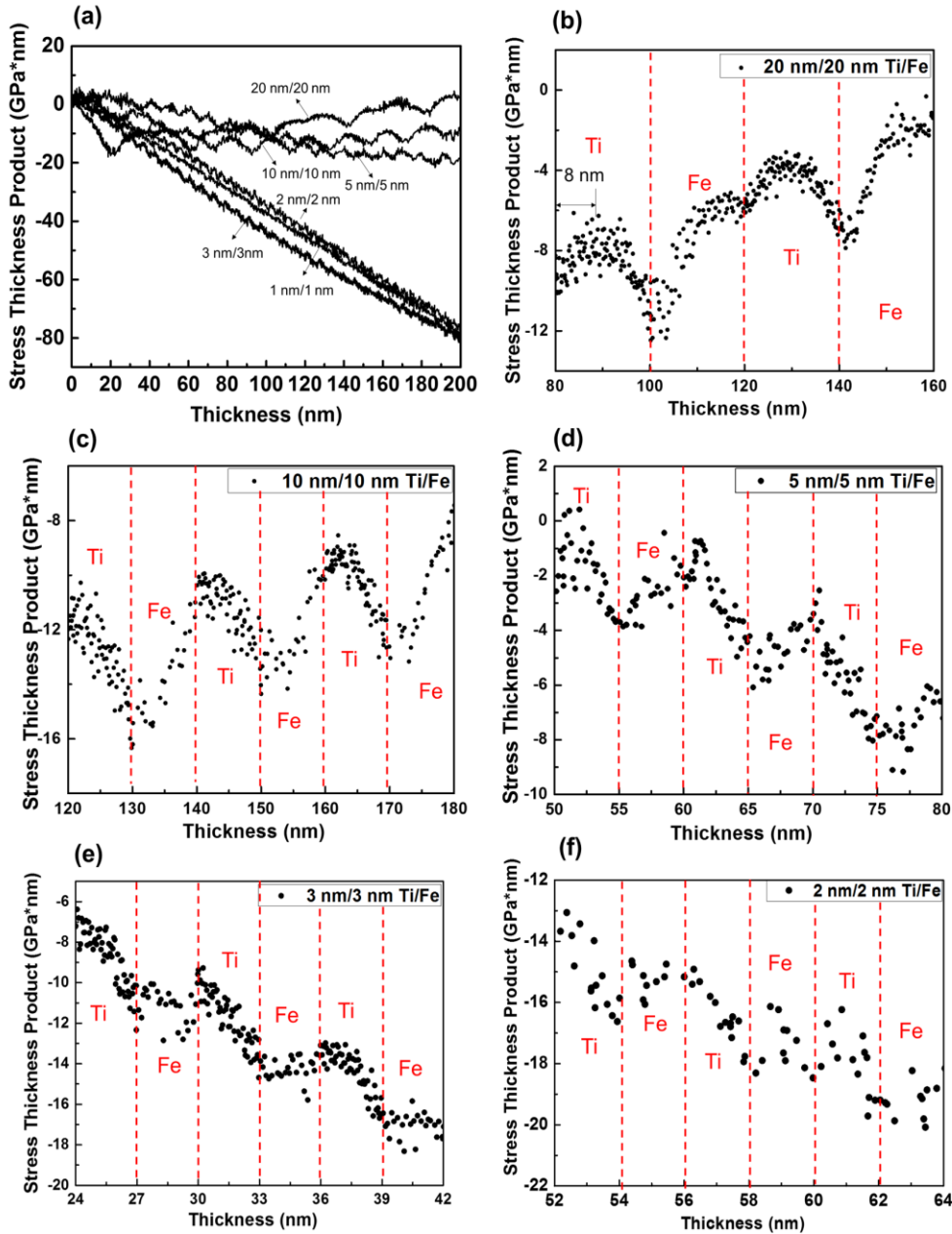


Fig .6.4(a) Stress-thickness product plot for Ti/Fe multilayer layers at various layer thicknesses. **(b)** Magnified stress plot of the 20 nm/20 nm Ti/Fe multilayer. Ti grows tensile up to 8 nm and then rolls back. Fe grows tensile through its whole thickness. **(c)** Magnified stress plot of the 10 nm/10 nm Ti/Fe multilayer. Ti's tensile growth behavior is not as obvious as that of the 20 nm/20 nm film. **(d)** Magnified stress plot of the 5 nm/5 nm Ti/Fe multilayer. Ti has a more compressive stress slope than that of the 5 nm/5 nm film and contributes to the large overall compressive stress behavior. **(e)** Magnified stress plot of the 3 nm/3 nm Ti/Fe multilayer. Ti shows no initial tensile growth behavior. **(f)** Magnified stress plot of the 2 nm/2 nm Ti/Fe multilayer. The compressive stress slope for Ti slightly relaxes.

The prior change in the tensile growth of Ti as a function of bilayer spacing provides an interesting understanding of how Ti is growing on the Fe surface and directly is affected by the layer thickness of the subsurface Fe. For the 20 nm/20 nm multilayer, Ti exhibits a tensile growth behavior up to ~ 8 nm before it rolls over to a negative slope commensurate with a compressive stress. It is clear from this work, that bcc Ti would be very unlikely stabilized to such a layer thickness. Prior work by the authors [18] noted this change over to corresponding with the phase change of the Ti layer. At least in this system, the change in slope is likely more related to the mobility of the adatoms on the growth surface which appear relatively independent of the phase (bcc or hcp) of Ti, if bcc is only stabilized up to ~ 2 nm based on the 2 nm/2 nm multilayer diffraction, **Fig. 2(c)**. From the introduction, tensile stresses are associated with either elastic strains of embryonic islands coalescence or low adatom mobility once coalescence has been achieved; in contrast compressive stresses are associated with higher mobility adatoms. Based on prior literature, Ti tends to exhibit post coalescence compressive growth, while prior literature reports for Fe being a low mobility film that exhibits tensile growth as seen in these multilayers. Thus, it appears that Fe has a much more dramatic influence on Ti's growth (evident by the growth stress variation) as compared to Ti on Fe's growth (which remained relatively consistent and tensile). Using the atom probe compositional profile from the 5 nm/5 nm multilayer, **Fig. 3(f)**, we can determine that the intermixed width for these films is ~ 1.5 to 2 nm and that once a film achieves a thickness > 1 nm, the layer itself only contains its own species.

As a comparison of how the different layer thicknesses affect the growth, two nonequivalent layer bilayer multilayers were grown, i.e. a 10 nm Ti/30 nm Fe and a 30 nm Ti/10 nm Fe. The growth stresses and XRD scans/electron diffraction patterns (which confirm both multilayers adopted the bulk phases) are given in **Fig. 5(a)-(d)**. For the 10 nm Ti/30 nm Fe film,

Fig. 5(c), Ti reveals a relatively positive slope growth with the Fe film continuing that trend up to ~ 10 to 15 nm after which the stress is relatively invariant, **Fig. 5(a)**. Upon a closer inspection of the 20 nm/ 20 nm film, **Fig. 3(b)**, there appears hints of a similar leveling out behavior of the stress near the end of its growth. Ti's lower bulk modulus (110 GPa) than that of Fe (170 GPa) [48] likely contributed to Ti being more compliant to the strains of it growing on the much thicker (rigid) Fe surface. This is manifested by its strain value noted in **Table 6.1**. According to the interpretation of Shull and Spaepen [19], as well as others [23,24,25,26], this change in slope would be associated with coalescence of the film on the multilayer growth surface. If this clear variation in slope does represent the point of complete Fe coalescence, then Fe's mobility from one of Volmer-Weber island growth [49] changes to one of near wetting across the surface for thickness $> \sim 10$ to 15 nm. For the 30 nm Ti/ 10 nm Fe multilayer, the Fe layer maintains a positive slope for all growth conditions and that the Ti exhibits a nearly instantaneous initial compressive growth and never achieves a 'leveling out effect' as observed with Fe tensile condition. Thus, even in these non-equivalent bilayers, Fe's layer thickness continues to influence Ti's growth stresses. We can conclude that once the Fe layer is sufficiently thin (≤ 10 nm), the Ti layer is driven to grow compressively.

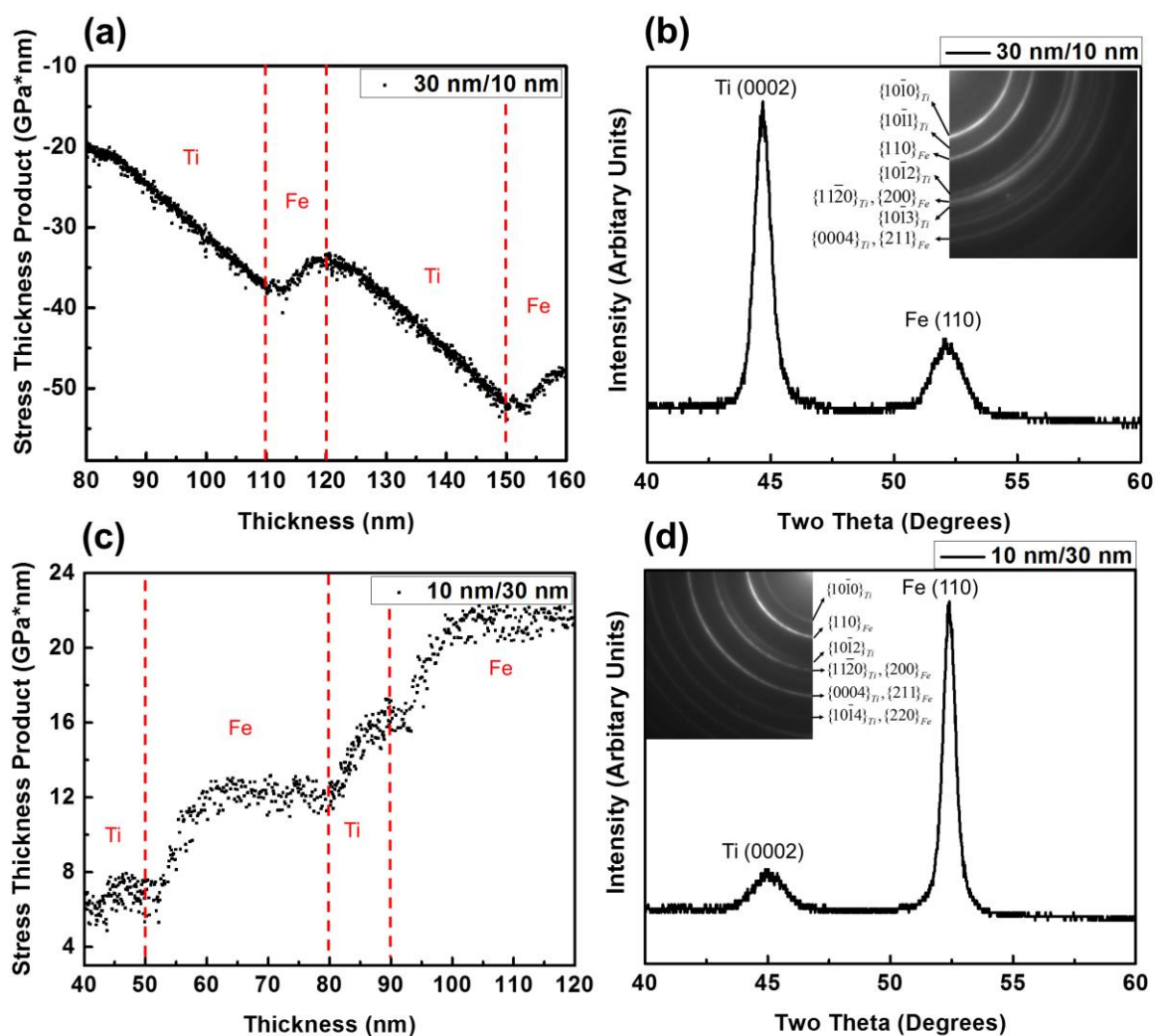


Fig. 6.5 (a) Magnified stress plot for the 30 nm Ti/10 nm Fe multilayer. No significant tensile growth behavior of Ti was observed. The large compressive stress slope of Ti indicates it has considerably good adatom mobility on the Fe surface. (b) XRD scan and electron diffraction pattern taken from the 30 nm Ti/10 nm Fe multilayer confirmed its hcp/bcc structure. (c) Magnified stress plot for the 10 nm Ti/30 nm Fe multilayer. Ti reveals a significant tensile growth which similarly observed in the 20 nm/20 nm film. (d) XRD scan and electron diffraction pattern taken from 10 nm Ti/30 nm Fe multilayer confirmed its hcp/bcc structure.

6.5 Summary

A series of Ti/Fe multilayered thin films with varying bilayer thickness have been sputter-deposited onto [001] Si substrates. As the bilayer thickness was reduced from 40 nm to 2 nm, the overall stress state changed from tensile to compressive, with the most dramatic change occurring between the 5 nm/5 nm and 3 nm/3 nm. This has been explained by Ti growth stresses on the Fe surface. For bilayers greater than 10 nm, the Ti exhibited a tensile to compressive growth evolution. However, for smaller bilayer spacings, Ti initially grows in a compressive state.

When the multilayer was 2 nm/2 nm, the Ti was stabilized as a bcc phase; however, both the bcc Ti and bcc Fe were highly strained. Further decreases in the bilayer resulted in the vitrification of the multilayer. The crystalline to amorphous phase transitions is attributed to the large atomic size difference, significant intermixing, and negative enthalpy of mixing kinetically constraining the system to form the bulk equilibrium TiFe (or TiFe₂) intermetallic. These phase changes resulted in a modest reduction of the compressive stress of the film.

6.6 Acknowledgements

This work has been supported by the National Science Foundation (Grant NSF-DMR-1207220). The authors thank the Central Analytical Facility in the University of Alabama for support.

6.7 References

- [1] Hylton TL, Coffey KR, Parker MA, Howard JK. Science 1993;261:1021.
- [2] Draaisma HG, De Jonge W, Den Broeder F. J Magn Magn Mater 1987;66:351.
- [3] Bhattacharya P, Das RR, Katiyar R. Appl.Phys.Lett. 2003;83:2010.

- [4] Kumar MMD, Devadason S. Applied Nanoscience 2013;3:453.
- [5] Cahill DG, Bullen A, Seung-Min L. High Temperatures High Pressures 2000;32:135.
- [6] Nuru Z, Arendse C, Muller T, Khamlich S, Maaza M. Solar Energy Mater.Solar Cells 2014;120:473.
- [7] Ylilammi M, Ranta-aho T. Thin Solid Films 1993;232:56.
- [8] Heavens OS. Optical properties of thin solid films. Courier Corporation, 1991.
- [9] Boher P, Giron F, Houdy P, Beauvillain P, Chappert C, Veillet P. J.Appl.Phys. 1991;70:5507.
- [10] Vavra W, Barlett D, Elagoz S, Uher C, Clarke R. Physical Review B 1993;47:5500.
- [11] Thompson G, Banerjee R, Dregia S, Fraser H. Acta materialia 2003;51:5285.
- [12] Thompson G, Banerjee R, Fraser H. Appl.Phys.Lett. 2003;83:3471.
- [13] Bruinsma R, Zangwill A. Journal de physique 1986;47:2055.
- [14] Bruinsma R, Zangwill A. EPL (Europhysics Letters) 1987;4:729.
- [15] Dregia S, Banerjee R, Fraser H. Scr.Mater. 1998;39:217.
- [16] Thompson G, Banerjee R, Dregia S, Miller M, Fraser H. J.Mater.Res. 2004;19:1582.
- [17] Li J, Liu W, Jiang Q. Acta materialia 2005;53:1067.
- [18] Wan L, Yu X, Thompson GB. Acta Materialia 2014;80:490.
- [19] Shull AL, Spaepen F. J.Appl.Phys. 1996;80:6243.
- [20] Cammarata R, Trimble T, Srolovitz D. J.Mater.Res. 2000;15:2468.
- [21] Spaepen F. Acta Materialia 2000;48:31.
- [22] Friesen C, Thompson C. Phys.Rev.Lett. 2002;89:126103.
- [23] Freund L, Chason E. J.Appl.Phys. 2001;89:4866.
- [24] Tello JS, Bower AF, Chason E, Sheldon BW. Phys.Rev.Lett. 2007;98:216104.
- [25] Chason E, Sheldon B, Freund L, Floro J, Hearne S. Phys.Rev.Lett. 2002;88:156103.
- [26] Floro JA, Chason E, Cammarata RC, Srolovitz DJ. MRS Bull 2002;27:19.

- [27] Abadias G, Fillon A, Colin JJ, Michel A, Jaouen C. *Vacuum* 2014;100:36.
- [28] González-González A, Polop C, Vasco E. *Phys.Rev.Lett.* 2013;110:056101.
- [29] Pao C, Foiles SM, Webb III EB, Srolovitz DJ, Floro JA. *Phys.Rev.Lett.* 2007;99:36102.
- [30] Shin JW, Chason E. *Phys.Rev.Lett.* 2009;103:056102.
- [31] Fu B, An W, Turner C, Thompson G. *Phys.Rev.Lett.* 2010;105:096101.
- [32] Stoney GG. *Proceedings of the Royal Society of London.Series A, Containing Papers of a Mathematical and Physical Character* 1909:172.
- [33] Sasanuma Y, Uchida M, Okada K, Yamamoto K, Kitano Y, Ishitani A. *Thin Solid Films* 1991;203:113.
- [34] Giannuzzi L, Stevie F. *Micron* 1999;30:197.
- [35] Thompson K, Lawrence D, Larson D, Olson J, Kelly T, Gorman B. *Ultramicroscopy* 2007;107:131.
- [36] Larson DJ, Prosa TJ, Ulfing RM, Geiser BP, & Kelly TF. *Local electrode atom probe tomography*. Springer, 2014.
- [37] Welsch G, Boyer R, & Collings E. *Materials properties handbook: titanium alloys*. ASM international, 1993.
- [38] Ledbetter H, Reed RP. *Journal of Physical and Chemical Reference Data* 1973;2:531.
- [39] Murray JL. *Bulletin of Alloy Phase Diagrams* 1981;2:320.
- [40] Liou S, Chien C. *J.Appl.Phys.* 1984;55:1820.
- [41] Turchanin M, Abdulov A, Agraval P. *Russian Metallurgy (Metally)* 2008;2008:370.
- [42] Fnidiki A, Juraszek J, Teillet J, Duc N, Danh T, Kaabouchi M et al. *J.Appl.Phys.* 1998;84:3311.
- [43] Sheng G, LIU CT. *Progress in Natural Science: Materials International* 2011;21:433.
- [44] Zaluski L, Tessier P, Ryan D, Doner C, Zaluska A, Ström-Olsen J et al. *J.Mater.Res.* 1993;8:3059.
- [45] Mizuno T, Morozumi T. *Journal of the Less Common Metals* 1982;84:237.
- [46] Senkov O, Miracle D. *Mater.Res.Bull.* 2001;36:2183.

[47] Luborsky F. Amorphous metallic alloys. Butterworth and Co (Publishers): London, UK, 1983.

[48] <http://periodictable.com/Properties/A/BulkModulus.v.html>.

[49] Hang ZY, Thompson CV. Acta Materialia 2014;67:189.

CHAPTER 7

CONCLUSIONS AND FUTURE WORK

Phase stability in metallic thin films has been studied for decades. People have developed various models to understand and predict this dimensional stability in a variety of systems. However, the criteria of phase stability are difficult to ascertain; it requires a combination of understanding of the materials physics as well as predictive modeling capability. To achieve that, a systematic study of how the structural and chemical nature of a material influences the phase stability in a selected material system is needed. The current research focuses on bi-metallic multilayers phase stability, for the reason that the large interfacial area maximizes the probability of interaction between the two species, including compositional interactions such as intermixing and lattice misfit such as strain. With the help of a laser interferometry technique, the growth stress during the thin film deposition can be measured in real time and the interface interaction can be back-inferred if the mechanism of the stress behavior is known. Also, post-growth structural and chemical characterization techniques provide insights in understanding the phase transformation and its relationship to the stress evolution. Furthermore, through molecular dynamics simulation, the kinetic path for the phase stability which is not easily seen from an experimental approach can be better understood.

In Ti/Nb multilayers, bcc Ti was stabilized to ~ 2 nm thickness in a series of sTi/Nb multilayered thin films grown at equivalent individual thicknesses. In the *in situ* growth stress evolution for hcp/bcc Ti/Nb multilayers, the tensile stress behavior for bcc Ti was manifested as a

positive stress slope. This was explained by the the slightly smaller bcc lattice constant of Ti (3.27 Å, extrapolated to room temperature) compared to that of Nb (3.30 Å). As Ti grows thicker, a roll-over of stress slope was noted. This transition has been rationalized to be the high mobility of the Ti on its underlayers. The bcc Nb growth exhibited a steeper compressive stress-thickness product slope regardless of the Ti phase state, which is indicative of Nb's high mobility on Ti surface. Using a MD deposition simulation, the collective compressive stress of the multilayer, which showed reasonable agreement with experimental data. APT revealed Ti segregation to the columnar grain boundaries in the multilayers and significant Nb intermixing into the bcc Ti layer. This partitioning was rationalized as a surface exchange process driven by interfacial thermodynamic considerations. The MD deposition simulation indicated that bcc Ti would be stabilized up to ~ 1 nm, but the coupling of the APT mixing results with modification to the simulated Ti layer revealed stabilization up to ~ 2 nm with intermixing and the second contact surface of Nb and was consistent with experimental findings. The results of this work have provided new insights into the complex stress evolution and phase stability behavior in nanoscale thin films.

In Ti/W multilayers, the interrelationship of growth stress evolution with a possible Ti phase transformation in Ti/W thin film multilayers were elucidated. Unlike the prior Ti/Nb multilayers, where the bcc lattice constant between Ti and bcc Nb are nearly equivalent yielding a coherent interface, the Ti/W system offers a much more strained interface of bcc Ti with W (3.16 Å). Under such a condition, the stress states were altered and provided new insights into Ti's stabilization. These films exhibit large compressive stress with W being more compressive, or alternatively more mobile than Ti. As the bilayer thickness was reduced to 1 nm/1 nm, where the phase transformation for hcp-to-bcc Ti was confirmed, the overall compressive stress reverses

back to being more compressive. The growth of 1 nm bcc Ti onto the W surface showed a steep compressive slope whose gradient decreased, but was still compressive, when compared to hcp Ti's growth. This discernable change in stress slope denoted the bcc to hcp Ti transition as a function of Ti layer thickness. Cross-sectional transmission electron microscopy micrographs confirmed the layered morphologies even at the thinnest layers studied, which directs to the minimal intermixing in this system. The stress states for each film, during film growth, was rationalized by the lattice matching of the phase with the growth surface. The lattice strain and the reduction of interfacial energy are two key factors to drive the bcc to hcp Ti phase transformation in the Ti/W multilayers. MD simulations of phase stability as a function of Ti layer thickness revealed good agreement with the experimentally observed transformation thickness.

In Ti/V multilayers, the hcp-to-bcc phase transformation of Ti and *in situ* stress evolution in Ti/V multilayered thin films were studied. The films' overall stress states are less compressive than the previous Ti/Nb and Ti/W system. This is due to the tensile growth nature of V on Ti. As growth behavior of a species is greatly dependent on its adatom mobility on the underlayer surface, where a tensile stress is related to the low mobility atom and a compressive stress is linked to high mobility atom, it can be seen that V, unlike Nb and W, is a non-mobile atom. For thicker multilayers, the initial growth of Ti is tensile but rolls over to a compressive state. Compared to Ti/Nb multilayers, where this tensile growth behavior was explained by the coherency strain between β -Ti and bcc Nb, the length of the tensile growth does not match with the phase transition thickness (1 nm in this case). This is due to the complexity of the collective stress evolution which can be a convoluted effect of strain and adatom mobility. The lattice mismatch only considered a single crystal strain but the film is polycrystalline. Atom probe results have shown the intermixing width of Ti and V interfaces are dependent on the length of the layer thickness and are about the

same length scale of the Ti's tensile the growth. For that reason, the mixed nature of Ti layer exhibits a pronounced change in adatom mobility.

In Ti/Fe multilayers, as the length scale of individual layers are reduced, hcp Ti to bcc Ti phase transformations were noted at a Ti layer thickness of 2 nm. For hcp/bcc multilayers of equivalent individual thickness, the multilayers undergo an overall tensile stress state to a compressive stress state change, with a decreased bilayer thickness. When equal thicknesses of each layer were < 1 nm, the layers underwent an additional transformation from a crystalline to amorphous structure. This has been rationalized by the atom size and mixing enthalpy considerations. The growth of Ti onto the Fe surface showed a tensile to compressive change due to the adatom mobility change. More importantly, the influence of the underlayer thickness on the growth stress behavior is readily apparent in this system. Fe has a tensile growth behavior on Ti, no matter what thickness it is of the Ti underlayer. However, there seems to be a more pronounced effect of Fe underlayer on Ti. This phenomena is observed but the mechanism is not clear yet.

To summarize, the phase stability and stress evolution in Ti/bcc multilayered thin films were studied. Each of the systems have shown significantly different behavior. Among all the bcc species studied, Nb has the least different lattice constant compared to that of β -Ti. Coherent interfaces were expected to form upon Ti phase transformation, accompanied by the reduction of interface energy. For Ti/Nb (or V, Fe) multilayers, they tend to form a Burgers orientation relationship while Ti/W has a Potter orientation relationship. This could somehow alter the thermodynamic energies and ultimately regulating the criteria of phase stability. The *in situ* stress measurements have provided a lot of insights to study the phase stability and have shown being successful in relating the phase transition thickness with the noted change of growth stress slope in Ti/Nb multilayers. However, one must recall that the *in situ* stress measurements are a collection

of both individual crystal behavior as well as the influence of adatom mobility on the growth conditions and microstructure of the film. With the proceeding study on Ti/V and Ti/Fe, this change of the stress slope from tensile to compressive of initial growth of Ti is more likely related to the mobility of the adatoms on the growth surface which appear relatively independent of the phase.

While this research provides experimental study of four different multilayer systems, there is still work that can be done in the future within the same selected materials. The possible directions to study are:

1. Different volume ratio of the two species

The recent work mostly focus on the multilayer at equivalent individual thickness. It would be interesting to expand this ratio range. According to the thermodynamic model, the critical transition thickness is dependent on two variants: bilayer thickness and the volume fraction. That means the transition can be either promoted to a higher thickness or suppressed to a lower thickness by simply varying the composition ratio of the two species.

2. Ex situ heating after deposition

As for the current research, all the deposition were done at ambient temperature. But how the temperature would affect the phase stability is not understood. For species that has certain amount of solubility, for example, Ti/Nb, might has more significant intermixing than the as-deposited state. The intermixing can possibly help the system to stabilize to bcc phase to a higher thickness. On the contrary, for systems whose solubility is limited and tend to form distinct

separate phases, the heat could result in a reduced activation energy, and the phase separation can be accelerated.

3. In situ heating: depositing at elevated temperatures

It is known that the deposition condition can greatly affect the film properties, including the phase constitutions. The growth temperature is another variant that can be used to tune the phase stability. For example, by knowing how the temperature will affect the intermixing, the extent of intermixing amount as well as the width could be modified. Also, the temperature effect can be manifested in the *in situ* stress measurement, from which the adatom mobility is apparently observed.

4. Epitaxial growth with different substrates

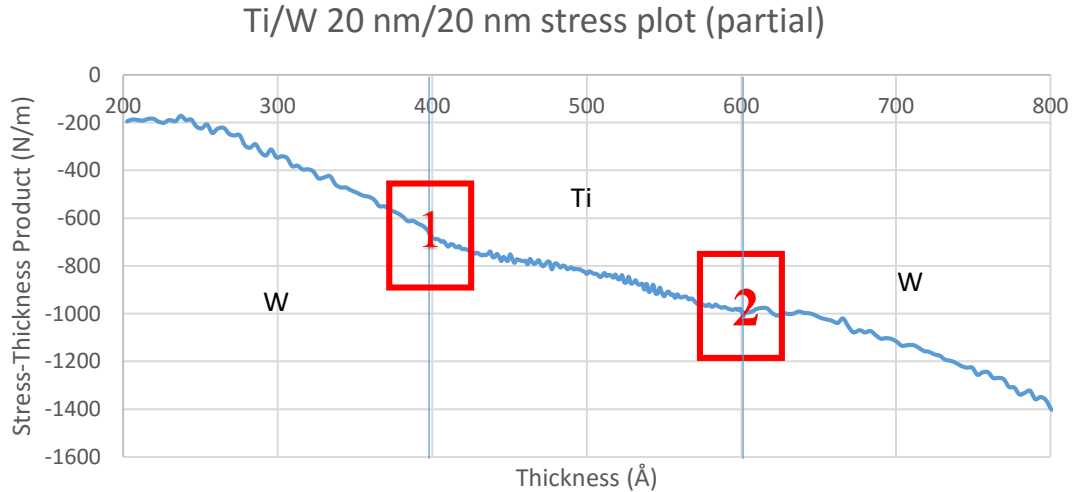
In the current study, the films are grown on [001] Si substrate with a native oxide layer to prevent any possible preferential growth/texture. And the sequence of the deposition is Ti/bcc/Ti/bcc...From the XRD pattern in all the systems studied, the films have a texture, depending on the lowest surface energy configuration. It might be interesting to deposit a buffer layer to initiate the growth of layer with a desired texture. This texture will alter the strain energy and eventually affect the stability of the multilayers.

APPENDICES

Appendix A. Procedure for Interfacial Stress Measurements

Below is an example. The data is taken from the Ti/W 20 nm/20 nm stress evolution.

1. Get the data prepared in an excel spreadsheet. The data contains two columns: thickness (\AA) and stress-thickness product (N/m).
2. Find a range you want to do measurement on. Here I take a W/Ti/W structure as an example. Plot out the data. We will focus on ROI 1 &2.



3. Obtain the phase transition thickness from XRD and electron diffraction. For Ti/W samples, the critical transition thickness is 1 nm. That means, the first 1 nm Ti grows as bcc on W surface. When it grows > 1 nm, a new hcp Ti surface is generated.

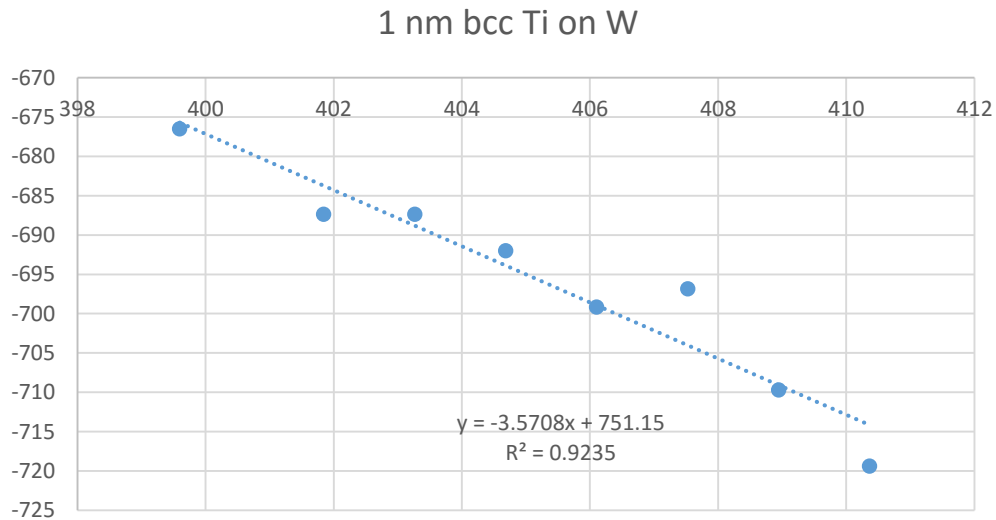
4. The equation to calculate the interfacial stress is:

$$\Delta_{\text{avg}} = [(2 \cdot \Delta_{\text{Ti on W}} (< 1 \text{ nm}) + (t_{\text{Ti}} - 1) \cdot \Delta_{\text{Ti on W}} (> 1 \text{ nm}) + (\lambda - t_{\text{Ti}}) \cdot \Delta_{\text{W on Ti}}] / \lambda \quad (2)$$

where t_{Ti} is the individual thickness of the Ti layer (nm) and λ is the bilayer thickness or $t_{\text{Ti}} + t_{\text{W}}$, $\Delta_{\text{Ti on W}}$ or when $\Delta_{\text{Ti on W}}$ in the respective thickness range.

5. To calculate $\Delta_{\text{Ti on W}} (< 1 \text{ nm})$, follow the steps below:

- 1) Write down the stress-thickness product value (y_1) at 400 Å. In this example, $y_1 = -676.518$.
- 2) Fit the data points linearly from 400 Å-410 Å, shown as below:



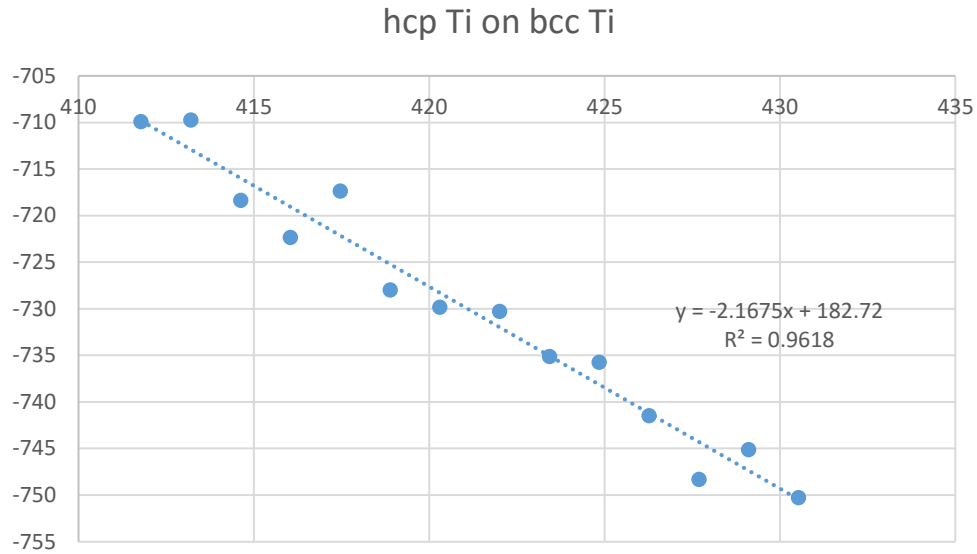
3) Plot in $x_1 = 400$ into the linear function, $y_2 = -3.5708 \cdot 400 + 751.15 = -677.17$

4) Calculate the difference between y_1 and y_2 :

$$\Delta_{\text{Ti on W}} (< 1 \text{ nm}) = \Delta y = y_2 - y_1 = -0.652$$

6. Now we calculate $\Delta_{\text{Ti on W}} (> 1 \text{ nm})$:

- 1) Write down the stress-thickness product value (y_3) at 410 Å. In this example, $y_3 = -719.403$.
- 2) Fit the data points linearly from 410 Å-430 Å, shown as below:



3) Plot in $x_3 = 410$ into the linear function, $y_4 = -2.1675 \cdot 410 + 182.72 = -705.955$

4) Calculate the difference between y_3 and y_4 :

$$\Delta_{\text{Ti on W}} (> 1 \text{ nm}) = \Delta y = y_4 - y_3 = 13.45$$

7. To calculate $\Delta_{\text{W on Ti}}$, repeat the step in step 5 & 6.

8. Put the values into the equation and get the interfacial stress value.

9. If you have more than one bilayer, do the measurement for each interface and then do a statistic analysis.

Appendix B. MD Simulation Code for Nb/Ti Multilayer and the Run Procedures

Notes: This simulation code is to create multilayer stacks by injecting atoms onto a Nb substrate.

#By Shawn Yu, Oct. 27, 2013

#----- Initialization -----

clear

units metal

dimension 3

boundary p p ff

atom_style atomic

#----- Modelling -----

lattice bcc 3.30 origin 0.0 0.0 0.0 orient x -1 1 1 orient y 1 -1 2 orient z 1 1 0 #Simulation

Box

region box block 0 89.13871 0 94.545867 0 600 units box

create_box 2 box

read_dump dump.s 0 x y z box no add yes format native

lattice bcc 3.30 origin 0.0001 0.0001 0.0001 orient x -1 1 1 orient y 1 -1 2 orient z 1 1 0

#Fixed Region

region fix block 0 89.13871 0 94.545867 0 10 units box

lattice bcc 3.30 origin 0.0001 0.0001 0.0001 orient x -1 1 1 orient y 1 -1 2 orient z 1 1 0

#Temperature Control Region

region temper block 0 89.13871 0 94.545867 10 106 units box

lattice bcc 3.30 origin 0.0001 0.0001 0.0001 orient x -1 1 1 orient y 1 -1 2 orient z 1 1 0

#Insert Volume

region insert block 0 89.13871 0 94.545867 594 596 units box side in

lattice bcc 3.30 origin 0.0001 0.0001 0.0001 orient x -1 1 1 orient y 1 -1 2 orient z 1 1 0

#Wall

region wall block 0 89.13871 0 94.545867 598 600 units box side in

group fix1 region fix #Groups

group tem2 region temper

group wall region wall

#-----Setting Layers Temperature-----

```
mass 1      92.91                                     #Mass for Nb and Ti
mass 2      47.87
velocity    fix1 set          0.0 0.0 0.0           #Fix bottom layers
fix         bottom fix1 setforce  0.0 0.0 0.0
```

```
# -----Force Field -----
```

```
pair_style eam/fs
pair_coeff * * NbTi.eam.fs Nb Ti
```

```
# -----Deposition -----
```

```
compute temp2  tem2 temp
compute_modify temp2 dynamic yes
```

```
timestep    0.001
thermo      10000
thermo_style custom step atoms temp c_temp2 etotal pe ke pxx pyy pzz
thermo_modify lost warn
dump        1 all custom 100000 dump.* id type xs ys zs
```

#-----Deposition Setting-----

variable n loop 2

label loop

#-----Nb Layer-----

variable i loop 13000

label loop1

variable r equal random(1,1000000,999)

group Nb type 1

group Ti type 2

fix source Nb nve

fix middle Ti nve

fix depo all deposit 1 1 1 \$r region insert local 2.0 2.5 1.5 vz -14.41 -14.41 units box

fix wall wall wall/reflect zlo 598 zhi EDGE units box

run 1

unfix middle

unfix source

unfix depo

unfix wall

group Ti delete

group Nb delete

group Nb type 1

group Ti type 2

fix middle Ti nvt temp 300 300 0.1

#NVT for temper

region

fix source Nb nvt temp 300 300 0.1

run 999

unfix middle

unfix source

group Ti delete

group Nb delete

next i

jump dep.in loop1

variable i delete

variable r delete

#----- Ti Layer -----

variable i loop 13000

label loop2

```
variable r equal random(1,1000000,999)
```

```
group Nb type 1
```

```
group Ti type 2
```

```
fix source Ti nve
```

```
fix middle Nb nve
```

```
fix depo all deposit 1 2 1 $r region insert local 2.0 2.5 1.5 vz -20.0605 -20.0605 units
```

```
box
```

```
fix wall wall wall/reflect zlo 598 zhi EDGE units box
```

```
run 1
```

```
unfix middle
```

```
unfix source
```

```
unfix depo
```

```
unfix wall
```

```
group Ti delete
```

```
group Nb delete
```

```
group Nb type 1
```

```
group Ti type 2
```

```
fix middle Nb nvt temp 300 300 0.1
```

```
#NVT for temper
```

```
region
```

```
fix source Ti nvt temp 300 300 0.1
```

run 999
unfix middle
unfix source
group Ti delete
group Nb delete
next i
jump dep.in loop2

variable i delete
variable r delete

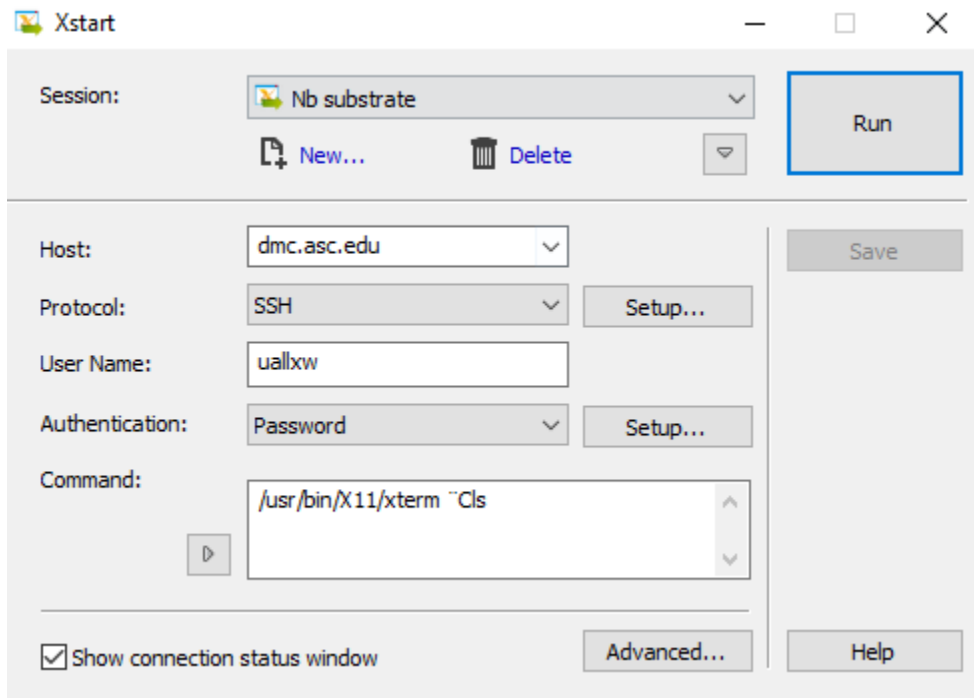
next n

jump dep.in loop

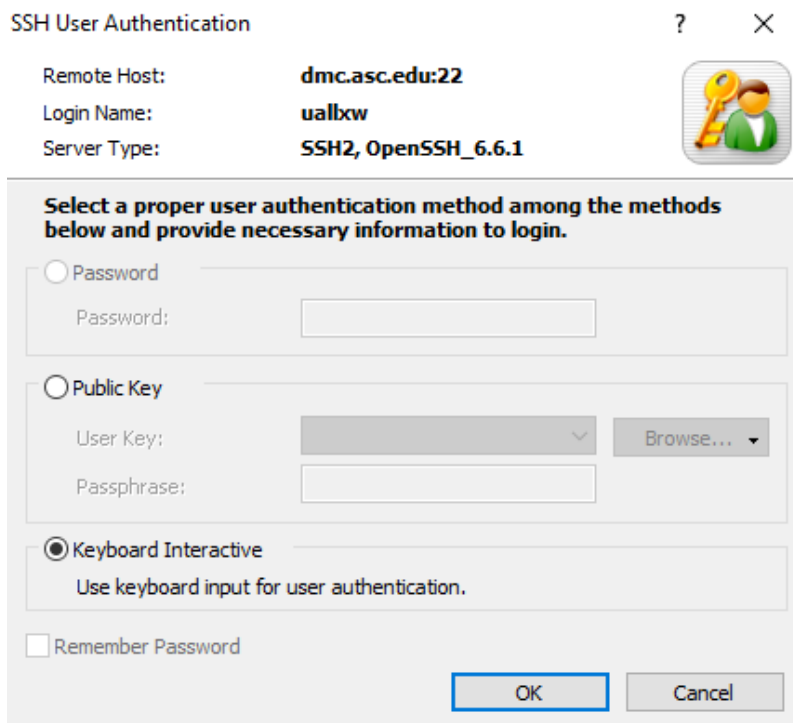
Step-by-step procedure of using this simulation code:

To prepare a substrate, here I take BCC Nb as an example.

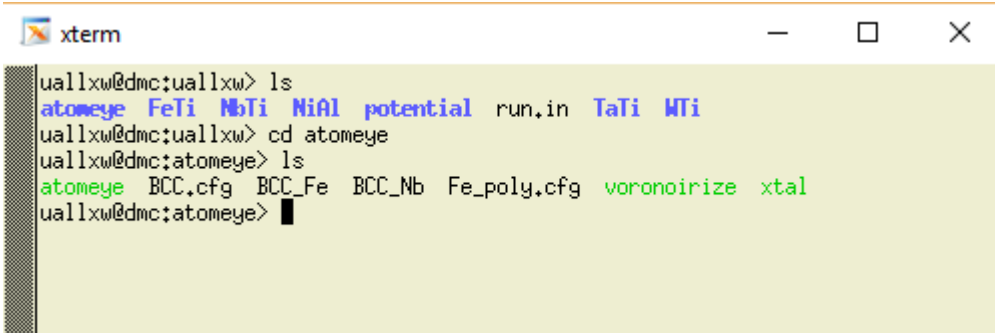
1. Open “Xmanager” and click “Run”.



2. Choose “key interactive”, click ok.



- When you see the command window below, go to the 'atomeye' folder.



```
xterm
uallxw@dmc;uallxw> ls
atomeye FeTi NbTi NiAl potential run.in TaTi MTi
uallxw@dmc;uallxw> cd atomeye
uallxw@dmc;atomeye> ls
atomeye BCC.cfg BCC_Fe BCC_Nb Fe_poly.cfg voronoirize xtal
uallxw@dmc;atomeye>
```

Note: "BCC_Nb" file can be obtained on this website link:

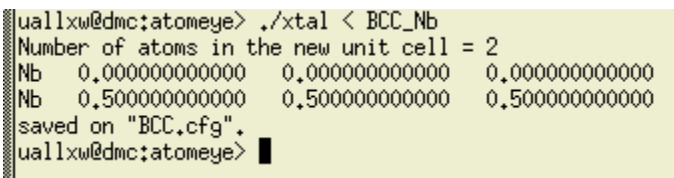
<http://li.mit.edu/A/Graphics/A/utills.html>

- Change the file format using the 'chmod' command:



```
xterm
uallxw@dmc;uallxw> ls
atomeye FeTi NbTi NiAl potential run.in TaTi MTi
uallxw@dmc;uallxw> cd atomeye
uallxw@dmc;atomeye> ls
atomeye BCC.cfg BCC_Fe BCC_Nb Fe_poly.cfg voronoirize xtal
uallxw@dmc;atomeye> chmod +x atomeye
uallxw@dmc;atomeye>
```

- When the file changes to green color, the format is successfully changed.
- Execute the following command under the 'atomeye' folder:



```
uallxw@dmc;atomeye> ./xtal < BCC_Nb
Number of atoms in the new unit cell = 2
Nb 0.000000000000 0.000000000000 0.000000000000
Nb 0.500000000000 0.500000000000 0.500000000000
saved on "BCC.cfg".
uallxw@dmc;atomeye>
```

- Execute "./atom BCC.cfg". You can see two windows pop out. The single crystal BCC Nb substrate is shown in the bottom.

```

BCC
After pairwise/own_pair saving,
likely MAX(neighbor) = ( 13 ) atoms,
atom-atom list created.

Uncompressed atom-atom list: 54000 entries, 3240004 bytes allocated,
max=10, min=4, avg=7.00 (53.8%), std.dev.=2.84 (21.8%).

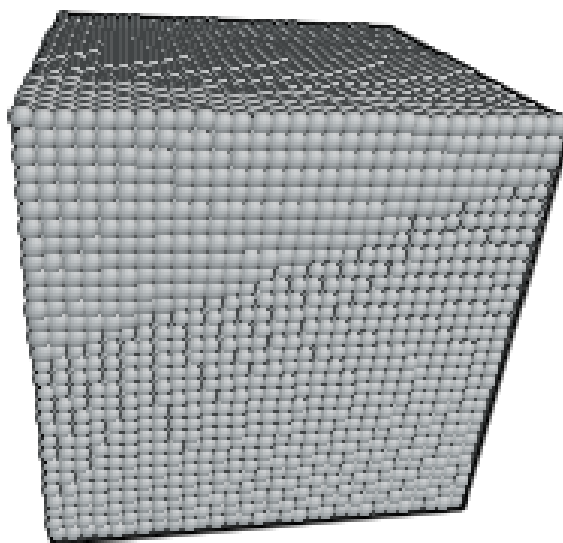
Compressed atom-atom list: 54000 entries, 1728004 bytes allocated,
max=10, min=4, avg=7.00, std.dev.=2.84 (40.6%).

All bin-related allocations freed.
----- Coordination Number Statistics -----
Coord. Count Percentage R G B Name
  14    54000    100.00%  1.000 0.894 0.882 MistyRose
-----
average = 14, most populous = 14.

      | 1 0 0 |
avg. M = | 0 1 0 |
      | 0 0 1 |

avg. microscopic shear strain = 2.74216e-17
This process has used up to 24.7 MB.

```



8. Execute “./voronoirize BCC.cfg random 3 3 3 Nb_poly.cfg”.

```

uallxw@dmc:uallxw> ls
atomeye FeTi NbTi NiAl potential run.in TaTi MTi
uallxw@dmc:uallxw> cd atomeye/
uallxw@dmc:atomeye> ls
atomeye BCC.cfg BCC_Fe BCC_Nb Fe_poly.cfg voronoirize xtal
uallxw@dmc:atomeye> ./voronoirize BCC.cfg random 3 3 3 Nb_poly.cfg
Loading "BCC.cfg"...

Guessing file format of "BCC.cfg":
should be Ju Li's CFG format.

Loading configuration from "BCC.cfg":
54000 atoms found.. reallocating memory

      | 99      0      0      | | 99      0      0      |
H = | 0       99      0      | = | 0       99      0      | A
      | 0       0      99      | | 0       0      99      |

supercell volume = 970299 = 970299 A^3
avg. atomic volume = 17.9685 = 17.9685 A^3
atomic number density = 0.0556529482149317 = 0.0556529482149317 A^-3
avg. mass density = 8.58583866598064 g/cm^3

----- Species Summary -----
Type Mass[amu] Count Abundance Wt. Pct.
Nb    92.906   54000  100.00%  100.00%
-----

Cut against all images = YES;

Grain 0 (0-26) centered at (0.829491 0.280023 0.129614) added,
  | 0.719286  0.688661  0.091503 |
R = | -0.309416  0.199642  0.929734 |.
  | 0.622004 -0.697057  0.356682 |

Grain 1 (0-26) centered at (0.890896 0.716538 0.554237) added,
  | -0.382622  0.870972  0.308233 |
R = | -0.885935 -0.251217 -0.389883 |.
  | -0.262144 -0.422253  0.867746 |

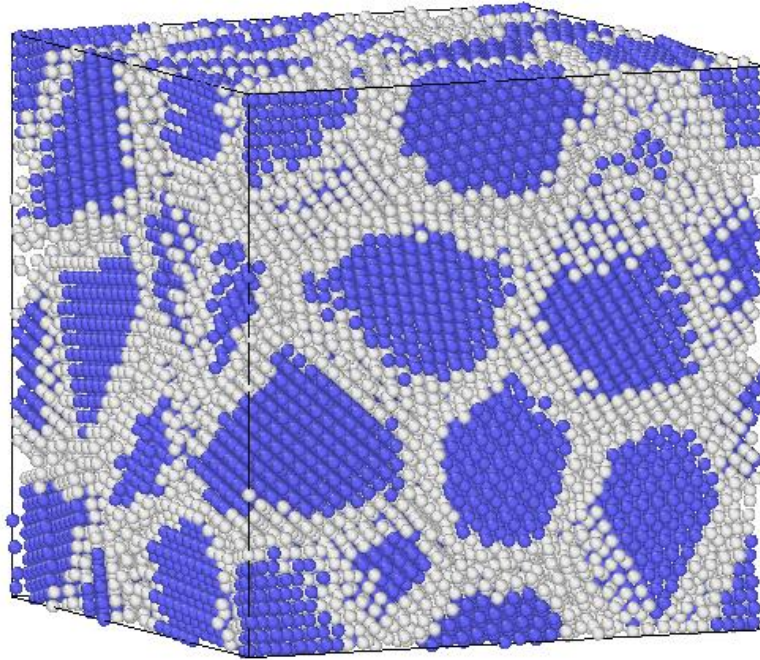
Grain 2 (0-26) centered at (0.936279 0.157338 0.371021) added,
  | -0.297503  0.095162  0.949966 |
R = | 0.584715  0.804737  0.102503 |.
  | -0.754719  0.585954 -0.295055 |

Grain 3 (0-26) centered at (0.319095 0.232942 0.917125) added,
  | 0.815054 -0.123754 -0.566014 |
R = | 0.507491 -0.318844  0.800494 |.
  | -0.279534 -0.939693 -0.197072 |

Grain 4 (0-26) centered at (0.460467 0.526093 0.819896) added.

```

9. The Nb substrate is now voronoirized. It can be visualized in OVITO software as below:



10. Prepare the following three files:

dump.o: structural file of the Nb

NbTi.eam.fs: EAM potential file for Ti-Nb binary system

dep.in: script file.